Influence of Aluminium and Titanium Alloy Particle Size Distribution on Laser-Based Powder Bed Fusion Manufacturability

Dissertation (monograph) approved

by the Doctoral Degree Committee of
Hamburg University of Technology

in pursuit of the academic degree of

Doktor-Ingenieurin (Dr.-Ing.)

written by
Ina Ludwig

from
Essen

2025

Supervisors: Univ.-Prof. Dr.-Ing. Prof. h.c. mult. Ingomar Kelbassa
Univ.-Prof. Dr.-Ing. Milan Brandt

Date of oral examination: 28.08.2025

DOI: https://doi.org/10.15480/882.16240
ORCID: https://orcid.org/0009-0008-2055-9107

Creative Commons License Agreement
The text is licensed under the Creative Commons Attribution 4.0 (CC BY 4.0) license unless otherwise noted. This means that it may be reproduced, distributed and made publicly available, even commercially, provided that the author, the source of the text and the above-mentioned license are always mentioned. The exact wording of the license can be accessed at https://creativecommons.org/licenses/by/4.0/legalcode.

Abstract

In this doctoral thesis, the influence of integrating larger particle size distributions (PSDs) up to 20-125 µm into laser powder bed fusion (LPBF) of aluminium and titanium alloys is investigated. The aim is to identify unexploited potential for significant resource and cost savings by increasing atomization yields up to 74 %. Despite the considerable advantages of LPBF in producing intricate geometries with high precision, the high cost of metal powders remains a barrier to its widespread adoption. By focusing on resource and cost efficiency while maintaining part quality, the research aims to determine whether sound-quality parts are manufacturable using larger PSDs, without compromising quality. Additionally, in this thesis, material cost-saving opportunities by integrating larger PSDs originally fractioned for electron beam-based powder bed fusion (EBM) are identified.

The generation of distinct PSDs through blending and sieving is investigated and successfully confirmed. As a suitable tool for generating homogeneous blends in an inert gas atmosphere without significant particle degradation, the V-shape blender is identified and consequently developed and tested. Thermal oxidation proved to be an effective method for particle marking to verify blending homogeneity, which is achieved after approximately 10 minutes of blending at 40 rounds per minute.

AlMg11 (commercially known as AlMgty®) and Ti-6Al-4V are examined as representatives of powder specially atomized for LPBF and as AM material with the highest metal feedstock consumption in 2020-2023, respectively. Six PSDs, ranging from 20-45 µm to 20-170 µm, are generated and evaluated for their flowability, processability, and mechanical properties. For AlMg11, wider PSDs (up to 20-125 µm) achieve consistent apparent and tapped densities and reduce Hall flow rates from 37 to 32 s/50g when compared to PSD of 20-70 µm. Relative densities above 99.5 % are reached in printed parts for all PSDs, with scanning speeds ranging from 805 to 1,405 mm/s.

For Ti-6Al-4V, blending LPBF_20-53 and EBM_45-106 powders into Ti64_20-100 enhances flowability. To reach relative part densities above 99.9 %, adapted process parameters are developed such as a 10 W higher laser power, a 0.05 mm smaller hatch distance, and 300 mm/s faster scanning speed for the larger PSDs.

Mechanical properties of printed parts are assessed for both alloys. AlMg11 shows consistent relative densities above 99.5 %, but multiple solidification defects such as pores and cracks are noted. Hardness remains within a range of 112-115 HV10 across all AlMg11 PSDs, and tensile properties decrease slightly with larger PSDs, likely due to heat retention. Ti-6Al-4V specimens meet industry reference values using adapted process parameters, with relative densities exceeding 99.9 % and comparable tensile properties across all PSDs. Hardness differences are minimal, with LPBF_20-53 showing a slightly lower hardness of 322 HV10 compared to 334-336 HV10 due to slower cooling rates.

Resource and cost analysis proves that a PSD of 20-100 µm increases atomization yield by 44 %, leading to potential material cost savings of up to 20 %, particularly for Ti-6Al-4V through the blending of LPBF and EBM powders. Further expanding the AlMg11 PSD from 20-70 µm to 20-125 µm results in a 72 % increase in the atomization yield. This research confirms that increasing the atomization yield through larger PSDs is a viable strategy for improving the cost-effectiveness and sustainability of the LPBF process without sacrificing part quality.

Table of Contents

Abbreviations

Abbreviation	Description
3D	Three Dimensional
316L	Stainless Steel 1.4404 CrNiMo-alloy
Al	Aluminium
AM	Additive Manufacturing
Ar	Argon
ASTM	American Society for Testing and Materials
BJ	Binder Jetting
BSE	Backscattered Electron
C	Carbonium, Carbon
CA	Carbon Analysis
CAD	Computer-Aided Design
Cu	Cuprum, Copper
D10/50/90	Decile with 10/50/90 %
DED	Direct Energy Deposition
DEM	Discrete Element Method
DIN	German Institute for Standardization
DOE	Design Of Experiment
EBM	Electron Beam Melting
ELI	Extra Low Interstitial
EN	European Standard
EOS	EOS GmbH (Electro Optical Systems)
Fe	Ferrum, Iron
GA	Gas Atomization
H	Hydrogen
HV	Vickers Microhardness
ICP-OES	Inductively Coupled Plasma Optical Emission Spectroscopy
IGF-TC	Inert Gas Fusion using thermal conductivity
ISO	International Organization for Standardization
LMD	Laser Metal Deposition
LPBF	Laser Powder Bed Fusion
MFFF	Metal Fused Filament Fabrication
Mg	Magnesium

Abbreviation	Description
Mn	Manganese
N	Nitrogen
O	Oxygen
OP-S/U	Oxide Polishing Solution
OVS	Oversize
PBF-LB/M	Laser-Based Powder Bed Fusion of Metals
PREP	Plasma Rotating Electrode Process
PSD	Particle Size Distribution
rpm	Rounds Per Minute
RH	Relative Humidity
SEM	Scanning Electron Microscope
Si	Silicon
SOTA	State-of-the-art
Ti	Titanium
TO	Thermal Oxidation
V	Vanadium
VED	Volumetric Energy Density
VDI	Association of German Engineers
WAAM	Wire Arc Additive Manufacturing
Zn	Zinc

Nomenclature

Symbol	Description	Unit
A	Elongation at break	%
A_P	Surface area of a powder particle	µm²
br	Build Rate	cm³/h
C	Cohesion Index	[-]
D_{crop}	Diameter cropped of GranuDrum Drum Diameter	mm
d_0	Tensile specimen diameter middle part	mm
E_L	Line Energy	J/m
HR	Hausner Ratio	[-]
l_P	Length of particle	µm
LT	Layer Thickness	mm
m	Mass of powder	g
n	Sample size	[-]
P_L	Laser power	W
PLD	Powder Layer Density	g/cm³
ppm	Parts per million, used for 0.0001 wt.-%	wt. -%
$Q(x)$	Cumulative distribution	%
$q(x)$	Frequency distribution	%/µm
$r_{1;2}$	Minimum distance to centre of area of particle	µm
r_C	Correlation coefficient	[-]
Ra	Arithmetic average of profile height deviations from the mean line	µm
R_m	Tensile strength	N/mm²
$R_{p0.2}$	Yield strength at 0.2 % elongation	N/mm²
$SPHT$	Sphericity measured by Camsizer X2	[-]
$Span$	PSD-Span (D90-D10 = Span)	[-]
$Symm$	Symmetry measured by Camsizer X2	[-]
$T_{transus}$	β-transus temperature	°C
U	Particle Circumference	µm
V	Volume of Hall-Funnel container	cm³
VED	Volumetric Energy Density	J/mm³
V_P	Volume of a powder particle	µm³
v_S	Scanning speed	mm/s

Symbol	Description	Unit
w_P	Width of particle	µm
x_{area}	Area of particle approximated to a circle of the same size and the resulting diameter is assumed	µm
$x_{c\ min}$	Minimum diameter	µm
$x_{Fe\ max}$	Feret-maximum: Maximum diameter between two parallel tangents	µm
Δy_S	Hatch distance	µm
α	α phase, hexagonal close-packed of titanium or titanium alloys	[-]
α'	Martensitic structure in titanium or titanium alloys	[-]
α''	Orthorhombic martensitic structure in titanium or titanium alloys	[-]
α_A	Avalanche angle	°
α_C	Correlation significance	%
β	β-phase, body centred cubic phase of titanium or titanium alloys	[-]
β-transus	β-phase transus temperature	°C
Ψ	Sphericity	[-]
ρ_a	Apparent density according to the funnel method	g/cm³
ρ_t	Tapped density according to the funnel method	g/cm³
σ_{CI}	Standard deviation of cohesion index	[-]

1 Introduction

The market volume of metal Additive Manufacturing (AM) has been growing from 2.08 billion US dollars in 2021 to 2.71 billion US dollars in 2023 with laser-based powder bed fusion (LPBF[1]) exhibiting the highest equipment revenue share of 40 % in 2023. With more installed LPBF machines, the latest market growth is driven by the metal feedstock consumption, that is expected to grow by up to 176 % from 3.32 billion US dollars in 2023 to 6.23 billion US dollars until 2028. [2]

The particle size distribution (PSD) for LPBF remains consistent over the last decade. It is investigated in the early 2010s, as demonstrated in studies by Spierings et al. in 2011. The PSDs are chosen based on layer thickness (*LT*) ranging between 30-60 µm [3]. Improvements of the LPBF machines such as an increase in laser powers from 200 W to 1000 W are not aligned with adaptions of the PSD. This is why the industry still relies on typical PSDs such as 10-45 µm, 20-53 µm, 20-63 µm or 20-70 µm [4]. These PSDs achieve an atomization yield ranging from 10 to 50 %. The usage of larger PSDs up to 20-125 µm offers unexploited potential for resource and cost savings by increasing the atomization yield to 30-60 % [5–8]. The quantitative contribution of this thesis to the state-of-the-art (SOTA) is presented in Figure 1-1. The target is to increase in atomization yield by 44 % and cost-effectiveness by 20 %, while maintaining consistent part quality.

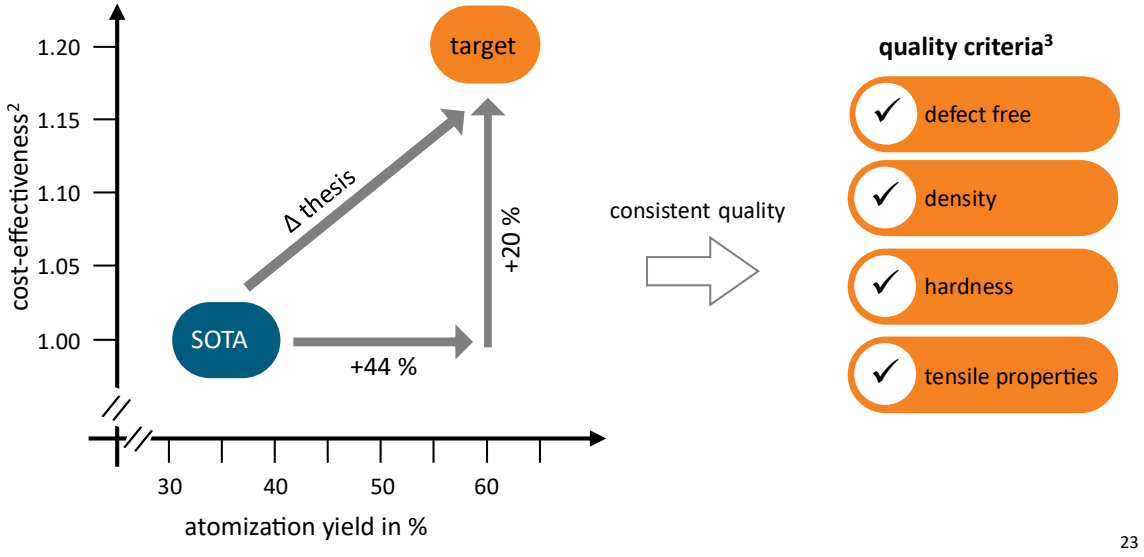

Figure 1-1: Diagram of the variables for a quantitative description of the contribution to the state-of-the-art (SOTA) (left) and list of quality criteria (right).

[1] Laser-Based Powder Bed Fusion of Metals (PBF-LB/M), as defined in ISO/ASTM 52911-1, is referred to as LPBF in this thesis [1].

[2] The calculation of cost-effectiveness is provided in Equation (1.1): $cost\ effectiveness = \frac{costs_{SOTA}}{costs_{target}}$ (1.1).

[3] Sound-quality according to VDI 3405 2.4 for Ti-6Al-4V and according to AlMgty80-datasheet for AlMg11 [9, 10].

2 Objectives and Proceeding

To investigate the influence of PSD on manufacturability, this thesis addresses the material flow from the vertical LPBF process chain, presented in Figure 2-1. The horizontal process chain demonstrates the pre-process, LPBF and post-process.

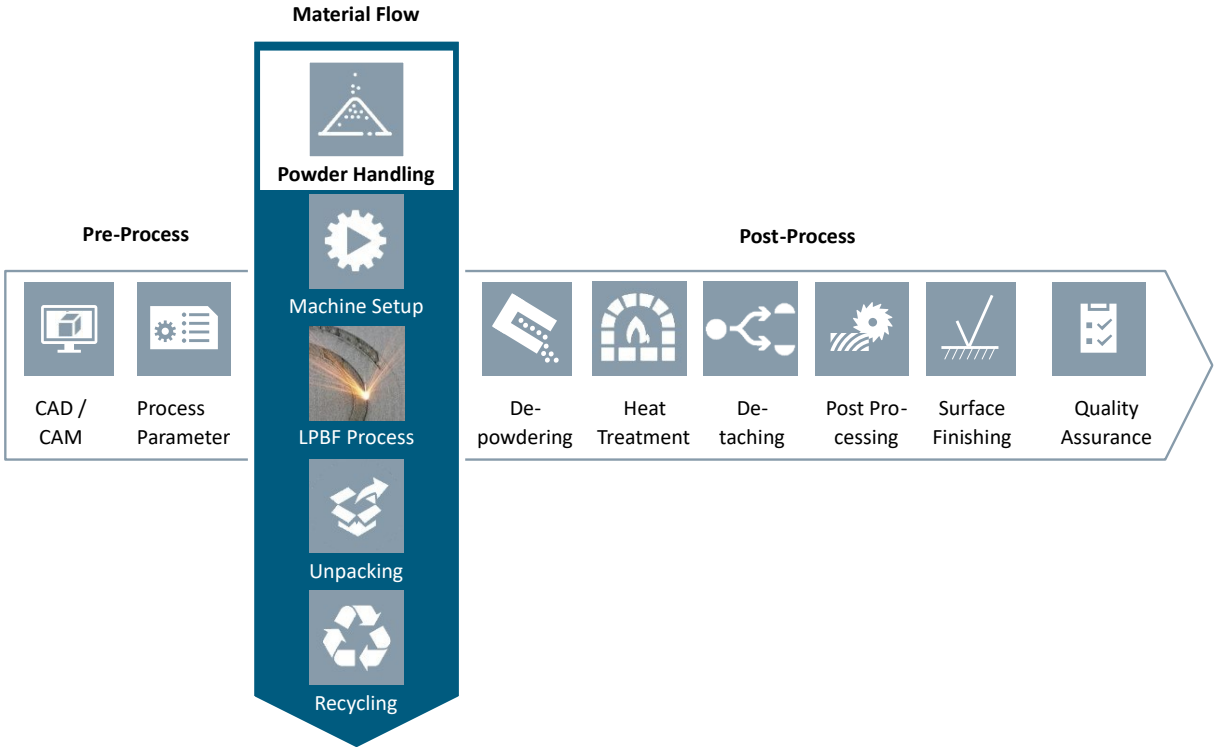

Figure 2-1: Schematic drawing of the LPBF process chain with the detailed vertical material flow.

The objective of this work is to save resources and material costs for LPBF by increasing the atomization yield by 44 % and the cost-effectiveness by 20 % without compromising quality. Therefore, the largest processable PSD from six self-generated PSDs ranging between 20-45 µm and 20-170 µm is identified by assessing the influence of PSD on flowability, process parameters and mechanical properties. Processability is given in case of generic defect free printability of the powder. The manufacturability of a PSD is defined as achieving sound quality. Sound quality implies compliance with the mechanical properties from the AlMgty80 data sheet for AlMg11 and from VDI 3405 sheet 2.4 for Ti-6Al-4V. To ensure that the self-generated PSDs feature a homogeneous distribution, and the particle shape is not affected, the blending process is validated in advance.

To achieve resource and cost savings, the identified research gaps are systematically addressed. Knowledge and findings on the processability of PSDs up to 170 µm to manufacture sound-quality parts must be acquired to answer the research question: Can sound-quality parts with increased atomization yield be manufactured using LPBF aluminium and titanium alloys? The systematics of the research approach are presented in Figure 2-2:

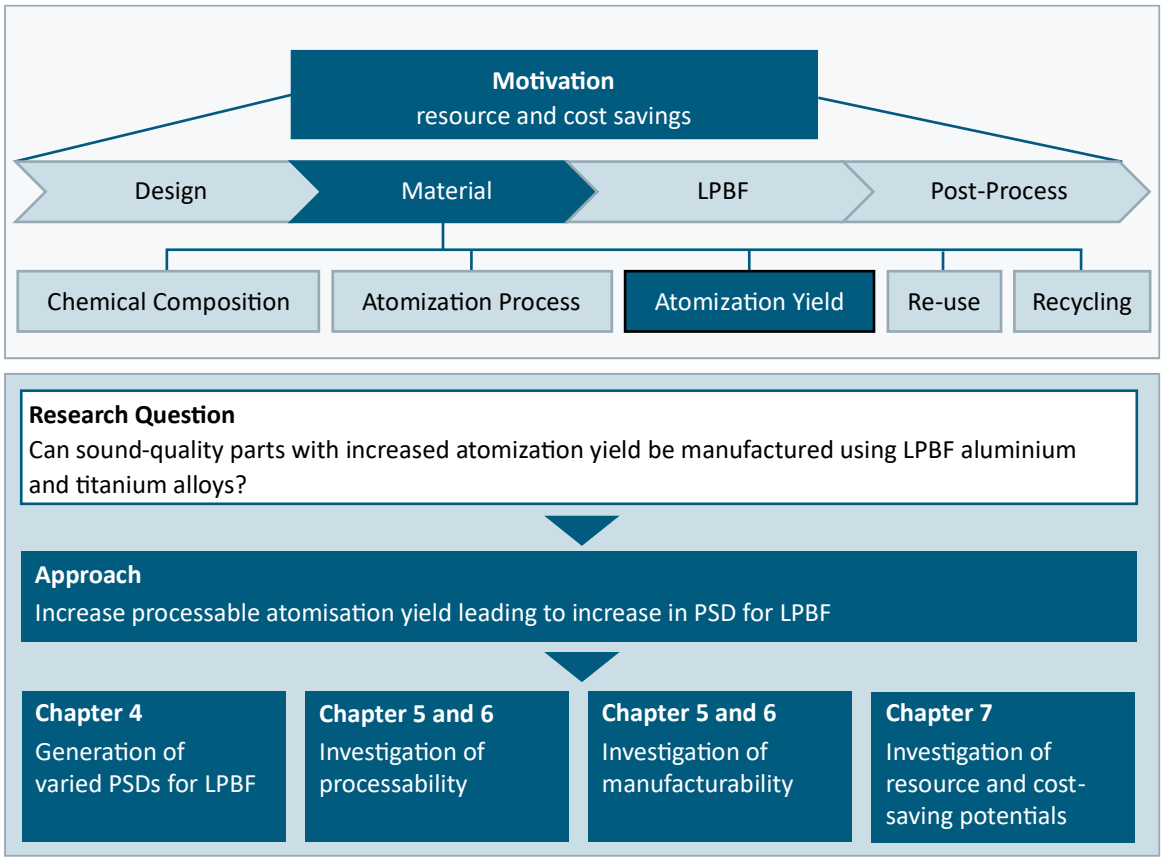

Figure 2-2: Graphical flow chart of systematics.

Chapter 5: Generation of varied PSDs for LPBF

In the first step, six PSDs are generated in the range from 20-45 µm to 20-170 µm to determine the highest processable atomization yield. A self-developed V-shape tumbling blender and sieves with aligned mesh sizes are used for this purpose. To ensure homogeneous powder blends in subsequent studies, the blending results are verified in advance. All generated PSDs are characterized by particle size, particle size distribution and particle shape. Addressing the first sub-question, "Can different PSDs be generated from commercial PSDs for LPBF?".

Chapter 6 and 7: Processability and Manufacturability of varied PSDs

The second step is to identify the influences of PSD on processability. Additionally, the influence of PSD on the flowability is determined by measuring apparent and tapped density, Hausner ratio, Hall flow-ability, avalanche angle, and cohesion index. For each PSD, process parameter adjustments are applied to establish a process window[4] for a generic, defect-free material build-up with densities exceeding 99.5 % (resp. 99.9 % for Ti-6Al-4V). If both criteria are met, processability is achieved. This contributes to answering the second sub-question: "What is the effect of the PSD on processability?".

If processability is assured, the influence on manufacturability and, consequently, the mechanical properties are investigated in the third step. Specimens are manufactured and analysed for density, microstructure, hardness and tensile properties. If the mechanical properties meet the sound-quality criteria, the PSD is manufacturable. The results are compared to those obtained using typical LPBF

[4] Process window: LPBF parameter range that leads to processability.

PSDs[5] to exclude machine and environmental influences, thereby addressing the third sub-question: “How do the different PSDs affect the mechanical properties of the manufactured parts?”.

Chapter 8: Investigation of Resource and Cost-Saving Potentials

Finally, the effect of the manufacturable PSD on the achievable resource and cost savings is examined. Representative atomization yields are used to approximate the resource savings with the achieved atomization yield. Additionally, market prices are analysed to determine cost-saving potentials for PSDs available on the market, clarifying the sub-question: “How does PSD influence resources and costs?”.

Two alloys are investigated: AlMg11 and Ti-6Al-4V. AlMg11 (traded as AlMgty®) is used as a representative of powders specially atomized for LPBF. Increasing the atomization yield for this alloy offers particularly potential for saving resources and costs by reducing the quantity of unused particles. Ti-6Al-4V serves as a representative of high-cost powders. The availability of various PSDs for Ti-6Al-4V on the market enables the purchase of more cost-efficient PSDs, such as 45-106 µm [11]. The relatively high price[6] of titanium alloy powders, along with their widespread use, offers potential cost savings for LPBF users, for example, by utilizing the electron beam melting (EBM) PSD of 45-106 µm.

All steps are carried out using both alloys, with processability and manufacturability are investigated separately. For AlMg11, the focus is on identifying the PSDs that are processable. Therefore, the specimens are manufactured with the same process parameters. For Ti-6Al-4V, the emphasis is on the comparability of manufacturability, which is why the process parameters are adapted for each PSD.

[5] LPBF PSDs: 10-45, 20-53, 20-63 or 20-70 µm [4].
[6] Pricing median Titanium is 5,734 €/kg > Aluminium > stainless steel for a single part [2].

3 State-of-the-art

In this chapter, a comprehensive review of current advancements and methodologies in LPBF, focusing on metal powders and the influence of PSD, is provided. Understanding these factors is crucial for analysing processability and manufacturability in LPBF, as well as for evaluating their impact on mechanical properties and cost-effectiveness.

3.1 Additive Manufacturing

The term additive manufacturing (AM) refers to the creation of material cohesion for the production of physical components from 3D data models through iterative and layer-by-layer construction [1]. With DIN 8580, additive manufacturing is counted among the primary forming manufacturing processes [12]. This procedure differs from conventional, subtractive processes (e.g. milling or drilling), shaping processes (e.g. casting or forging) or joining processes (e.g. welding or soldering). There are various direct metal, additive manufacturing processes, including powder bed processes with laser (LPBF) or electron beam (EBM), direct energy deposition (DED) with laser (LMD) or wire arc (WAAM) to deposit powder or wires or metal AM processes with a sintering step afterwards, like binder jetting (BJ) or metal fused filament fabrication (MFFF). An overview is presented in Figure 3-1. Each of these technologies offers advantages and limitations in terms of processable materials, build volume, processing speed, part quality (mechanical properties, dimensional accuracy and surface roughness) and the additional post-processing. [13–16]

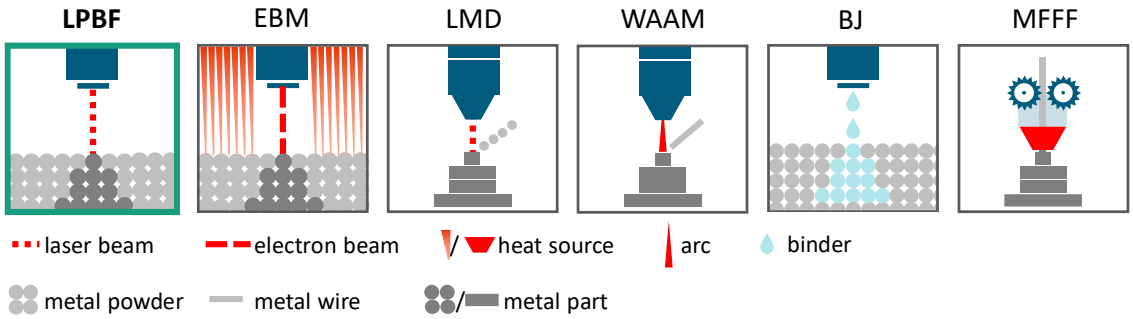

Figure 3-1: Schematic drawing of AM technologies: LPBF, EBM, LMD, WAAM, BJ, and MFFF [17].

The additive build-up allows for the production of complex structures, for material savings with near-net shape designs, and for the integration of functions [13, 18, 19]. Industries such as aviation, space, and automotive benefit from the advantages of LPBF technology. For instance, lightweight alloys are employed in these sectors to achieve weight savings and reduce fuel consumption. The most used lightweight alloys are aluminium and titanium alloys [1, 3, 13], which is why this investigation focuses on these materials. The AM technology used is LPBF, presented in more detail in the following section [20–23].

3.1.1 LPBF

Laser-based powder bed fusion (LPBF) is an iterative process, where metal powder is selectively melted in a powder bed using the energy input of a laser beam (200-1000 W) and then re-solidifies to form a component. The powder is applied from the storage tank to the building platform with a blade. The applied powder layer should be homogeneous and possess a consistent powder density. The quality

of this layer directly impacts part quality, as irregularities cause defects. A laser beam scans the component contour of the respective layer and thus melts the powder [1, 18, 24, 25]. A stereotypical LPBF machine system is displayed in Figure 3-2 (a) and a schematic drawing of the melting track in Figure 3-2 (b).

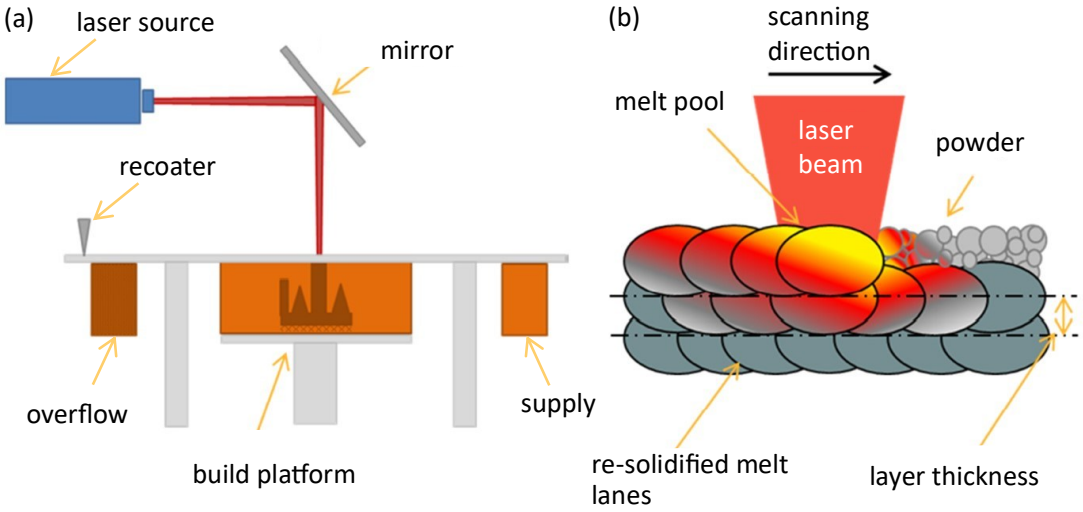

Figure 3-2: Schematic drawing of (a) a stereotypical LPBF machine and (b) LPBF melting track [26].

The entire build chamber is flooded with an inert gas, usually argon or nitrogen, to set the oxygen content to 0.01-0.05 ppm [25]. This prevents oxygen pickup in the part during the process and protects against discharges that trigger explosions. The melted particles re-solidify together to form a component featuring vertical grain growth over multiple layers with densities up to 99.99 % [25, 27]. After scanning each layer, the build platform is lowered to set the targeted layer thickness and new powder is applied [3, 25]. According to Wang et al. and Jing et al. layer thickness from 20-150 µm are used [28, 29]. Overflow powder is collected in a storage container. This powder is sieved to remove spatters and agglomerates to recycle the powder for further usage.

The process parameters laser beam shape and diameter, laser power, scanning speed, hatch distance, layer thickness, pre-heat temperature, blade type and scanning strategy are adapted to the material, the powder, the desired mechanical properties and productivity [30–32]. The interaction of the process parameters with the particle size and their influence on the mechanical properties is described in more detail in Section 3.2.2.2.

3.1.2 Alloys

The chemical composition of the powder determines the chemical composition of the part and therefore its properties. LPBF is similar to a welding process with the melting of the powder and the re-solidification into a component, which is why many LPBF powders are based on welding alloys such as AlSi10Mg, Ti-6Al-4V and 316L [33]. Custom LPBF alloys are developed to increase processability and manufacturability and to achieve the desired mechanical properties [30]. The alloying elements vary in melting temperatures and laser radiation absorptions, leading to different melting behaviour in the process. Boley et al. determined the alloy dependent laser absorption of the materials, with 0.22 for Al and 0.64 for Ti [34].

3.1.2.1 AlMg11

The aluminium alloy AlMg11 features a density of 2.6 g/cm³ and is a precipitation-hardening material. The melting point of aluminium (Al) is 660 °C, while for magnesium (Mg), it is 650 °C [8]. The average strength of this alloys results mainly from solid solution strengthening, in addition precipitation and grain refinement contribute to the strength. Suzuki et al. describe a formation of hierarchical microstructures in LPBF for aluminium alloys [35]. AlMg11 features natural corrosion resistance against seawater. Therefore, it is used in shipbuilding and containers [36, 37]. The full AlMg11-alloy composition is demonstrated in Table 3-1.

Table 3-1: Chemical composition of AlMg11 according to AlMgty80 material data sheet [9].

Al	Si	Fe	Cu	Mn	Mg	Zn	Ti
Rest	< 0,1%	< 0,1%	< 0,05%	< 0,05%	9-11%	< 0,05%	0,011-0,5%

The values from the AlMgty80 material data sheet (in Table 3-2) apply as a reference for the assessment of the achieved mechanical properties.

Table 3-2: Mechanical properties of AlMg11 according to AlMgty80 material data sheet [9].

Mechanical properties	Target values in as-built condition
Yield Strength at 0.2 % $R_{p0.2}$	< 220 MPa
Tensile Strength R_m	> 340 MPa
Elongation A	< 15 %
Vickers Hardness	100-115 HV10

3.1.2.2 Ti-6Al-4V

Ti-6Al-4V features a density of 4.42 g/cm³ and a melting temperature range of approx. 1604-1664 °C [38, 39]. The Ti-6Al-4V extra low interstitial (ELI) Grade 23 features a defined chemical composition with a maximum oxygen content of 0.13 wt.-% and a maximum hydrogen content of 0.012 wt.-%. In comparison, Grade 5 features a maximum oxygen content of 0.20 % and a maximum hydrogen content of 0.015 % [40]. The alloy composition is presented in Table 3-3.

Table 3-3: Chemical composition of Ti-6Al-4V Grade23 – ELI according to ASTM B348 [41].

Powder	Ti in [wt.-%]	Al in [wt.-%]	V in [wt.-%]	Fe in [wt.-%]	C in [wt.-%]	O in [wt.-%]	N in [wt.-%]	H in [wt.-%]
Ti-6Al-4V Gr 23 — ELI	Balance	5.5-6.5	3.5-4.5	≤0.25	≤0.08	≤0.13	≤0.05	0.012

Asherloo et al. describe the microstructure obtained from LPBF as an α'-martensitic, fine needle-like structure in columnar prior β grains and prior β grain boundaries [42, 43]. This structure exhibits a nanoscale β phase (approximately up to 4 %), along with an orthorhombic α'' phase within the Vanadium (V) oversaturated regions [43–48]. Grain growth aligns with the build direction with grains growing several hundred micrometres through re-melting of previous layers [42, 49, 50]. Thijs et al. identify a β-columnar structure with a 90° scanning pattern rotation in LPBF [42].

A desired microstructure is formed in situ with an adapted process parameter combination or ex-situ with heat treatment [43]. In situ: Xu et al. decrease the layer thickness from 90 µm to 30 µm, which results in finer grain structure of average 15 µm instead of an average of 70 µm. With an increased hatch distance from 0.12 to 0.18 mm, the energy density is reduced from 50.62 to 33.74 J/mm³, which forms a dominant α' martensite phase instead of ultrafine lamellar (α+β) [51]. Ex situ: Heat treatment: Yadroitsev et al. show that to influence an anisotropic characteristic, the β-transus temperature of around 980-996 °C must be reached, which allows for a phase re-nucleation [52–55]. A heat treatment between 760 °C-850 °C transforms the α'-martensite into an acicular α-phase inside prior β-grain boundaries [56]. With a heat treatment of 800 °C for 2 h, Sallica-Leva et al. achieve an increase in ductility from 8.5 to 11 %, due to a full decomposition of martensite and a refinement of microstructure [57]. Strengthening mechanisms in Ti-6Al-4V include strain hardening, solid solution strengthening, precipitation hardening, and grain refinement [37].

As a reference for industry standard, the mechanical properties presented in VDI 3405 part 2.4 are used. For a more comprehensive interpretation of the findings in this thesis, published values from Xue et al., EOS Optical Systems GmbH and Nikon SLM are referenced, as presented in Table 3-4 [10, 50, 58, 59]. The properties obtained in this study are compared to these references to assess if industry standards are met. The results depend on various factors, including the type of machine used, process parameters, and heat treatment, and are therefore only transferable to a limited extent.

Table 3-4: Mechanical properties of Ti-6Al-4V based on literature review [10, 50, 58, 59].

Study	**Heat Treatment**	***LT*** in [µm]	R_m in [N/mm²]	$R_{p0.2}$ in [N/mm²]	***A*** in [%]	**Hardness**
VDI 3405 part 2.4 (min. value)	843 °C 4.5 h	/	990	898	12.4	HV10 339
Xue et al. (horizontal)	800 °C 2 h	60	1029	956	14.3	/
Xue et al. (vertical)	800 °C 2 h	60	1041	978	16.2	/
EOS (horizontal)	800 °C 2 h	40	1050	940	14	/
EOS (vertical)	800 °C 2 h	40	1050	980	15	/
Nikon SLM (horizontal)	940 °C 4 h	60	987	894	12	307 HV10
Nikon SLM (vertical)	940 °C 4 h	60	991	905	15	

3.1.2.3 Humidity and Oxygen

Powders tend to absorb moisture, e.g. the relative humidity (RH) of the atmosphere in the form of H_2O, which forms liquid bridges between the particles [60]. Weiss et al. expose AlSi10Mg powder for 14 h and a temperature of 50 °C to a relative humidity of 80 %. They measure an increase in moisture content from 0.084 wt.-% in the as-received-state to 0.098 wt.-% after exposure, corresponding to an increase of one sixth [61]. Cordova et al. expose Ti-6Al-4V powder to the atmosphere for 72 h at 50 °C and 80 % RH and measure an increase of 0.035 wt.-% in moisture content [60]. The same exposure for AlSi10Mg results in an increase from 0.057 to 0.437 wt.-%.

This shows, that an uptake of H_2O is dependent on the alloy, the exposure to relative humidity, and exposed time, and temperature [62, 63]. In tendency, moisture uptake increases if relative humidity

increases, exposure time increases and temperature increases. Weiss et al. measure an increase in avalanche angles from 47° to 49° for AlSi10Mg after exposing it for 14 hours to 80 % RH in 50 °C [61]. Agglomerates are formed, which reduces flowability [61, 64]. An oversaturated melt causes so-called hydrogen porosity [65–67]. Either dissolved hydrogen is precipitated during the re-solidification of the melt or the metal oxides are reduced by the hydrogen with the formation of water vapour [68].

Seyda et al. investigate the impact of oxygen content in the powder on the static mechanical properties of Ti-6Al-4V. A powder with an oxygen content of 0.073 wt.- % achieves a tensile strength of 1020 MPa, an elongation of 7 % and a hardness of 360 HV1. In comparison to a powder with a higher oxygen content of 0.139 wt.- %, that exhibits a tensile strength of 1100 MPa, an elongation of 4.5 % and a hardness of 390 HV1. An increased oxygen content leads to a higher tensile strength, a higher hardness and a reduced ductility. [69, 70]

The oxygen contents of different PSDs are investigated by Xiongfei et al. for Ti-6Al-4V, who observe an oxygen content below 1000 µg/g for 45-150 µm and about 1500 µg/g for particles below 45 µm, due to higher specific surface area of the smaller particles [7]. Balbaa et al. measure the oxygen content of AlSi10Mg parts produced with 5-15 µm and 20-56 µm PSD. The smaller powder features up to 35 wt.- % oxygen content, which is 30 wt.- % more than the 5 wt.- % oxygen content of the larger powder [20].

3.2 Metal Powder for LPBF

Metal powders are a frequently used feedstock material in AM, they are utilized according to ISO 52900 in the processes EBM, DED, BJ and LPBF [1, 71]. In the following section, an overview of the state-of-the-art of metal powders for LPBF is presented. The material life cycle of the metal powder serves as the framework for this section. Initially, atomization technologies of the powders used are explained. Subsequently, the powder characteristics affecting LPBF and part properties are described.

3.2.1 Powder Atomization

Metal powder is produced through solid state reduction, mechanical grinding, atomization, electrolysis or chemical processes [71]. The production process determines the powder's characteristics, which influence the physical, mechanical, and microstructural properties of the printed component [69, 71, 72]. Key characteristics include morphology, density, particle size and distribution, flowability, and chemical composition [73].

The atomization technologies differ in their raw materials, melting technology (heat element or plasma torch), the nozzle designs and the atomization medium used, such as gas (GA), water, plasma. [71, 74]. The powders investigated in this work are produced via gas atomization and plasma atomization, as shown in Figure 3-3.

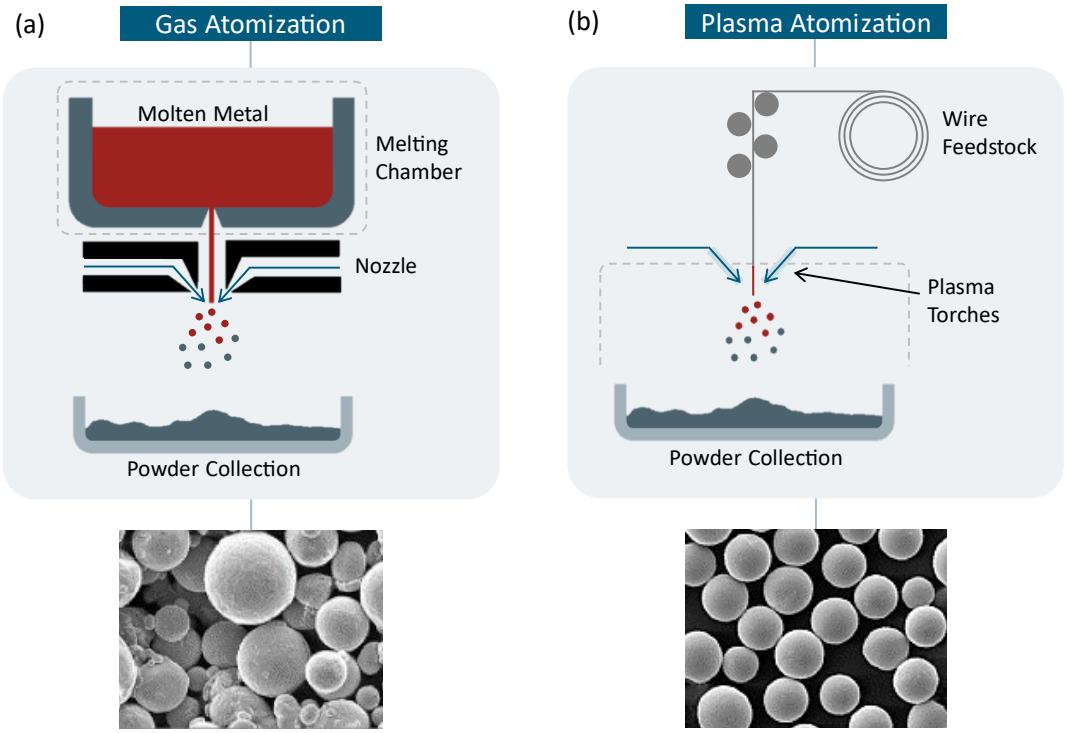

Figure 3-3: Schematic drawings for (a) gas atomization and (b) plasma atomization and exemplary SEM images of the resulting powders [74, 75].

Qi et al. report an atomization yield of 10 % for a gas atomized PSD range of 20-70 µm for FeCrNiBSiNb [5]. Anderson and Terpstra achieve with gas atomization an atomization yield of 50 % for the same PSD for 316L [6]. Xiongfei et al. investigate plasma rotating electrode process (PREP) with 10 % atomization yield for a PSD below 45 µm and electrode induction guiding gas atomization with 35 % [7]. Exemplary cumulative particle diameters for gas atomization from Qi et al. and Anderson and Terpstra are shown in Figure 3-4, highlighting yields from 20-70 µm. [5, 6]

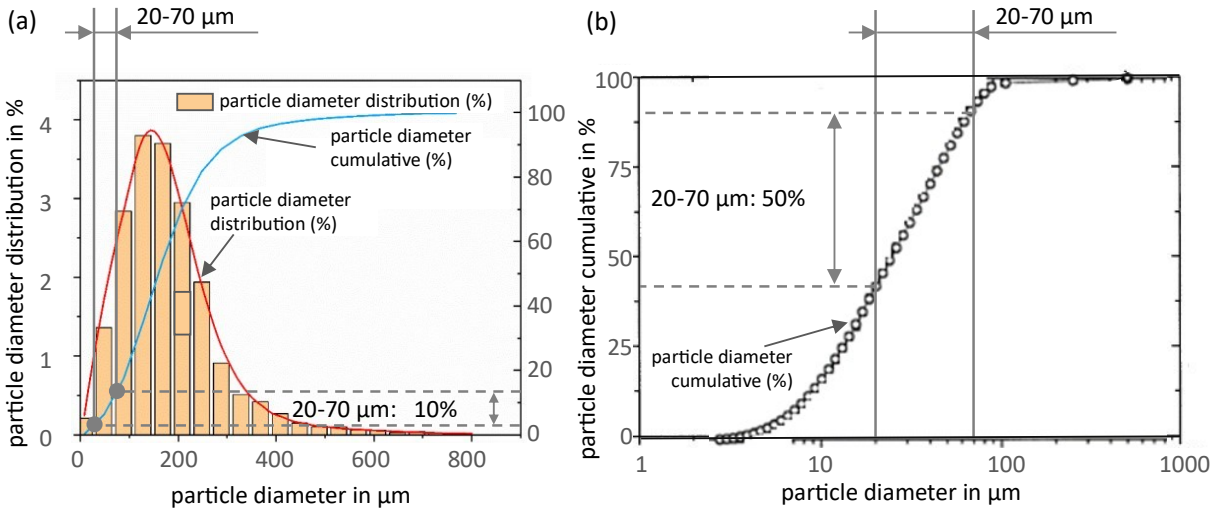

Figure 3-4: Diagrams of particle diameter distributions with GA atomization yields, a) from Qi et al. [5] and b) from Anderson and Terpstra [6].

3.2.2 Powder Characteristics

The characteristics of the powder influence the flowability, therefore the spreadability in the building chamber and thus the mechanical properties of the resulting part [19, 27, 71, 76]. That is why the particle shape, size and flowability are explained in detail in the following sections.

3.2.2.1 Morphology / Particle Shape

Morphology (Greek μορφή morphé — shape, form) is the study of form, shape, and structure [77]. The particle shape is formed during the atomization process and is determined by the technology used as well as the settings during atomization [69, 71]. The particle shapes for LPBF vary between spherical and irregular, as presented in Figure 3-5:

Figure 3-5: Schematic drawings of the particles shapes: spherical and irregular [65].

In 1935, geologist Hakon Wadell defined the term sphericity Ψ, that describes how spherical a body or, in this work, a particle is with the Equation (3-1) [78].

$$\Psi = \frac{\pi^{\frac{1}{3}} * (6 * V_P)^{\frac{2}{3}}}{A_P} \qquad \text{(3-1) [78]}$$

V_P = Volume of a powder particle in m³

A_P = Surface area of a powder particle in m²

The surface of the particle being examined is compared to that of a sphere with the same volume, and the ratio describes the sphericity (Ψ) [78, 79]. A perfect sphere particle features a sphericity of one, irregularities decreasing the ratio. In LPBF, irregularly shaped spatters are formed and ejected from the melt pool. Agglomerates are satellite-shaped clusters of particles that are not materially connected, with a total surface area similar to the sum of individual particles [80]. With interparticle forces, agglomerates are bonding [80, 81]. The particle surface structure exhibits smooth, dendritic, or uneven characteristics.

3.2.2.2 Particle Size and Particle Size Distribution

Metal powder is the feedstock material for LPBF. The powder consists of particles in different sizes, typically indicated by particle diameter and the deciles D10, D50, and D90. These values represent the percentage of particles below the specified value: For example, a D50 value of 45 µm indicates that 50 % of the particles are smaller than 45 µm, with D10 and D90 representing the same for 10 % and 90 % of the particles, respectively. Graphically, the PSD is presented as a frequency distribution, or sum distribution, as demonstrated in Figure 3-6. [82]

Typical PSDs for LPBF are 20-53 µm, 20-63 µm, and 20-70 µm, while a smaller distribution of 15-44 µm is commonly used for steels, oriented to the respective layer thickness [4]. According to VDI 3405 part 2, the maximum particle diameter should be one-third of the selected layer thickness [83]. Meier et al. recommend the smallest layer thickness of two to three times the maximum particle diameter to form a homogeneous powder bed [84]. Most PSDs follow a monomodal Gaussian distribution [50].

Haferkamp et al. state that bimodal distributions do not affect part density [85]. A typical layer thickness for LPBF is between 30-60 µm [25]. Wischeropp et al. demonstrate that the effective layer thickness on top of the part is 4-5.5 times higher than the levelling height, because of the shrinkage due to re-solidification [26].

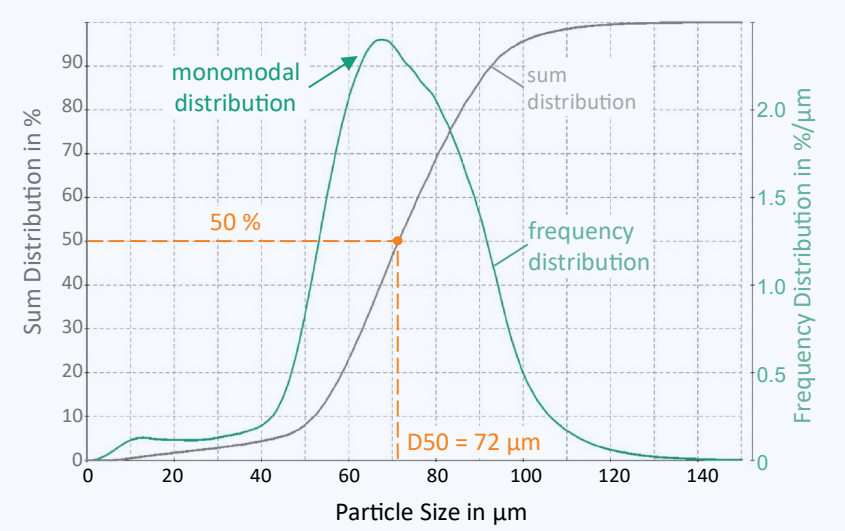

Figure 3-6: Diagram of a frequency and sum distribution of a Ti-6Al-4V 45-106 µm powder based on own measurement.

To produce dense parts (above 99.5 % relative density), Rausch et al. increase the line energy[7] from 60 J/m for 30 µm mean particle diameter to 67 J/m for 90 µm mean particle diameter for Ti-6Al-4V [86]. This finding aligns with Spierings et al., who demonstrate a relationship between the required volumetric energy density (VED) and the PSD: to achieve a relative density above 99.0 %, the VED is 20 J/mm³ higher for a D50 of 37 µm compared to a D50 of 15 µm [3]. Zhang et al. investigate the scanning track dimensions and identify that for a powder with a D50 of 5 µm, the track width is 200 µm and the track depth is 205 µm. For a powder with a D50 of 48 µm, the track width is reduced to 165 µm and the track depth to 45 µm, using the same process parameters. This shows a 17.5 % decrease in track width and a 78 % decrease in track depth, with an increase in D50 from 5 µm to 43 µm [87]. Li et al. investigate the melt pool size of AlSi10Mg for increasing laser exposure time. The width increases from 110 to 130 µm and the depth from 40 to 60 µm by increasing the exposure time from 100 to 180 µs [88]. Baitimerov et al. conclude that process parameters should be adapted to the particle sizes [18].

The impact of particle size on the mechanical properties of various alloys is analysed in several studies. Spierings et al. investigate the influence of particle size on the mechanical properties of 316L (1.4404). With a layer thickness of 45 µm, the lowest surface roughness occurs at 50-60 J/mm³ VED, measuring 4 µm Ra for 7-25 µm particles and 7 µm Ra for 15-55 µm particles. Particles up to 55 µm reduce tensile strength from 750 MPa to 600 MPa and yield strength from 650 MPa to 450 MPa, while elongation at break increases from 30 % to 40 %. [27]

[7] $E_L = P_L/v_s$ with the laser power P_L and the scanning speed v_s [86].

Gu et al. identify no significant differences in microstructure for PSDs with mean particle diameters of 30 µm and 38 µm for Ti-6Al-4V printed, using the same process parameters [49].

Xue et al. identify a process window for Ti-6Al-4V with 99.9 % relative density between 33-50 J/mm³ VED for PSDs ranging from 0-53 µm to 15-105 µm. The surface roughness on a 45° up-skin surface is 8.66 µm with a PSD of 15-53 µm compared to 9.88 µm with a PSD of 15-105 µm. [50]

Balbaa et al. report that AlSi10Mg with 5-15 µm powder results in 57 % larger cell sizes compared to 23-67 µm powder. They attribute this difference to higher absorptivity of the smaller particles, which increases the melt pool temperature and decreases the cooling rate. The relative density of the smaller powder is 95 % compared to 99 % of the larger powder. [20]

The studies indicate that PSD significantly influences the powder bed quality, melt pool characteristics, and mechanical properties in LPBF processes.

3.2.2.3 Flowability

Flowability refers to the ease with which a powder begins to roll and slide due to gravity, without other external forces (gravity excluded) [89]. When gravitational forces outweigh interparticle forces, the powder slips. [8]Approximately 80-90 % of interparticle forces are generated by Van der Waals forces [91]. In addition, hydrogen bonds, electrostatic and magnetic effects contribute to interparticle forces [92]. Relative smaller particles feature a higher specific surface area and lower weight, leading to increased interparticle forces relative to gravitational or resistance forces. Consequently, as the particle size decreases, the interparticle forces increase in relation to gravitational or resistance forces. While an exact determination of interparticle forces for the powders investigated is beyond the scope of this thesis, a relative comparison is employed instead. For more details on the calculation of interparticle forces, see Castellanos [93].

In LPBF, spreadability describes the powder's ability to form an even and dense powder layer[9] during recoating [27, 94]. Therefore, flowability is a key indicator of a powder's spreadability for LPBF. Meier et al. state that an even powder package stabilizes the melting area, avoiding irregularities in the part [70]. To accurately assess flowability for LPBF powders, it is essential to select methods that closely mimic the powder's spreadability during the process. Although powder flowability depends on particle properties, it is also influenced by the powder's interaction with its environment [69]. Given the various physical characteristics that affect flowability, a comprehensive understanding of powder characteristics and their movement, as well as different characterization methods, are necessary [69, 95, 96]. Typical techniques include optical evaluation, apparent and tapped density, Hausner ratio, Hall flowability, avalanche angle, cohesion, surface fractal analysis, powder rheology, and shear tests [69]. Each technique applies distinct stresses to the powder, yielding condition-specific results. That is why multiple flowability measurements are applied [96]. When comparing the values among each other, a higher value means a lower flowability because more interparticle forces must be overcome.

[8] Haferkamp et al. identified a higher Hausner ratio of 1.11 for AlSi10Mg, which features a lower density of 2.67 g/cm³, compared to a Hausner ratio of 1.05 for 316L, which features a density of 8 g/cm³ [90]. This demonstrates how chemical composition affects the Hausner ratio.

[9] Powder Layer Density (PLD): 53-56 % for Ti-6Al-4V according to Wischeropp et al. [26].

3.2.2.3.1 Influence of Particle Size on Flowability

Xue et al. investigate the influence of particle size on the flowability and processability of Ti-6Al-4V powders. They identify that the apparent and tapped densities are higher for the 15-105 µm powder, at 2.41 g/cm³ and 2.92 g/cm³, respectively, compared to 2.3 g/cm³ and 2.84 g/cm³ for the 15-53 µm powder. The larger particles (above 53 µm) fill in between the smaller particles (below 53 µm), reducing overall interparticle forces and resulting in enhanced flowability. A broader particle size span of 90 µm seems sensible in terms of higher powder density. [50]

Habibnejad-korayem et al. identify the highest flowability for a 45-106 µm Ti-6Al-4V powder, with an apparent density of 2.61 g/cm³, tapped density of 2.77 g/cm³, a Hausner ratio of 1.06, and a cohesion index of 5.8. The lowest flowability exhibits a 15-75 µm powder, with an apparent density of 2.56 g/cm³, tapped density of 2.83 g/cm³, a Hausner ratio of 1.11, and a cohesion index of 9.5. [97]

Baitimerov et al. compare two AlSi12 powders, both atomized with gas from different suppliers. The powder with a PSD of 24-71 µm features higher flowability, with an apparent density of 1.20 g/cm³ and a Hall flowability of 65.4 s/50g, compared to the powder with a PSD of 17-84 µm, which features an apparent density of 1.28 g/cm³ and a Hall flowability of 72.2 s/50g. The 24-71 µm powder achieves a relative density of 99.4 %, compared to 95.6 % for the 17-84 µm powder, using the same process parameters. The higher flowability influenced the higher density, though no significant differences in microstructure are detected. [18]

Balbaa et al. analyse two AlSi10Mg powders: one with a small PSD of 5-15 µm and one with a large PSD of 23-67 µm. The small powder shows no Hall flowability, while the large powder flows for 76 s/50g through the funnel. The flowability of the large powder results in a 21 % higher powder bed density of 53 % compared to the small powder. [20]

These studies collectively suggest that small particles fill the voids between larger particles, enhancing packing density and flowability. Therefore, a mixture of small and large particles is recommended to exploit the advantages of both sizes and mitigate the negative properties for compactibility. This conclusion counters the idea of using ever smaller powders to achieve thinner and smoother layers, thus challenging the notion that smaller powders lead to lower surface roughness of components. [3, 98, 99]

3.2.2.3.2 Influence of Particle Shape on Flowability

The influence of particle shapes on flowability is investigated by Haferkamp et al., who compare powders with similar PSD and different particle shapes to their flowability and packing density. For 1.4404, the lowest sphericity of 0.68 in a water-atomized powder results in a Hausner ratio of 1.24. In contrast, an almost spherical PREP-atomized powder with a sphericity of 0.99 features a Hausner ratio of 1.05. The lower packing density leads to a reduced part density of 98.1 % compared to 99.4 %, despite using the same process parameters. In a similar measurement with AlSi10Mg, the powder with the highest sphericity of 0.98 features a Hausner ratio of 1.11 and a part density of 98.4 % with a D50 of 38 µm. The powder with the lower sphericity of 0.94 and a Hausner ratio of 1.13 achieves a higher part density of 98.6 %, with a D50 of 48 µm. This shows a clear correlation of higher sphericity and higher flowability, but no clear correlation between sphericity and part density. [90]

Brika et al. investigate three Ti-6Al-4V powders, all within the PSD range of 20-50 µm. The powder with a sphericity of 0.91 features a Hausner ratio of 1.07 and a part density of 99.5 % at 30 µm layer thickness and 99.3 % at 60 µm. The powder with a sphericity of 0.97 yields a relative density of 99.8 % at 30 µm and 99.5 % at 60 µm. Both studies indicate that more irregular powders tend to exhibit lower flowability, leading to reduced densities. [73]

Chu et al. compare two AlSi10Mg powder batches, one spherical (qualitatively analysed via scanning electron microscope (SEM) images) with 20-55 µm PSD and one irregularly shaped with attached satellites and a PSD of 22-68 µm. The spherical powder, with a repose angle of 39° and cohesion stress of 0.3 kPa, features an enhanced flowability in contrast to the irregularly shaped powder with a repose angle of 41° and cohesion stress of 0.4 kPa. With a VED of 69 J/mm³, the spherical powder yields a higher part density of 99.9 % compared to 99.8 % for the irregularly shaped powder. With a VED of 84 J/mm³, the relative density of the spherical powder is 99.6 % and the melt pool is overall smaller: 53 µm height and 144 µm width compared to 98.3 % relative density of the irregularly shaped powder with a 62 µm melt pool height and 166 µm melt pool width with a VED of 69 J/mm³. [31]

In tendency, smooth and regular-shaped particles reduce the particle contact points and minimize the frictional forces, leading to higher flowability and homogeneous packing properties that stabilize the melting zone. Irregularly shaped particles cause geometric snagging, leading to uneven powder layers. This results in variations in energy absorption and laser reflection, negatively affecting part density. [19, 22, 71, 100–102]

3.2.3 Research Needs for Increased Particle Sizes

Within the identified literature, listed in **Table 3-5** and Table 3-6, there are several gaps in the systematic investigation of PSDs above 70 µm for LPBF. Current studies largely focus on typical PSDs and do not address process parameter adaptations to PSDs for the analysis of mechanical properties or the use of up-to-date LPBF machines. The atomization yield of 10-50 % for LPBF powders and the restricted material selection further highlight the need for research into larger PSDs. Closing these gaps aims to improve resource efficiency and reduce costs in AM.

Table 3-5: Literature review I — studies on increased PSDs [18, 49, 84, 86, 103–105].

Author	Year	Material	Parameter Adaptation	PSDs	Used System	Gap
Alfaify	2019	Ti-6Al-4V 316L	Yes	Ti-6Al-4V: 20-50 µm; 45-80 µm, 50-105 µm 316L: 20-45 µm; 30-80 µm	- Renishaw AM250 - 200 W - Fibre laser with pulsed laser wave	- Pulsed laser radiation - No aluminium alloys - No wide PSD
Baitimerov	2018	AlSi12	Yes	24-70 µm; 17-85 µm; 22-94 µm	- 3D Systems DM125 - 200 W - Fibre laser	- Low laser power - 20-100 µm with low apparent density (not a suitable powder)
Gu	2014	Ti-6Al-4V	Yes	20-50 µm and 4-10 µm	- EOS DMLS M270 - 200 W	- No coarse particles - No aluminium alloys
Marchetti	2021	17-4 PH 316L	/	63-106 µm	- Only flowability characterization	- Only steel alloys - No LPBF processing - No particles <63 µm
Meier	2019	Ti-6Al-4V	Yes (layer thickness)	D50: 34 µm and 17 µm	- DEM Simulation	- Only recoating simulation - No practical validation
Rausch	2019	Ti-6Al-4V	Yes	D50: 58.7µm + 30 µm, +60 µm, 90 µm	- Simulation (SAMPLE2D)	- No practical validation - No 3D simulation - No aluminium alloys
Riener	2020	AlSi10Mg	Yes (scanning speed)	32-63 µm, 19-46 µm, 19-61 µm, 28-61 µm (D10 until D90)	- SLM500 - Nd:YAG solid-state laser - 700 W	- No coarse particles - Low parameter variation
Sagar	2020	316L	Yes	D50: 21.1 µm, 34.6 µm, 48 µm	- DEM, CFD and Structural Mechanics Simulation - 100 W, 150 W, 200 W	- No practical validation - No Ti-6Al-4V or aluminium alloys

Table 3-6: Literature review II — studies on increased PSDs [3, 24, 50, 69, 87, 106–108].

Author	Year	Material	Parameter Adaptation	PSDs	Used System	Gap
Seyda	2017	Ti-6Al-4V	No	20-53 µm and 20-63 µm	- EOS M270 - 200 W - Fibre laser	- No coarse PSD
Sendino	2023	Inconel 718	No	D50 ca. 25-40 µm	- Renishaw AM400 - 200 W	- No mech. properties - No Ti6Al or aluminium alloys
Spierings	2011	316L	Yes (scanning speed)	7-24 µm, 20-40 µm, 15-55 µm	- Concept Laser M1 - 104 W - Nd: YAG solid-state laser	- No coarse or wide PSD - No Ti-6Al-4V or aluminium alloys
Spurek	2021	316L	No	Max. 50-70 µm (monomodal powders)	- Renishaw AM250 - 200 W pulsed laser	- No coarse and wide PSD - No parameter adaptation - No Ti-6Al-4V or aluminium alloys
Xue	2023	Ti-6Al-4V	Yes	0–53 µm, 15–53 µm, 15–75 µm and 15–105 µm	- Bright Laser Technologies BLT S210 - 200-400 W - Ytterbium fibre laser	- No hatch variation - Tensile specimen without parameter adaptation - Low flowability for powders
Young	2022	Ti-6Al-4V	No	Range between 15-25 µm and 35-48 µm	- Test set up - 364 W	- No coarse particles - No transfer to manufacturability - No investigation of mech. properties
Zhang	2019	Tungsten	Only melt pool analysis	(a) D50 = 5.7 µm; (b) D50 = 22.47 µm; (c) D50 = 37.26 µm; and (d) D50 = 47.63 µm	- Not mentioned - 500 W - YLR-500 ytterbium fibre laser	- No mech. properties - No Ti-6Al-4V or aluminium alloys

3.3 Powder Blending

Powder blending is presented as a method of PSD generation. Blending of two powders is classified as solid-solid blending. As the only blending category used in this investigation, it will be referred to as "blending" in the following. Blending of several powders represents a basic operation of mechanical process engineering. Blending aims to homogenize the powders to a complete random state [109–111]. Furthermore, blending processes are classified concerning their conveying directions (axial, radial and tangential) [112].

3.3.1 Solid-Solid Blending

The blending of two powders presupposes a movement of particles. The movement is subdivided in terms of its spatial extent. A distinction is made between convection and dispersion, analogously classified as coarse blending and fine blending. The two forms of blending take place at the same time and overlap. Their transition to each other is fluid. In Figure 3-7, the blending processes are shown schematically after an initial blending. Filled and blank dots represent particles of two powders (powder A and powder B). [113]

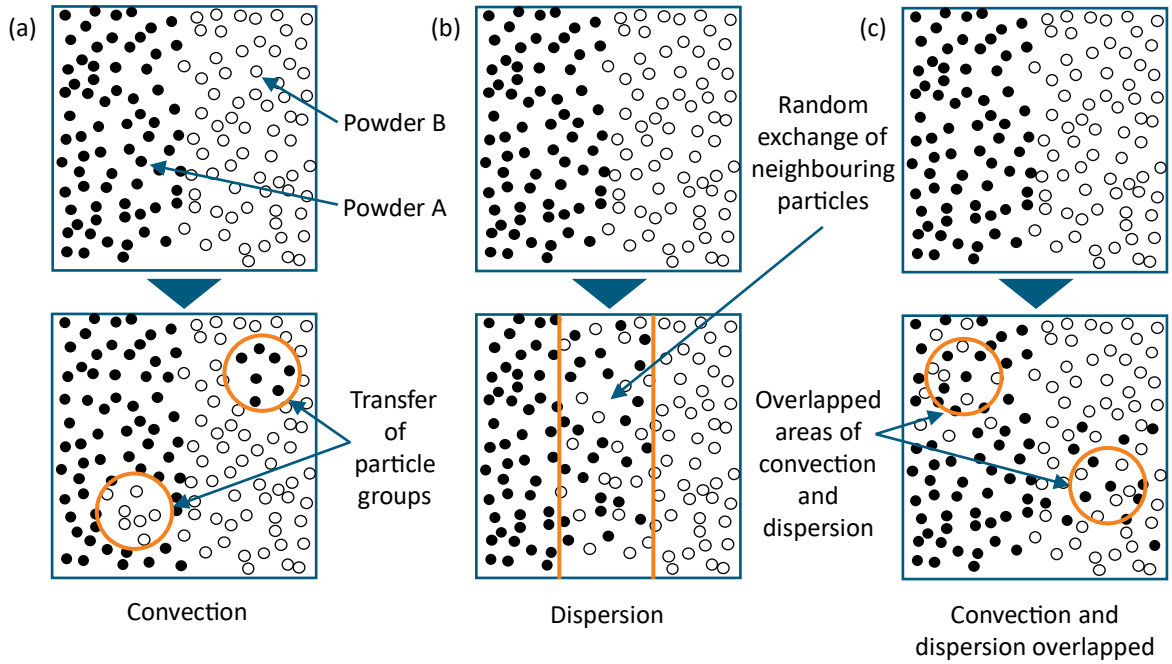

Figure 3-7: Schematic drawing of (a) convection, (b) dispersion, and (c) convection and dispersion overlapped mechanisms during blending [113].

Convection refers to the transport of particle groups within the blending chamber. The separation of the material takes place at random points. In this way, the size of the single-powder groups is gradually reduced. There are completely segregated phases at the beginning of the blending process. Convection increasingly abolishes the separation of the phases. This results in randomly distributed groups of smaller initial components. [113]

Dispersion works alongside dispersion blending. This form of blending is described as dissolving the boundaries of the groups. Dispersion takes place at the particle level. Through the random exchange of neighbouring particles, the boundaries between the groups of the same powder are blurred. The range of dispersion is limited to the neighbouring particles. The effectiveness of dispersion therefore increases as convection progresses, increasing the number of particles in adjacent positions to particles

of other components. The effectiveness of fine blending also determines the achievable blending quality. [113]

3.3.2 Segregation

The homogeneous random distribution as a blending result is subjected to potential segregation. Influencing factors are particle interactions, which reduce the free particle movement. Differences in particle size, shape, and density are decisive for the intensity of segregation [111, 113, 114]. According to Weinekötter and Gericke, the particle size is supposed to exert the biggest influence [113]. A difference in particle size of 1:1.3 leads to segregation, which is intensified by increasing size ratio. Cohesive interparticle forces reduce the particle-ratio-effect. Segregation occurs at any time due to different mechanisms separately or, more likely, multiple parallel mechanisms [89]. A blend container design that enforces re-blending while emptying the container, such as one using mass flow, prevents it [89]. Segregation is not to be equated with over-blending, which leads to a deterioration of material characteristics [111]. The two segregation effects that are most relevant for this work, slip-of-slope and percolation, are presented in Figure 3-8:

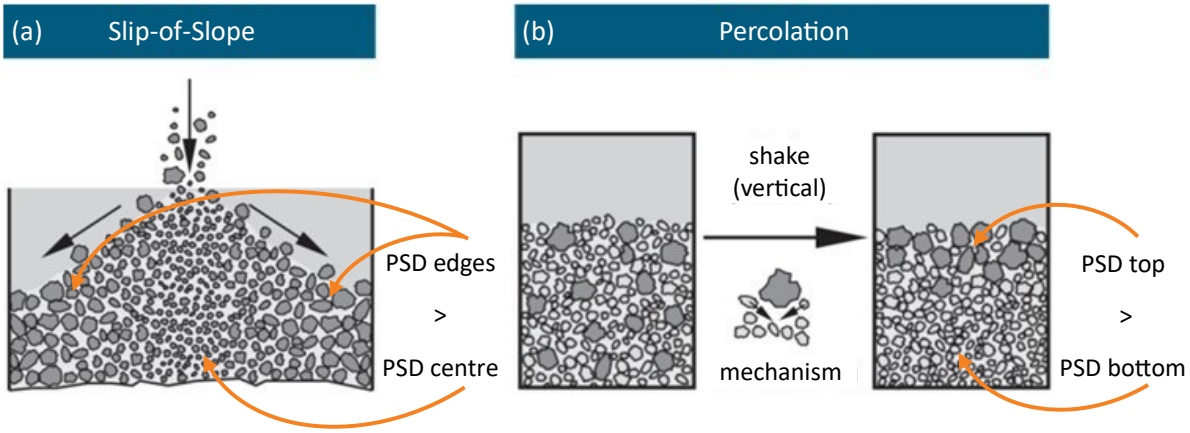

Figure 3-8: Schematic drawings of segregation mechanisms: (a) slip-of-slope and (b) percolation [89].

1) Slip-of-Slope

Particles of different sizes exhibit variations in their momentum and cohesion. When a flowing powder impacts a heap, the smaller particles, with relatively lower momentum, tend to settle directly below the point of impact. In contrast, the larger particles, with relatively higher momentum, accumulate at the outer edge of the heap, as demonstrated in Figure 3-8 (a). This phenomenon is known as the slip-of-slope effect or momentum segregation. [111]

2) Percolation

During the movement of a powder, particles interact and create gaps between each other. Particles fitting into the gaps preferentially flow into these. Since gravity is the dominant external force in most powder applications, the relatively smaller particles drift downwards within the moving powder. This effect. Known as percolation or sifting, is demonstrated in Figure 3-8 (b). [89]

3.3.3 Research Needs for Powder Blending

For PSD generation, a homogeneous powder blend is crucial. Irregularities in particle sizes lead to varying interparticle forces and flowabilities. These irregularities affect the applied powder layer, causing

defects in the final part. Currently, powder blending plays an inferior role in the powder handling for LPBF. In Table 3-7, an overview of the blender utilization for LPBF is presented.

Table 3-7: Literature review – studies with Powder Blenders for LPBF [24, 85, 115–121].

Author	Year	Blender	Purpose	Research Gap
Churu	2022	Mechanical blender (Custom made at Stellenbosch University – South Africa)	- Alloy fabrication - 15 min at 65 rpm	- Focus on comparing the homogenization progress of different powder mixtures during solid-state sintering.
Haferkamp	2021	Rotating cylindrical drum	- Generating different PSDs - 2 h	- Qualitative verification → no quantitative verification - No differentiation between powder batches
Huang	2022	Tubular rotation	- Alloy fabrication	- No blending grade analysis
Ma	2023	Biconical mixer	- Alloy/Powder fabrication - 4 h blending	- Compacts made of blends - No typical blending process of two similar powders
Medina	2013	Powder mixing machine (Tumbler)	- Fabrication of low-cost powder of different particle shapes - 5 min blending time	- No detailed information about blending process - No blending of two spherical powders
Parker	2021	3D Turbula® mixer	- Alloy fabrication - Mixed in plastic container in Ar with - 250 rpm for 15 min - 200 rpm for 20 min	- No quantitative analysation of blending grade - Focus on powder quality
Thamae	2023	Rotary multiple-tube batch mixer	- Alloy fabrication - Analysing blending result	- No further information on blending process - Verification via powder qualities
Young	2022	Turbula Mixer (WAB, Allendale, NJ, USA)	- Generating different PSDs	- No further information on blending process

The review demonstrates the limited information available on powder blending for LPBF. The selection process for powder blenders is not addressed in the identified literature. With the frequently used plastic containers, there is a risk of abrasion, which leads to contamination. Furthermore, there is rarely a quantitative analysation of the blending grade. Only a few studies, such as those from Haferkamp et al. and Thamae et al., investigate the influence of the blending process on powder quality. [90, 121, 122]

Therefore, in this work, the blending of AM powders for PSD generation is analysed using a self-developed V-blender. A powder marking method is developed to validate the blending grade for different blending times and different rotational speeds, aiming to address the research gaps in powder blending for LPBF.

4 Experimental Setup

In this chapter, the investigated PSDs and the experimental setup are presented, including the PSD generation, the analysis of the powder characteristics, the adaption of process parameters and the subsequent mechanical testing.

4.1 Particle Size Distribution Generation

Two alloys are investigated using different approaches: AlMg11, which represents powders specifically atomized for LPBF, and Ti-6Al-4V, which represents high-cost powders. The investigation of AlMg11 primarily focuses on determining the highest atomization yield that is processable in LPBF from a defined range of six powders, as presented in Table 4-1, including the respective atomization yields[10]. The PSDs encompass small and large particle sizes ranging from 20 µm to 170 µm, as well as narrow (25 µm) and wide (150 µm) particle size spans. For LPBF, the reference powder is distributed within the PSD range of 20-70 µm (LPBF_20-70). To generate various PSDs, the excess oversize powder with 70-170 µm (OVS_70-170) is utilized. The two base powders, LPBF_20-70 and OVS_70-170, are blended using a self-developed V-shape tumbling blender (V-blender) and then sieved to achieve the desired PSDs. The selected PSDs are aligned with standard sieving mesh sizes of 45 µm, 80 µm, 100 µm, and 125 µm.

Table 4-1: Overview of AlMg11 powder nomenclature, target PSD, atomization yield, and the base powders used for PSD generation.

Powder Nomenclature	**Target PSD** in [µm]	**Atomization Yield** in [%]	**Base Powders**
LPBF_20-70	20-70	43	/
OVS_70-170	70-170	47	/
PSD1_20-45	20-45	24	LPBF_20-70
PSD2_45-70	45-70	21	LPBF_20-70
PSD3_70-125	70-125	31	OVS_70-170
PSD4_20-100	20-100	62	LPBF_20-70 + OVS_70-170
PSD5_20-125	20-125	74	LPBF_20-70 + OVS_70-170
PSD6_20-170	20-170	90	LPBF_20-70 + OVS_70-170

Second, the cost-saving potential for LPBF-users is analysed using Ti-6Al-4V. A typical LPBF PSD for Ti-6Al-4V of 20-53 µm is used as a reference and compared with an EBM-PSD of 45-106 µm, which represents the lower-cost powder. Additionally, both PSDs are blended with the V-blender and sieved at 100 µm. This approach allows for a comparison with the results from the AlMg11 investigations and reflects the higher atomization yield in the Ti-6Al-4V tests. The nomenclature and a basic description of the powders are given in Table 4-2:

[10] Atomization yields are determined from PSD measurement of the entire atomization batch, as shown in Figure 3-4.

Table 4-2: Overview of Ti-6l-4V powder nomenclature, target PSD, and the base powders used for PSD generation.

Powder Nomenclature	Target PSD in [µm]	Blended/Sieved with
LPBF_20-53	20-53	LPBF
EBM_45-106	45-106	EBM
Ti64_20-100	20-100	LPBF + EBM

4.1.1 V-shape Tumbling Blender

A tumbling blender with a V-shaped container is developed and manufactured for this investigation. The initial technical drawing, the Computer-Aided Design (CAD) model and the final manufactured blending rig, is illustrated in Figure 4-1.

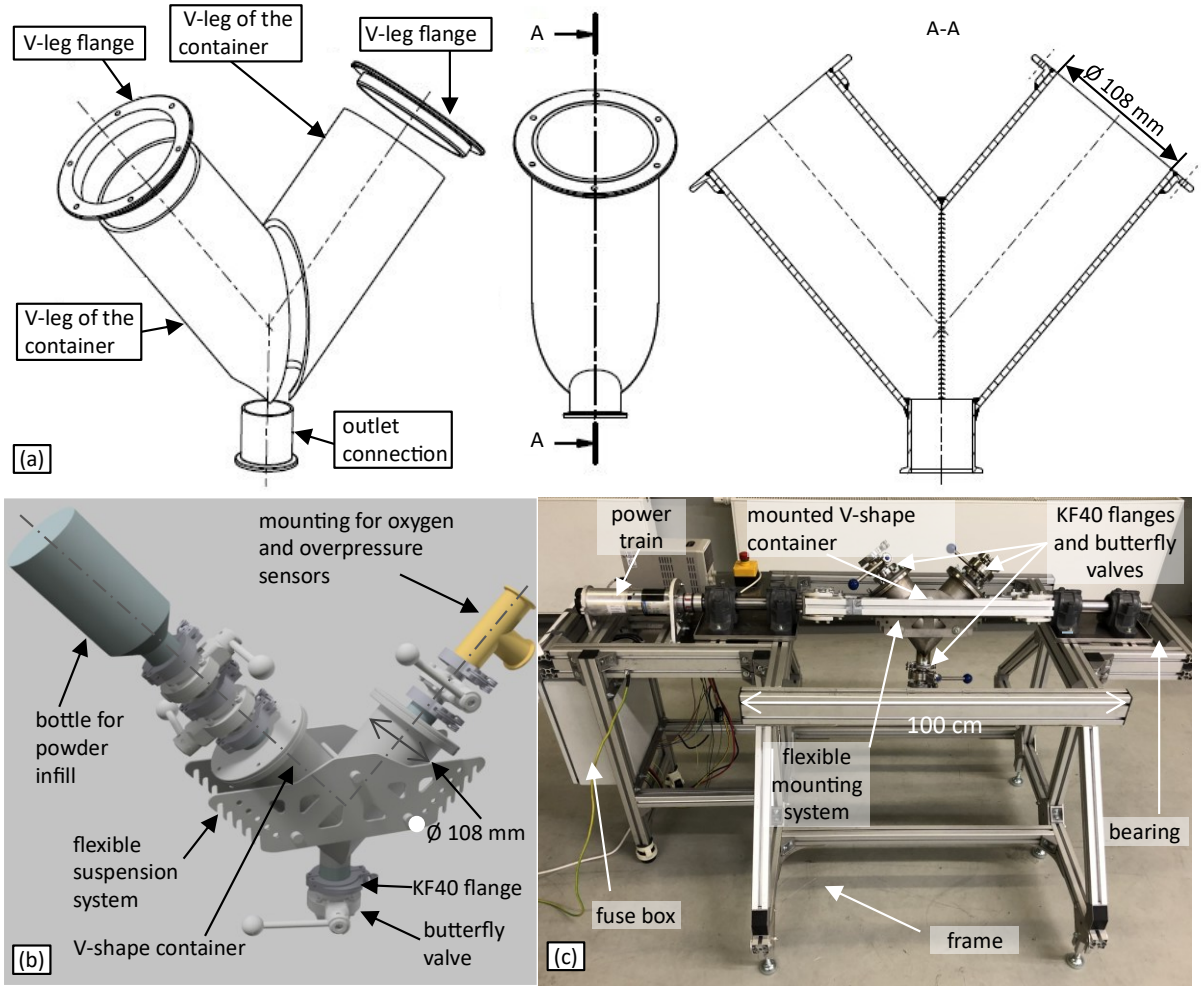

Figure 4-1: a) technical drawing of the V-shape container and its cross-section; b) CAD-Image of V-shape container with integrated mountings and c) image of manufactured blender test rig.

The systematic approach of the selection process for a V-shape blender is described in the Appendix A.3. The V-shaped container features a total volume of 3 l, corresponding to 2.1 l at a recommended filling level of 60-70 % [111]. The container is filled with 99.996 % argon gas until the oxygen concentration inside is reduced to below 5 %. The powder is filled into the container using a powder

bottle, which is connected via KF40 flanges and two butterfly valves secured by clamps to ensure leak-free filling. Additionally, the same connection features used for the powder bottle are employed to mount oxygen and overpressure sensors on the other V-leg of the container (see Figure 4-1(b)).

4.1.2 Powder Marking

To validate the blending grade, it is essential that the powders remain distinguishable after the blending process. Powders are distinguishable by characteristics such as size, shape, alloy, density, or colour. The selected characteristic for distinction should not affect the blending behaviour. In this case, colour is chosen due to its high visibility and minimal impact on powder properties and flow behaviour. Since two batches of the same metal alloy exhibit the same colour appearance, colour differentiation is not feasible for powders of the same alloy.

To produce a distinct colour, thermal oxidation (TO) is employed. Therefore, Ti-6Al-4V powder is placed into a flat bowl to a height of 1 cm, as illustrated in Figure 4-2 (a). The bowl is then heated in a furnace at 550 °C for 2 h in atmospheric conditions[11]. The ambient oxygen concentration of approximately 21 % and the temperature of 550 °C initiate the formation of an oxide layer. The colour variation is dependent on the thickness of this oxide layer: 25-40 nm thickness results in purple hue, 40-50 nm in dark blue and around 60 nm in light blue, as shown in Figure 4-2 (b). The phenomenon is attributed to light interference. Microscopy images of the original and marked Ti-6Al-4V powders are displayed in Figure 4-2 (c) and (d). [123–125]

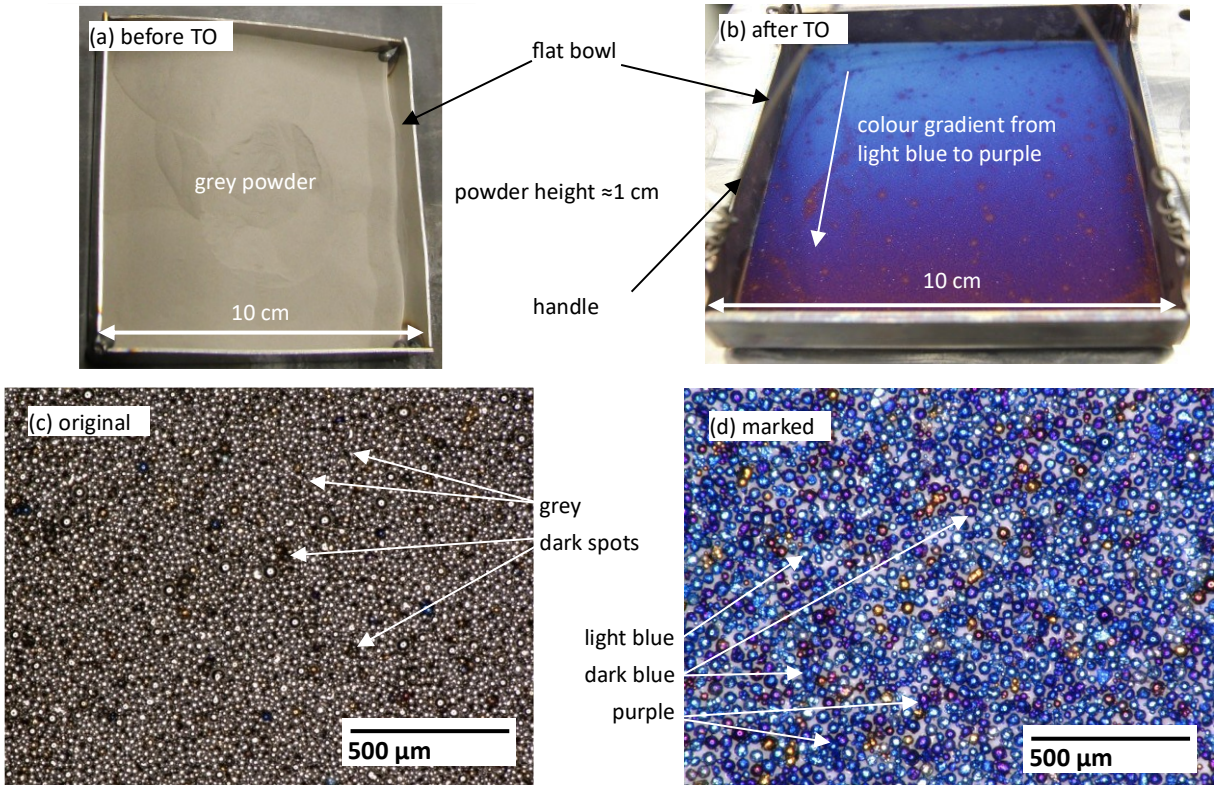

Figure 4-2: (a) Image of flat bowl with original Ti-6Al-4V powder; (b) image of flat bowl with marked Ti-6Al-4V powder; (c) light microscopy image of original Ti-6Al-4V powder; (d) light microscopy image of marked Ti-6Al-4V powder.

[11] Temperature and duration are identified in pre-tests.

4.1.3 Evaluation of Blending Result

To measure the blending result, powder samples are taken and subdivided into five subsamples for statistical analysis. Each subsample is positioned on a double-layered metal plate featuring eight cavities (0.5 mm in depth) on the upper layer. This thin powder layer enables the measurement using a Keyence VHX5000 optical light microscope without introducing any additional medium in the background. The captured images are processed using image analysis software, where they are binarized to differentiate between the marked and original particles. Specifically, each pixel in the image is classified as either a marked or original particle based on an image threshold value of 150 (contrast and brightness). Exemplary original and processed images are presented in Figure 4-3.

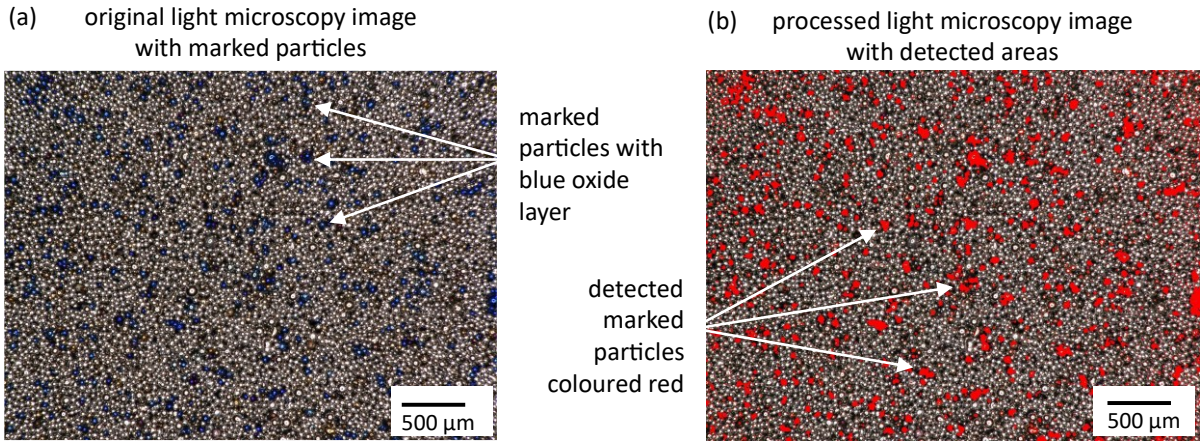

Figure 4-3: (a) Light microscopy image of blended powder with marked particles and (b) processed light microscopy image with detected areas.

4.1.4 Determination of Blending Settings

For the initial blending operation, the blending settings rotational speed and blending time are determined. Ti-6Al-4V powder is separated into three distinct batches, each mixed with 10 % of marked powder at different rotational speeds of 20, 40, and 60 rounds per minute (rpm). The three rotational speeds cover three levels of induced stress on the powder. Systematic sampling is conducted from both the top and bottom of the blending container at 1-minute intervals ranging from 1 to 10 minutes to assess the progression of the blending ratio over time.

The area percentage of marked particles in each image is calculated, and the mean value is compared to the expected 10 % marked particle content. The findings are visualized using a box plot diagram, which displays both the mean values and the distribution of the eight individual results.

4.1.5 Degradation Test

To further ensure the avoidance of particle degradation, the blending settings are tested for their impact on particle characteristics. Therefore, the powders (original and marked) are characterized by size and shape (as described in Section 4.2.1) both before and after an extended blending period of 180 minutes. The target values are calculated using the before-values in the blending ratio of 90:10 of the original and marked powders. The deviation of these calculated target values and the measured after-values determines the degradation through the blending process. The test is performed at the three pre-selected rotational speeds of 20, 40, and 60 rpm. The powder samples are taken at 1-minute intervals for the first 10 minutes, then every 5 minutes for the next 30 minutes. Subsequently, samples

are taken at 1-hour intervals until 180 minutes in total are reached. After 180 minutes, two samples from each V-leg and one from the bottom of the container are additionally taken to analyse particle size and shape from different areas of the container.

4.2 Powder Characteristics

To assess the impact of varied PSDs on LPBF processability and manufacturability of the powders, the key powder characteristics (particle size, particle shape, chemical composition, and flowability) are systematically measured and analysed.

4.2.1 Particle Size and Shape

The particle morphology is analysed using dynamic image analysis according to ISO 13322-2 with the Camsizer X2 from Microtrac Retsch GmbH. A schematic drawing of the Camsizer X2 is presented in Figure 4-4. For the dynamic image analysis, the powder sample is filled into a channel via a funnel and guided evenly to the feed inlet by vibration. The powder falls through a gap in front of a nozzle that disperses the powder with compressed air. The particles are thereby separated from each other and are analysed individually. In a measuring shaft, the particles are captured by two cameras and recorded in greyscale images.

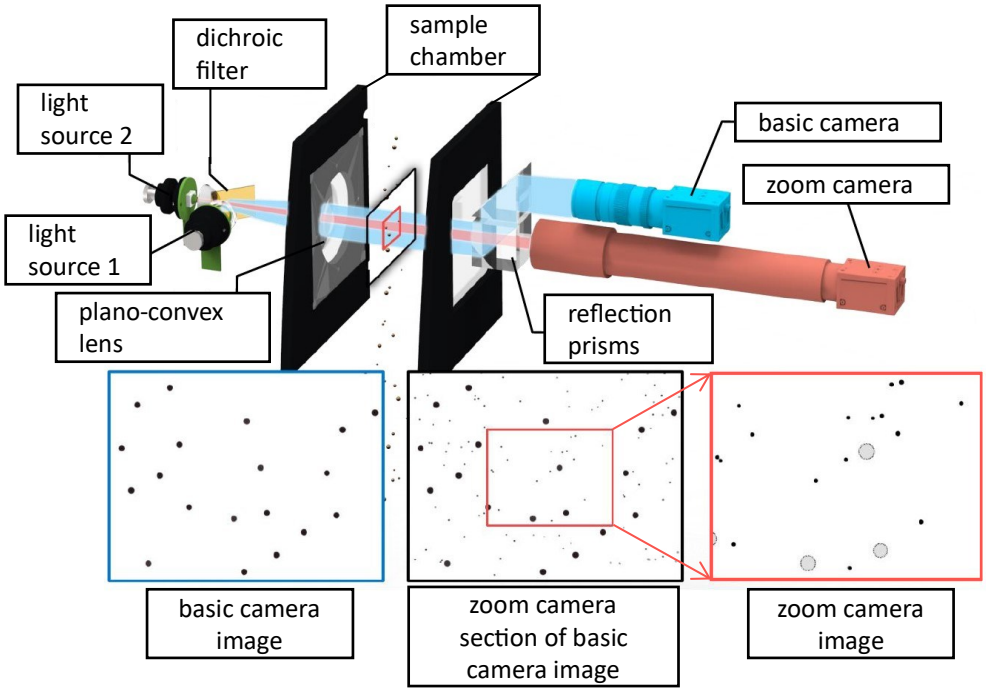

Figure 4-4: Schematic drawing of the Camsizer X2 setup as originally published in [126].

Using algorithms, the images are converted into binary format, where the contours of individual particles are identified by analysing the individual pixels. Based on these contours, the particle size and shape are measured [127]. The diameters used for calculations are described in Table 4-3:

Table 4-3: Overview of diameters used for morphology determination [128].

Diameter	Description
x_{area}	The particle's area *A* is estimated by approximating it to a circle of equivalent size, and the resulting diameter is then assumed
$x_{c\ min}$	Minimum diameter
$x_{Fe\ max}$	Feret -Maximum: Maximum diameter between two parallel tangents

The particle size is indicated in this thesis by the particle diameter x_{area} (Equation (4.1)) [128]. It allows comparing different particle sizes without being falsified by the non-shape of the particles.

$$x_{area} = \sqrt{\frac{4A_P}{\pi}} \quad (4.1)\ [128]$$

The particle size is plotted on the x-axis, the first y-axis shows the cumulative distribution Q(x) and the second y-axis the frequency distribution q(x), which is determined by the derivative of the cumulative distribution (Equation (4.2)):

$$q_r(x) = \frac{d}{dx} Q_r(x) \quad (4.2)\ [128]$$

The PSD is specified within a range, such as 20-70 µm. To confirm that the PSD falls within the declared limits, the D10 and D90 values must lie within this range, with deviations of up to 10 % considered acceptable. The D50 is targeted as the mean value, so for a PSD range of 20-70 µm, a D50 of 45 µm is acceptable, with a deviation of ±5 %. The PSD span, representing the difference between D10 and D90, is also acceptable with a deviation of ±5 %.

The particle shape is determined via the aspect ratio, symmetry, and sphericity with the dynamic image analysis of the Camsizer X2. The aspect ratio is calculated from the width and length ratio of the narrowest chord ($x_{c\ min}$) and the longest measured Feret diameter $x_{Fe\ max}$, as described in Equation (4.3):

$$\frac{w_P}{l_P} = \frac{x_{c\ min}}{x_{Fe\ max}} \quad (4.3)\ [128]$$

The sphericity is determined by the particle area and the particle circumference in Equation (4.4).

$$SPHT = \frac{4\pi A_P}{U^2} \quad (4.4)\ [128]$$

The symmetry is defined in Equation (4.5) from the minimum distances r_1 and r_2 to the centre of the area from several measurements, each perpendicular to the scanning direction:

$$Symm = \frac{1}{2}\left[1 + \min\left(\frac{r_1}{r_2}\right)\right] \quad (4.5)\ [128]$$

In a comparison to the reference powder, a deviation of 5 % in shape values is considered acceptable for similarity. The evaluation of the particles is carried out according to the volume-related index 3. [128, 129]

For detailed analysis of the particle shape across different particle sizes, averaged values from defined size classes are used. Up to 100 µm particle size, the classes are in intervals of 10 µm; up to 150 µm they are in 25 µm intervals, and the final class extends to 200 µm.

4.2.2 Chemical Composition

The Optima 7300 V from PerkinElmer Inc. is used for Inductively Coupled Plasma Optical Emission Spectroscopy (ICP-OES) to determine the chemical element composition according to ASTM E2371 [130]. This technique simultaneously quantifies elements in a sample, such as aluminium and magnesium. In this method, a plasma source excites the atoms and ions in the sample to emit light at a characteristic wavelength, which allows for element identification. The concentration of each element is determined by the intensity of the emitted light (amplitude).

Carrier gas hot extraction is used to measure the oxygen content in the powder, with the measurements conducted using a LECO TCH 600CR. When the sample is melted in a hot graphite crucible, gases are released. These gases are transferred to sensors via the carrier gas flow, where the oxygen content is then recorded. This procedure follows the guidelines of ISO 22963. [131–133]

For Ti-6Al-4V, the oxygen and nitrogen are measured using Inert Gas Fusion according to ASTM E1409 [133]. The hydrogen is determined with Inert Gas Fusion with detection using thermal conductivity (IGF-TC) according to ASTM E1447 [134]. The carbon is determined by combustion analysis (CA) according to ASTM E1941 [135].

4.2.3 Scanning Electron Microscope

The morphology of the AlMg11 powders is analysed using a scanning electron microscope (SEM), specifically the JSM-6490LV from JEOL Ltd. During this process, an electron beam excites the atoms in the sample, causing the emission of secondary electrons. These are detected by a secondary electron detector, allowing for detailed examinations of the powder morphology. [136]

4.3 Flowability

As a key aspect of processability, the influence of increased PSD on flowability is assessed. Flowability refers to the ease and consistency with which powder particles move under applied force. This characteristic is compared relatively between different PSDs and alloys, with deviations of 5 % or less in mean values considered as similar. Flowability is measured using both Hall funnel and rotating drum methods.

4.3.1 Flowability Measurement using the Hall Funnel

A schematic diagram of the Hall funnel is presented in Figure 4-5. This device is used to measure apparent and tapped density, and thus to calculate Hausner ratio and determine Hall flowability.

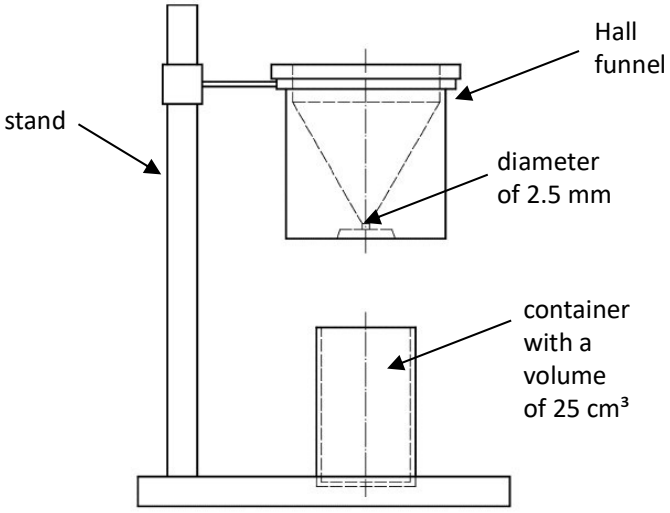

Figure 4-5: Schematic drawing of the Hall funnel setup, including the funnel and stand [137].

4.3.1.1 Apparent and Tapped Density and Hausner Ratio

The apparent and tapped densities of the powder are determined in accordance with DIN EN ISO 3923-1 and DIN EN ISO 3953. A sample of at least 100 cm³ is taken to allow for three separate measurements statistically required. The powder is poured through the Hall funnel (Figure 4-5) until the standardized container with a filling volume (*V*) of 25 cm³ overflows. The excess powder is then scraped off, and the remaining powder quantity is weighed to determine the apparent density using Equation (4.6). [138, 139]

$$\rho_a = \frac{m_a}{V} = \frac{m_a}{25} \quad (4.6)\ [138]$$

By compacting the powder with tapping and refilling the container with additional powder three times until it overflows, the excess powder is again scraped off. The tapped density is then determined after weighing, as described in Equation (4.7).

$$\rho_t = \frac{m_t}{V} = \frac{m_t}{25} \quad (4.7)\ [139]$$

The Hausner ratio, a key indicator for flowability, is calculated as the ratio of tapped to apparent density (Equation (4.8)). A Hausner ratio below 1.25 indicates a good flowability, suggesting high compactibility after powder recoating without the need for additional external compression, making it suitable for LPBF processing. [96, 140]

$$HR = \frac{\rho_t}{\rho_a} \quad (4.8)\ [140]$$

In Table 4-4, the Hausner ratio values are categorized into different flowability classes by Hausner:

Table 4-4: Flowability classification based on Hauser ratio [107, 140].

Hausner Ratio	Flowability Class
1.00-1.11	Excellent
1.12-1.18	Good
1.19-1.25	Fair
1.26-1.34	Passable
1.35-1.45	Poor
1.46-1.59	Very poor
> 1.60	non-flowable

Apparent and tapped densities, along with Hall flowability, are measured by Xue et al. and Xiongfei et al. for Ti-6Al-4V powders with different PSDs as shown in Table 4-5 [7, 50]. These values serve as reference points for the investigated Ti-6Al-4V powders. For AlMg11, no reference data could be identified.

Table 4-5: Flowability reference values for apparent and tapped density and Hall flowability for Ti-6Al-4V based on literature [7, 26, 50].

PSD in [µm]	Apparent Density in [g/cm³]	Tapped Density in [g/cm³]	Hausner Ratio [-]	Hall Flowability in [s/50g]	Reference
15-53	2.3	2.84	1.24	34.29	[50]
28-48	2.42	2.90	1.20	/	[26]
15-105	2.41	2.92	1.21	24.30	[50]
45-150	2.58	/	/	24.3	[7]

4.3.1.2 Hall Flowability

The Hall flowability test is conducted according to DIN EN ISO 4490 using the standardized Hall funnel (Figure 4-5). A sample of 50 g ± 0.1 g powder is poured into the Hall funnel while the outlet is manually kept closed. The outlet is then opened, and the time taken for the 50 g of powder to flow through the funnel is recorded. If powder clogging occurs, a single tap on the funnel is permitted. The Hall flowability is expressed in seconds per 50 g (s/50 g). A shorter Hall flowability time indicates easier movement of the particles by gravity, which is advantageous for achieving uniform powder application in LPBF. [137]

4.3.2 Flowability Measurement using the Rotating Drum

The GranuDrum from Granutools™ is a 100 ml glass-walled drum that is partially filled with 50 ml of powder, as illustrated in Figure 4-6. The drum is backlit, allowing a front-facing camera to capture the contour of the powder during rotation. The flowability of the powder is dynamically measured under varying stress conditions, which are induced by different rotational speeds in accordance with ISO/ASTM TR 52952 [141]. This approach allows for a more detailed analysis of the flowability, closely

mirroring the powder's behaviour during application and enabling the identification of time-dependent and stress-induced thickening mechanisms.

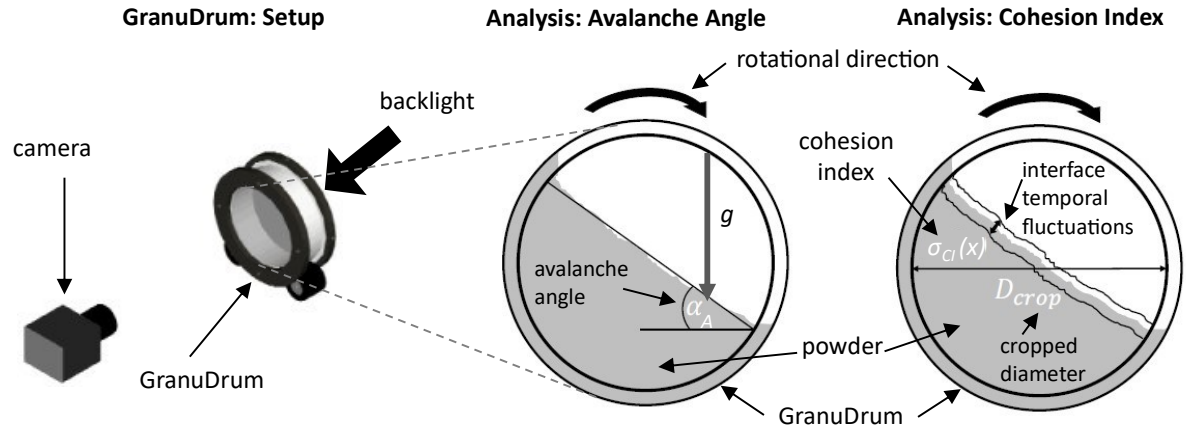

Figure 4-6: Schematic drawing of the GranuDrum setup and a sectional view of the drum with the measured variables [142].

The measurement method employed in this work is referred to as Speed Hysteresis. This method involves a sequence of increasing and then decreasing rotational speeds: 2, 4, 6, 8, 10, 15, 25, 35, 45, and 55 rpm. The sequence is designed to cover a range of stress levels. At each speed, 20 individual measurements are taken, and the mean values for each rotational speed are calculated. These mean values are presented as data points in the diagrams within this thesis, and the relationship between these points is represented by a linear trend line. Measurements where the powder is agitated (tossed) are excluded, as flowability is not reliably detectable under these conditions. Since the results for decreasing speeds do not differ significantly from those for increasing speeds, only the data for ascending rotational speeds are displayed.

The avalanche angle α_A is measured, representing the highest gradient before the powder slips in an avalanche-like manner. Additionally, the cohesion index is calculated, which is the normalized standard deviation of surface fluctuations. This index describes the smoothness of the powder surface, independent of the avalanche angle. The calculations are given in Equation (4.9) and Equation (4.10). [142, 143]

$$\sigma_{CI}(x) = \sqrt{\frac{\sum_{i=1}^{N_y(x)} (\bar{y}(x) - y_i(x))^2}{N_y(x)}} \quad (4.9)\ [142]$$

$$C = \frac{1}{D_{crop}} \int \sigma(x)\, dx \quad (4.10)\ [142]$$

In Table 4-6, the flowability is classified based on the avalanche angle and cohesion index. An avalanche angle of less than 45° and a cohesion index below 30 are classified as indicating passable processability [71, 144].

Table 4-6: Classification of flowability based on avalanche angle and cohesion index [71, 144].

Avalanche Angle in [°]	**Cohesion Index** [-]	**Flowability Class**
<30	0-5	Excellent
31-35	5-10	Good
36-40	11-20	Fair
41-45	21-30	Passable
46-55	31-40	Poor
56-65	41-50	Very poor
>65	51-60	non-flowable

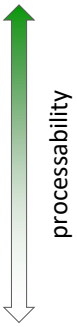

4.4 LPBF Process

In the following sections, the procedure for analysing the processability with increased PSD is described. This includes the machines used, the process parameter development, and a powder application test.

4.4.1 M290 EOS

The build jobs with AlMg11 powders are conducted on an EOS M290 system from EOS Electro Optical Systems, equipped with a 400 W Ytterbium-fibre laser with a fixed 105 µm laser beam diameter. The building chamber dimensions are 250 mm x 250 mm x 350 mm (length x width x height). A double-lip rubber coater blade is used as the recoating element. The processing chamber is flooded with 99.996 % argon as an inert gas, and no pre-platform heating is applied. The build jobs are performed with a layer thickness of 50 µm, in accordance with the AlMg11-material data sheet. The scan strategy for the EOS M290 print jobs is continuous, bidirectional and involves a 67° rotating exposure to minimize anisotropy. [30, 145] The samples are removed by wire cutting.

4.4.2 M2 Concept Laser

The Ti-6Al-4V build jobs are conducted on an M2 Cusing system from Concept Laser to avoid cross contamination. One of the two equipped Ytterbium-400 W lasers is used, ensuring comparability with the AlMg11-tests and eliminating additional influences on the specimen characteristics. The laser beam is set to a 100 µm diameter to match the conditions used in the AlMg11 experiments. The processing chamber is filled with 99.996 % argon as an inert gas, and no pre-platform heating is applied. A double lip rubber coater blade is used as a recoating element. The building chamber dimensions are 250 mm x 250 mm x 250 mm (length x width x height). All build jobs are performed with a layer thickness of 60 µm, which is typical for productivity oriented Ti-6Al-4V print jobs [50, 59]. The scan strategy follows a continuous, bidirectional, 90° rotating exposure, which is the closest setting on the M2 Cusing machine to the 67° rotation used on the EOS M290 machine.

To relief internal stresses, all Ti-6Al-4V specimens undergo heat treatment at 800 °C for 2 hours in a vacuum furnace, followed by furnace cooling. After heat treatment, the specimens are removed by wire cutting.

4.4.3 Process Parameter Development

The process parameters are developed with the aim of reaching relative densities higher than 99.5 % for AlMg11 and 99.9 % for Ti-6Al-4V according to their respective data sheets [9, 10]. To determine the relative density, density cubes (10×10×10 mm³) are printed with varying process parameters with a pyramid cone connection, as illustrated in Figure 4-7. This allows the cubes to be built without a support structure and therefore easier to detach from the building platform. The cubes serve as specimens for relative density, hardness and microstructure measurements, as described in the following sections. [30]

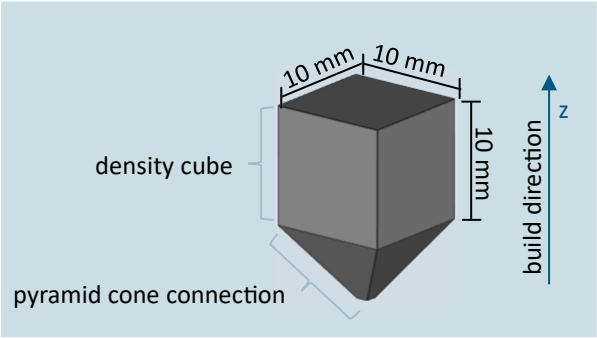

Figure 4-7: Rendered CAD image of a density cube with a pyramid cone connection.

In Figure 4-8, the positions of the infill and contour vectors are displayed schematically as a dependency of the CAD contour. The development of the process parameters concentrates on the infill-parameter. A variation of the contour parameter is deliberately omitted to avoid influences on the mechanical properties due to surface roughness in the tensile test specimens.

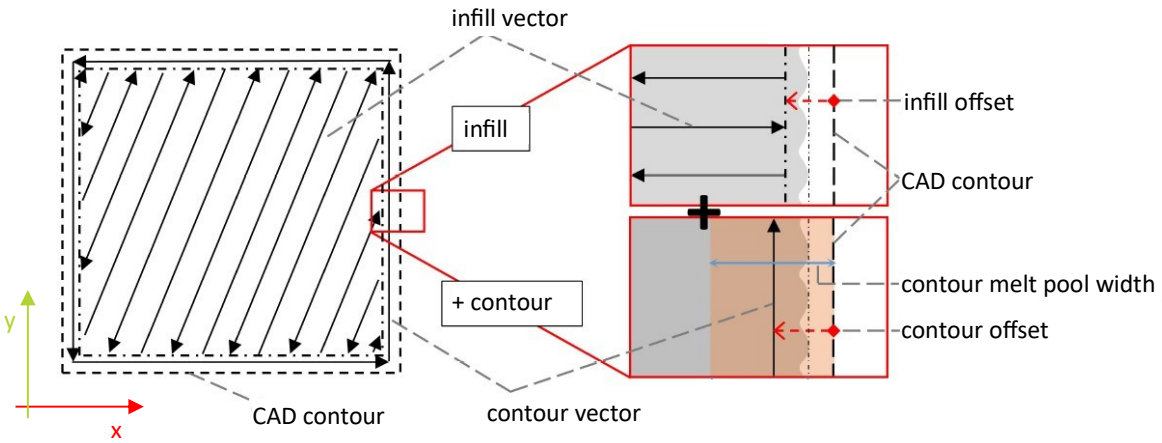

Figure 4-8: Schematic drawing of the contour and infill scanning vectors as originally published in [146]. Based on the CAD contour, the offset of the infill and contour vectors are indicated.

The process parameter development includes variations of the laser power P_L, the scanning speed v_S and the hatch distance Δy_S. The three process parameters are visualized in Figure 4-9. In addition, the fixed layer thickness LT is indicated

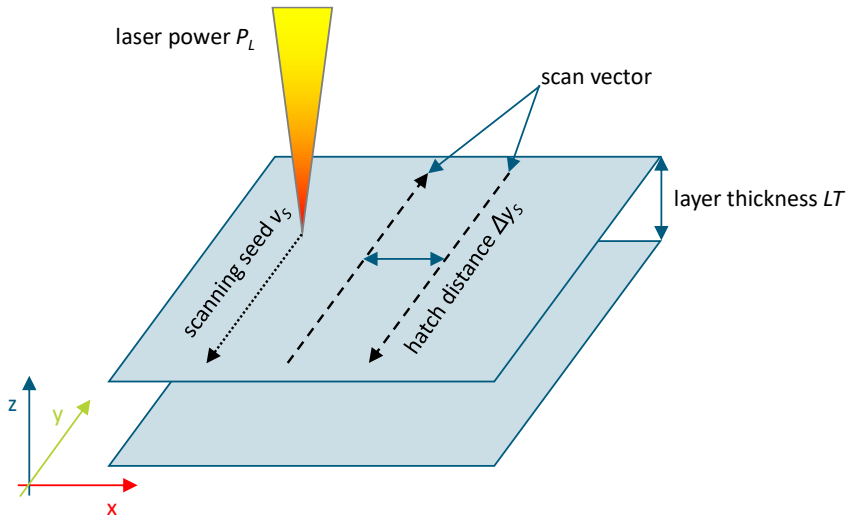

Figure 4-9: Schematic drawing of the process parameters laser power, scanning speed, hatch distance and layer thickness as originally published in [147].

The varied parameters are summarized in the key figure volumetric energy density (VED) in J/mm³ as shown in Equation (4.11) and the build rate (*br*) as shown in Equation (4.12):

$$VED = \frac{P_L}{v_S * LT * \Delta y_S} \quad (4.11)\ [148]$$

$$br = v_S * LT * \Delta y_S \quad (4.12)\ [148]$$

4.4.3.1 AlMg11

To determine the highest atomization yield that is processable in LPBF for the alloy AlMg11, density cubes are produced from each PSD. Processability is confirmed when a generic defect-free build up is achieved, with a target relative density of 99.5 %, in line with the data sheet specifications. [9]

For each PSD, a build-job with 36 density cubes is built, as schematically shown in Figure 4-10. The Ytterbium fibre laser in the EOS M290 has a maximum power of 400 W, with an effective usable power of 370 W, which is therefore used as the maximum in these studies. A process parameter with a VED of 62.9 J/mm³, developed in previous studies, serves as reference. This reference process parameter is applied to the density cubes located at the corners and centre, as highlighted in Figure 4-10. This setup allows for a direct comparison of the mechanical properties of the varied PSDs against the material properties specified in the data sheet for LPBF_20-70 powder.

For the remaining density cubes, the scanning speed is varied to account for both increases and decreases in VED, enabling the analysis of how the varied PSDs influence processability. The scanning speed is adjusted from 805 mm/s to 1405 mm/s in 20 mm/s increments and is assigned to the corresponding density cubes as illustrated in Figure 4-10. This approach ensures both a detailed mapping of the scanning speed's influence and a broad variation in VED around the reference process parameter. Rotating the density cubes by -15° around the y-axis reduces the initial point of contact between the recoater and each density cube, thereby minimizing the risk of detachment caused by the initial impact.

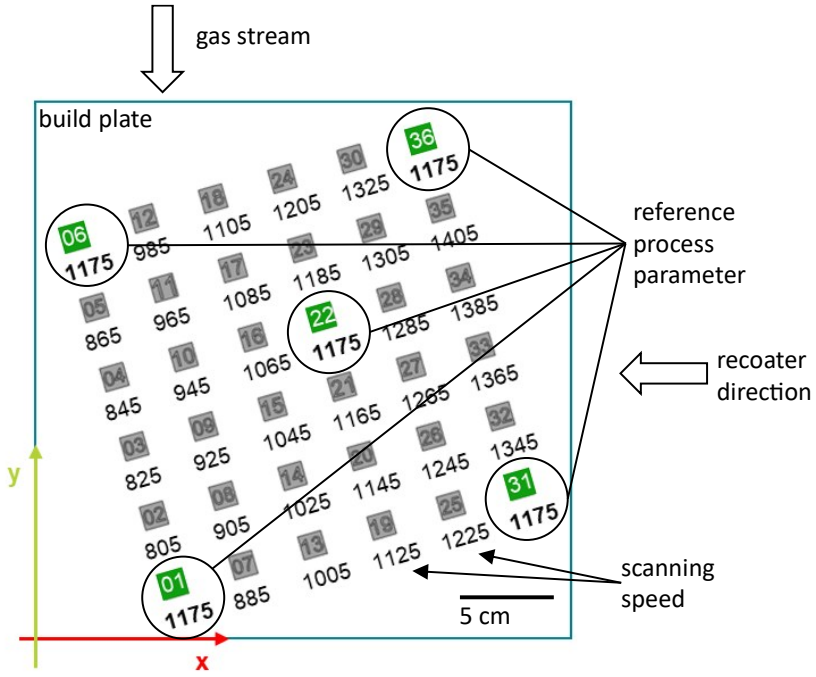

Figure 4-10: Schematic drawing of the build plate with the density cube placement with the scanning speed indicated.

The PSDs utilized for printing mechanical test specimens are selected based on their processability and the highest atomization yield among the investigated PSDs. To facilitate an accurate analysis of the influence of increased PSDs on manufacturability, all specimens are manufactured using the identical reference process parameters.

4.4.3.2 Ti-6Al-4V

The second alloy Ti-6Al-4V is used to specifically investigate the manufacturability of the adapted PSDs. Mechanical specimens are produced with process parameters adapted to each PSDs. This approach aims to determine whether adjustments to the process parameters for each PSD achieve manufacturability that meets industry reference values, as outlined in Table 3-4, in addition to ensuring processability.

The process parameters laser power P_L, scanning speed v_S and the hatch distance Δy_S are adapted for each PSD based on the criterion of high relative density, specifically above 99.9 %. These process parameter variations are performed using a fractional factorial design of experiments (DOE). In each build job, 36 cubes are placed on the build platform of an M2 Cusing from Concept Laser, similar to Figure 4-10. The standard process parameter from a comparable LPBF machine is initially applied to the LPBF_20-53 powder for the first stage of parameter development. For the larger EBM_45-106 powder, the approach involves increasing the VED compared to that used for LPBF_20-53, ensuring complete melting of the larger particles. The amount of VED increase is determined through experimental testing. The Ti64_20-100 powder, a blend of LPBF_20-53 and EBM_45-106 powders, combines small (20 µm) and large (100 µm) particles resulting in a wide distribution (span of 80 µm). It is assumed that the VED of the final Ti64_20-100 process parameter will fall within the VED range established for the other two powders.

In the final print jobs for each PSD, density cubes and tensile specimens are manufactured using the identified, adapted processes parameters. This allows for the determination of mechanical properties and as assessment of the manufacturability of parts meeting the specified industry standards.

4.4.4 Powder Application Analysis

A powder application analysis is conducted to determine the particle sizes applied on the build plate. Powder samples are collected from the supply, the build chamber, and the overflow as indicated in Figure 4-11. The PSD is measured using dynamic image analysis as described in Subsection 4.2.1. The PSDs of the samples are then compared to those of the initial supply and the set layer thickness. The differences in D10, D50, and D90 values are presented in a bar chart, with the layer thickness indicated by a red bar.

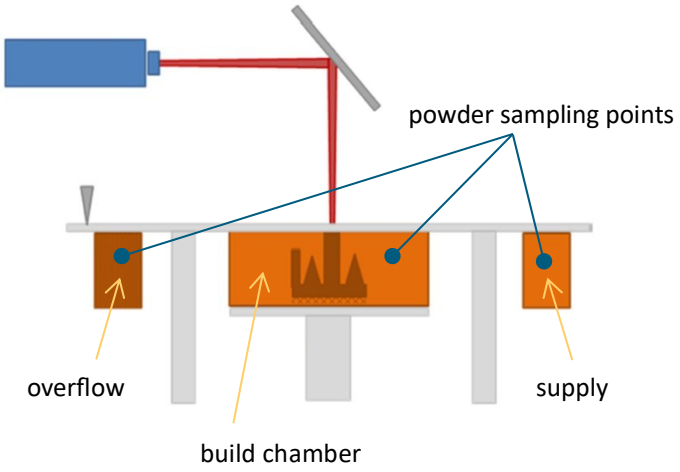

Figure 4-11: Schematic drawing of the LPBF machine setup, with indication of powder sampling points in the supply, build chamber and overflow.

4.5 Mechanical Properties

The mechanical properties evaluated in this thesis include relative density, microstructure, hardness, and tensile properties. The corresponding testing methods are described in the following sections.

4.5.1 Relative Density

The relative density of the printed cubes is measured after preparation. The cubes are warm-embedded in a polymer matrix (ClaroFast) using the CitroPress from Struers. The embedded specimens are then ground and polished. For polishing, a 0.04 µm oxide polishing solution (OP-S) suspension is used for the AlMg11 samples, while a 0.04 µm OP-U suspension is applied to the Ti-6Al-4V samples. Each material is processed using a specific program that adjust grinding roughness, duration, pressure and grinding direction according to the material requirements.

Images of the polished samples are captured using a VHX-5000 reflected-light microscope from Keyence, with 50x magnification in dark-field exposure. Each micrograph of a cube is composed of several individual images stitched together. The relative density is calculated using the image processing software provided by Keyence, as described in Section 4.1.3.

4.5.2 Microstructure

An exemplary examination of the microstructure is conducted to identify general differences in the build-up of the various PSDs. The embedded and polished specimens used in the relative density analysis are also utilized for microstructure analysis. High-resolution microscopy is performed using a JEOL 7200 F Scanning electron microscope (SEM), with backscattered electron (BSE) images to capture detailed microstructural features. For the Ti-6Al-4V specimens, conductivity is achieved by connecting them to the socket using a copper band.

4.5.3 Hardness

The hardness is measured on the polished surface of the density cubes using a DuraScan from Struers according to DIN 6507-1. The Vickers hardness HV10 is measured with a 4-sided diamond pyramid featuring a square base and an angle of 136°, applying a load of 10 kgf (98 N). For statistical validation, the measurement is repeated at five points per cube, as illustrated in Figure 4-12 and the arithmetic mean is calculated.

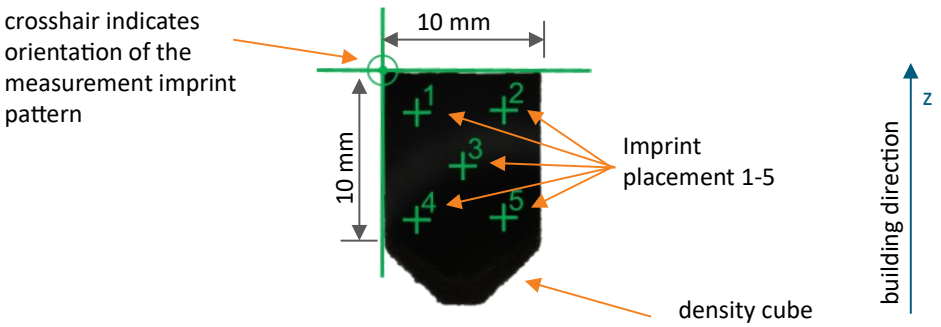

Figure 4-12: Schematic drawing of a longitudinal section of a density cube, with indication of the 5-point imprint pattern.

4.5.4 Tensile Properties

To determine the static mechanical properties, tensile specimens are manufactured in form B according to the standard DIN 50125. The detailed geometric dimensions for specimens with the diameters d_0 = 4 and 5 mm are specified in DIN 50125 [149]. The specimens are printed with an offset of 1 mm and finish machined to conform to form B specifications to exclude potential notch effects due to varying surface roughness. Five specimens are tested for each orientation. The orientation of 0° refers to a horizontal position relative to the polar angles, while 90° refers to a vertical position on the building platform, according to DIN 52921, as shown in Figure 4-13 [150].

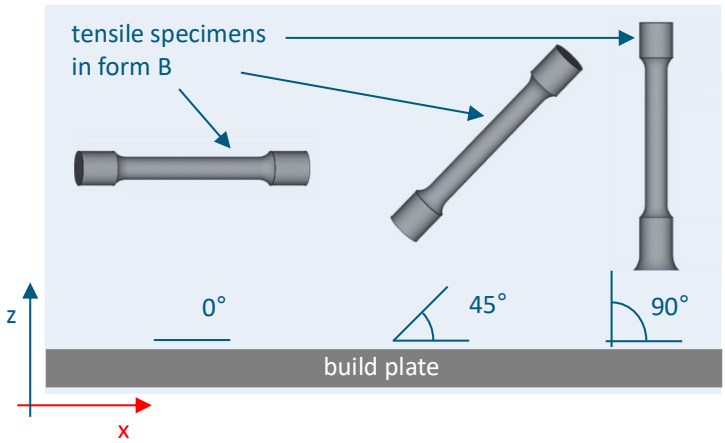

Figure 4-13: Schematic drawing of rendered CADs of tensile specimens with assigned orientations according to DIN 52921 [150].

Tensile testing is performed by external accredited laboratories in accordance with DIN EN ISO 6892-1 at 20 °C. The testing machine used is a Galdabini – Quasar with a capacity of 600 kN/50 kN. The properties determined include yield strength at 0.2 % offset ($R_{p0.2}$), tensile strength (R_m), and elongation after fracture (A). [149–151]

4.5.5 Correlation Analysis

The correlation analysis is conducted using the statistical software *R*, applying Pearson's correlation coefficient (r_C) to assess linear relationships between two variables. The Pearson correlation coefficient is calculated using Equation (4.13). It is scaled between −1 and +1 for each variable. A value of −1 indicates a perfect inverse correlation, +1 represents a perfect direct correlation, and a value of 0 implies no correlation. The Pearson correlation coefficient is considered to indicate a strong correlation if it exceeds ±0.7. This threshold is typically regarded in literature as indicative of a high correlation, thus ensuring substantial statistical relevance. [108]

$$r_c = \frac{\sum_{i=1}^{n}(x_i - \bar{x})(y_i - \bar{y})}{\sum_{i=1}^{n}(x_i - \bar{x})^2(y_i - \bar{y})^2} \qquad (4.13)\ [152]$$

x_i, y_i = values of the two variables x and y

$\bar{x}, \bar{y}$ = mean values of the two variables x and y

n = sample size

To determine if the observed correlation is likely to be a genuine trend rather than a random occurrence, the correlation coefficient is compared to a significance level (α_C), typically set above 5 %. This implies a 95 % probability that the observed correlation reflects a true relationship rather than occurring by chance. [153–155]

The results are presented in a correlation matrix, where positive correlations are indicated in blue and negative correlations in red. The size of the circles in the matrix represents the significance of the correlation: larger circles denote higher significance. The causal relationship is analysed for each validated correlation. [153]

4.6 Resources and Costs

The impact of implementing larger powders, such as EBM powder with a PSD of 45-106 µm, on potential resource and cost savings is assessed.

To estimate resource savings, atomization yields from the literature are reviewed. Based on these studies, the yield from the LPBF reference PSD is compared with the previously identified largest PSD that exhibits processability and manufacturability in LPBF. This comparison is used to assess the potential increase in atomization yield. An increase of atomization yield corresponds to resource savings, as higher atomization efficiency reduces raw material waste and enables more effective resource utilization during production. However, the exact determination of these resource savings is not possible due to the proprietary nature of the data held by powder atomizers.

To estimate the cost reduction potential by utilizing larger particles, a market survey is performed. Offers from 22 powder suppliers, including both traders and manufacturers, are requested for Ti-6Al-4V ELI grade 23 in quantities of 100 kg and 1,000 kg, covering both EBM and LPBF PSDs. Machine suppliers are not considered. For LPBF, the prices are summarized for typical LPBF PSDs ranging from 20-53 and 20-63 µm. For EBM, prices are summarized for PSDs of 44-106 µm, 45-100 µm and 45-125 µm. Prices are not negotiated, and all offers are received between June 1st to August 31st, 2021. Currency conversions are performed on September 2nd, 2021, to align the prices. Four suppliers are declared as outliers, leaving a database of eleven suppliers for analysis. It is noted that suppliers offer fixed PSDs, so a direct comparison of identical PSDs is not possible.

5 Generation of varied PSDs for LPBF

The foundation of investigating the influence of varied PSD on processability and manufacturability, is the generation of homogeneous, blended PSDs. In the following sections, the suitability of the self-developed V-Blenders is assessed. After successful validation, PSD variations are generated and characterized to identify any deviations. These deviations are then linked to variations in processability and manufacturability in the subsequent investigations.

5.1 Validation of Blending Methodology

To generate variations in PSD using the self-manufactured V-blender, a series of preliminary validation steps is performed to ensure a homogeneous blending result. These steps are outlined as follows:

- Step 1: Validation of particle marking methodology
- Step 2: Determination of blending settings
- Step 3: Assessment of powder degradation

If all three steps are validated successfully, the V-blender is approved for use in generating the PSD variations required for subsequent experiments.

5.1.1 Step 1: Validation of Particle Marking Methodology

In the following sections, the results of the validation of the particle marking methodology are presented and discussed.

5.1.1.1 Results of the Validation of Particle Marking Methodology

The particle marking methodology is validated to ensure it does not influence the blending outcome by confirming the similarity of the marked powder to the original powder, in terms of:

- particle size distribution
- flowability

To verify this, Ti-6Al-4V powder is divided into two batches: one original and one marked through thermal oxidation, as detailed in Subsection 4.1.2. To rule out any influence of the oxide layer from the marking process on particle size, the frequency distribution of the original and marked powder is compared in Figure 5-1. Both powders exhibit similar monomodal curves, with a local maximum around 30 µm and inflection points around 20 and 50 µm. No influence of the particle marking on the particle size is observed.

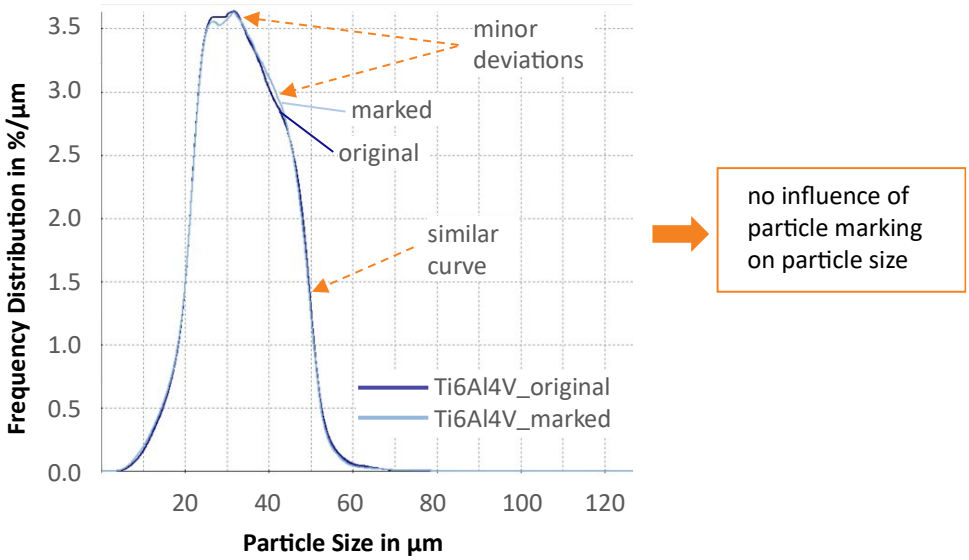

Figure 5-1: Diagram of the frequency distribution comparing original and marked Ti-6Al-4V powders.

The primary requirement for the marked powder is that its blending behaviour closely resembles that of the original powder. This similarity ensures the validation of the blending process operation with marked and original particles to reliably transfer to blends of original and unmarked powders. Flowability functions as an indicator of the particle movement while blending. That is why, the flowability of both the original and marked powders is measured, and the results are demonstrated in Table 5-1.

Table 5-1: Overview of apparent and tapped density, Hausner ratio Hall flowability of original and marked Ti-6Al-4V Powders.

Powder	**Apparent Density** in [g/cm³]	**Tapped Density** in [g/cm³]	**Hausner ratio** [-]	**Hall flowability** in [s/50g]
original	2.46 ± 0.01	2.83 ± 0.01	1.15	23.1 ± 0.1
marked	2.45 ± 0.00 ✓	2.80 ± 0.01 ✓	1.14 ✓	24.3 ± 0.3 ↑ +5.2 %

The results for apparent and tapped density are comparable, with deviations of up to 0.03 g/cm³. The resulting Hausner ratio is also similar. However, the Hall flowability of the marked powder is 1.2 s/50g higher than that of the original powder. This difference corresponds to a 5.2 % increase, which is slightly above the accepted 5 % deviation threshold.

5.1.1.2 Discussion of the Validation of Particle Marking Methodology

Validating particle blending presents challenges that require careful attention to both particle characteristics and validation methodologies. The characteristic chosen for tracking, such as alloy composition, shape, size, and colour, directly affects the choice of appropriate validation techniques.

This thesis does not account for variations in the chemical composition of particles during the blending process. As noted by Dietrich et al., the chemical composition significantly influences powder melting behaviour and the mechanical properties of printed parts [156]. Consequently, verifying blending results through chemical composition analysis is primarily suitable for initial operations and alloy pro-

duction. Achieving a high level of homogeneity is critical for processing powders, as differences in density impact powder flowability, which, in turn, affects the blending outcome when using different alloys. Methods like ICP-OES or with EDX are effective for evaluating compositional differences and serve as a useful validation technique for alloy production [157, 158].

Particle shape influences powder flowability and blending performance. In tendency, irregular particle shapes reduce blending homogeneity or increase the required blending time [71]. Distinct variations in particle shapes are observed between different atomization methods, while the same technology yields minimal differences [74]. Therefore, particle shape is a suitable criterion when blending powders produced through different atomization technologies. Differentiating between spherical and irregular shapes poses a challenge in image-based particle tracking, requiring advanced strategies. Qualitative assessments using SEM images, as described by Young et al., offer a practical approach [24].

Particle size affects flowability, with relatively smaller particles demonstrating stronger interparticle forces that potentially lead to agglomeration [71]. Despite these challenges, particle size is advantageous due to its ease of measurement using methods as dynamic image analysis, allowing for statistically robust assessments. Dynamic image analysis reveals if a distribution is homogeneous, which is especially relevant when blending powders of varying sizes for specific applications. This method offers the added benefit of preserving the powder's suitability for processes like LPBF.

The particle colour does not differ between powders of the same alloy. That is why this criterion is not suitable for particle tracking without any treatment. Thermal oxidation enables effective particle differentiation of original greyish particles through the formation of colourful, nanometre-thin oxide layers on particle surfaces [123–125]. An advantage of the oxide layer is that it forms over the entire particle. For coatings, the powders need to be agitated for full coverage. The coating must exhibit a strong adhesion so that the layer is not rubbed off during the blending process. Irregularities that lead to a change in particle shape could occur.

Comparing the assessment criteria of particle size and colour, dynamic image analysis typically produces lower quality scores in contrast to area measurement, though it offers greater quantitative accuracy. Therefore, a combination of both methods is recommended to ensure robust validation of blending results. Moreover, alternative validation techniques, such as elemental composition analysis, should be considered, particularly in alloy production, to enhance the validation process and ensure the integrity of blended powders.

The influence of the added oxide layer on the flowability and blending behaviour is investigated. A minimal impact on particle size, shape, and flowability, measured as apparent and tapped density as well as the Hausner ratio and Hall flowability, is confirmed. This proves that the blending result is not affected by the oxide layer.

In conclusion: Thermal oxidation for particle marking shows no significant influence on particle size or frequency distribution. The flowability of the marked powder is generally comparable to that of the original powder, with only a slight decrease in Hall flowability. Therefore, the marked particles are suitable for particle tracking to validate the blending result.

5.1.2 Step 2: Determination of Blending Settings

In the following sections, the results of the determination of the blending settings are presented and discussed.

5.1.2.1 Results of the Determination of Blending Settings

The blending settings for achieving a homogeneous blend are determined by:

- Identifying the rotational speed for effective[12] blending.
- Identifying the required blending time to ensure homogeneity.

Three batches of 10 % marked powder and 90 % original powder are blended at three rotational speeds of 20, 40, and 60 rpm. Samples are taken over time as described in Subsection 4.1.4. The target is to achieve a homogeneous distribution with 10 % marked particles. The results are demonstrated in Figure 5-2.

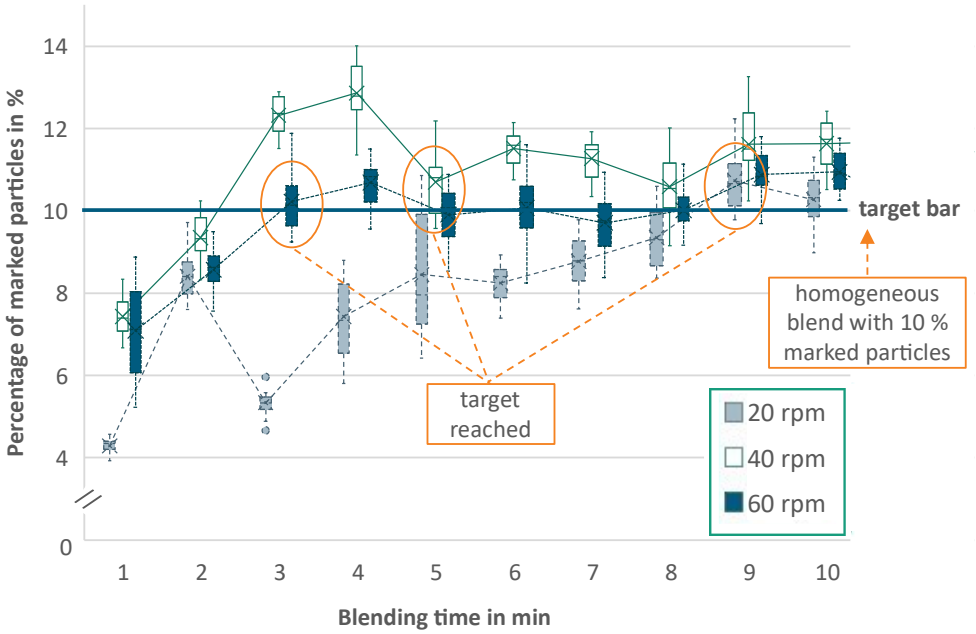

Figure 5-2: Diagram of the percentage of marked particles over 10 minutes at rotational speed of 20, 40 and 60 rpm.

An increase in the concentration of marked particles is detected over time for all three rotational speeds. At 20 rpm, it takes the longest time, 9 minutes, to reach the target of 10 % marked particles. At 60 rpm, the target is achieved after 3 minutes and remains consistent with further blending. At 40 rpm, the target is reached after 5 minutes.

Light microscopy images are presented from samples blended for 1, 5 and 10 minutes at 20 rpm in Figure 5-3. These images qualitatively assess the homogeneity of the marked particle distribution within the original powder. After 1 minute of blending, single marked particles are observed, which are homogeneously distributed. By 5 minutes, clusters of marked particles begin to appear. After 10 minutes, the target of 10 % homogeneous, randomly distributed marked particles is achieved, validating the quantitative results obtained from the optical image analysis shown in Figure 5-3.

[12] Effective: The shortest blending time needed to achieve a homogeneous blend with minimal impact on particles.

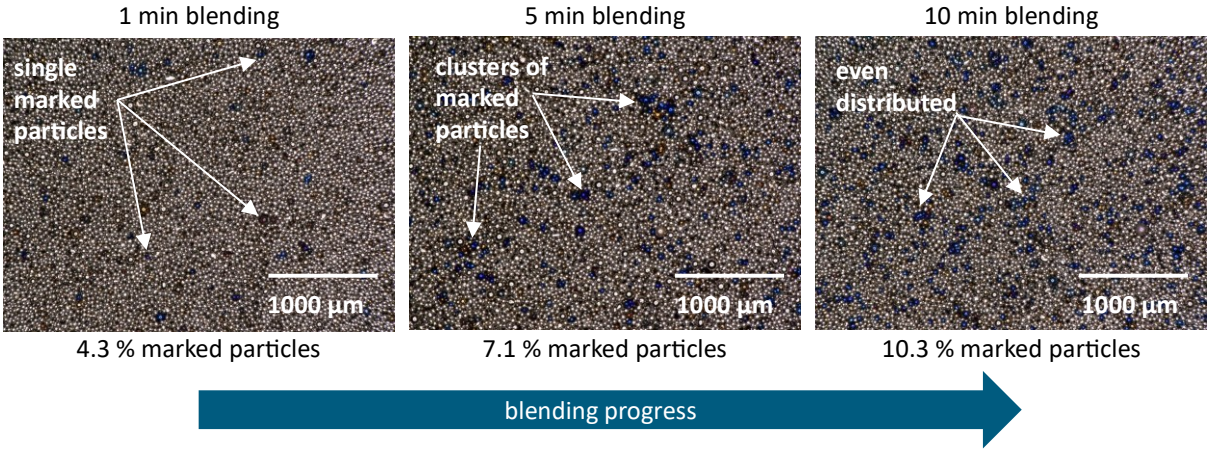

Figure 5-3: Light microscopy images of blended powder with marked and non-marked particles after 1, 5 and 10 minutes of blending at 20 rpm.

5.1.2.2 Discussion of Determination of Blending Settings

In the analysis of the microscope images, it is observed that 1-2 % more area tends to be counted than what is marked. This discrepancy is primarily caused by light reflections on the spherical particle shape and their shiny surfaces, as well as increased radiation at the image edges due to the angle of light incidence. Since this effect is consistent across all images, the full image is used for evaluation. An alternative approach is the analysis of the image core, which would yield more accurate results for that section but reduce the sample size and provide less qualitative information about the overall blend. The larger image section represents a compromise. A qualitative review of the images by the analyst argues in favour of the use of the full image, acknowledging a consistent exaggeration of the results that still reflects the overall trend.

The image analysis of the blending results with marked particles is feasible using an optical microscope. The primary limitation is the small sample size on the double metal plate that is analysed. To address this, multiple samples (in this case eight) are taken and measured, significantly increasing the evaluation effort. Additionally, the formation of an oxide layer makes the powder unsuitable for further use in LPBF, due to the increased risk of brittleness caused by elevated oxygen levels, as reported by Meier et al. [70]. The oxygen content is likely to exceed the Ti-6Al-4V standards, potentially reducing strength and ductility [41, 70, 159–161]. While particle marking is suitable for an initial validation of blending, it is not a viable method for long-term operation. In situ methods using high-speed cameras and synchrotron X-ray imaging, such as those developed by Priyadarshi et al. and Kohlwes et al., provide the advantage of particle tracking without the need for marking [162, 163]. These methods are more appropriate for powders intended for LPBF processing, though they are limited by restricted powder accessibility during the blending process.

The blending results are discussed in terms of blending time and percentage of marked particles and their homogeneous distribution. The desired blending degree is achieved in less than 10 minutes, particularly at higher rotational speeds of 40 and 60 rpm. Initially, the two powders (marked and original) are completely separated. As blending progresses, clusters of marked particles dispersed among the original particles, as illustrated in Figure 5-3 after 5 minutes. After 10 minutes of blending at 20 rpm, the mechanisms of convection and dispersion result in a homogeneous, random particle distribution,

also depicted in Figure 5-3. Paul et al. state that the degree of blending is determined by powder volume and the number of rotations, which is confirmed by shorter blending times at higher rotational speeds [111].

In conclusion: All three rotational speeds achieve a homogeneous blending result within 10 minutes, as confirmed through both qualitatively and quantitively analyses. The final selection of blending settings is based on their impact on particle quality, i.e., whether degradation occurs.

5.1.3 Step 3: Assessment of Powder Degradation

In the following sections, the results of the assessment of the powder degradation are presented and discussed.

5.1.3.1 Results of Assessment of Powder Degradation

Within this assessment, the impact of blending on particle of powder quality is evaluated. Therefore, the particles are examined for:

- Alterations in particle shape
- Alterations in particle size

The blending impact aims to be gentle enough to prevent degradation of particle characteristics. To test for degradation, the particle size and shape are measured over 180 minutes of blending at 20, 40 and 60 rpm as described in Section 4.1.5. The results, presented in Table 5-2, feature a standard deviation of 0.000 within the three measurements per sample.

Table 5-2: Particle shape comparison after 180 minutes at 20; 40 and 60 rpm.

shape	target	20 rpm		40 rpm		60 rpm	
		result	Δ in %*	result	Δ in %*	result	Δ in %*
Ø *SPHT*	**0.879**	0.875	-0.45	0.877	-0.23	0.877	-0.23
Ø *Symm*	**0.930**	0.927	-0.32	0.931	+0.11	0.929	-0.11
Ø w_P/l_P	**0.864**	0.859	-0.58	0.866	+0.23	0.863	-0.16

* >5 % deviation classifies as significant

The measured values are compared to the calculated target for a 90:10 ratio of original and marked powder. The target sphericity, symmetry, and aspect ratio are achieved at all rotational speeds. The deviations range between 0.11 % for the symmetry at 40 and 60 rpm to 0.58 % for the aspect ratio at 20 rpm. Overall, no significant shape degradation is observed after 180 minutes of blending.

The calculated target size values and the measured particle sizes are presented in Table 5-3. All target values for D10, D50 and D90 are met at all three rotational speeds. The highest deviation is observed for D10 at 20 rpm with a difference of 4.07 %. Across all three rotational speeds, a slight decrease in D10 values and a slight decrease in D90 values are observed, while no clear trend is detectable for D50.

Table 5-3: Overview of target and measured D10, D50 and D90 values after 180 minutes blending at 20; 40 and 60 rpm.

Deciles	target in [µm]	20 rpm		40 rpm		60 rpm	
		result in [µm]	Δ in %*	result in [µm]	Δ in %*	result in [µm]	Δ in %*
Ø D10	**36.13**	37.6 ± 0.7	+4.07	36.4 ± 0.9	+0.75	37.1 ± 0.8	+2.68
Ø D50	**55.43**	56.9 ± 1.1	+2.65	54.8 ± 0.7	-1.14	55.2 ± 1.0 ✓	-0.41
Ø D90	**110.42**	108.4 ± 0.7	-1.83	106.5 ± 0.6	-3.55	106.9 ± 0.9	-3.19

* >5 % deviation classifies as significant

The results for all three rotational speeds are similar, with 40 rpm providing the best balance between effective blending, achieving homogeneity after 5 minutes, and minimizing the impact on particle quality. Therefore, 40 rpm with a blending time of 10 minutes is established as blending settings.

The results for samples taken over 180 minutes at 40 rpm, as presented in Figure 5-4, demonstrate whether the blend quality remains consistent over time. This analysis serves as the final validation for the blender's performance.

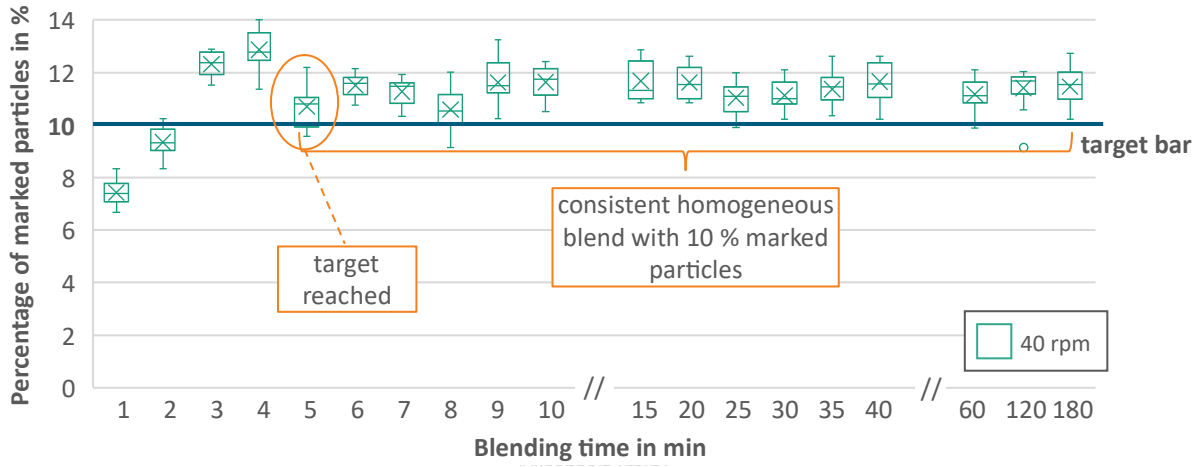

Figure 5-4: Box plot diagram showing the percentage of marked particles over 180 minutes at 40 rpm.

Once the target of 10 % marked particles is achieved after 5 minutes, the percentage remains steady between 10-11.5 %. This consistency indicates that once a homogeneous blend is reached, no significant segregation occurs while blending.

5.1.3.2 Discussion of Assessment of Powder Degradation

The powder degradation is assessed over a blending time of 180 minutes by sampling at multiple points (top of both legs and the bottom) within the V-blender to verify consistency throughout the powder. This multipoint sampling approach, based on DIN EN ISO 3954[13], confirmed homogeneous particle distribution aligning with the desired completely random state described by Daumann and Nirschl [109]. Negligible degradation is observed, supporting the integrity of the blend. While the particle shape remained consistent with unblended powders, a slight narrowing of the PSD is detected after 180 minutes.

[13] General powder sampling standard which is adapted to the powder blender through different sampling points.

The Ti-6Al-4V powder used for marking is a recycled powder from LPBF, resulting in a larger PSD (36-110 µm). The D10 values of approximately 36-37 µm and D90 values of around 106-108 µm are closely aligned with the target PSD intended to be generated using virgin LPBF_20-53 and EBM_45-106 powders. Smaller particles (<30 µm) adhered to the V-shaped container due to higher interparticle forces, leading to a 1 µm increase in the D10 value. Additionally, the D90 value decreased by an average of 3 µm, likely due to the agglomerate breakdown. Low standard deviations in particle size confirm the reliability of the results, consistent with findings from Tang et al. and Yusuf et al. on typical variations in PSD through powder handling [164, 165].

Extensive testing confirmed the blend's stability and suitability for further use, despite potential segregation risks inherent in the V-shaped design. The design tends to promote segregation of relatively large and small particles due to percolation and momentum effects. Percolation occurs through vibration and container movement, while momentum-induced segregation is more likely during emptying. [89, 111]

Overall, the blend quality is sufficient, though cost implications and operational efficiency must be considered. The common “quality-time-cost” trade off in product development applies here. A precise cost assessment for the V-blender is challenging, as initial development is the most time-consuming and unique aspect of the process. Comparing cumulative costs of single parts with commercially available blenders is not straightforward due to differing corporate structures, economies of scale, and profit margins. However, the potential cost savings from utilizing larger particle sizes such as EBM_45-106 need to be assessed to determine whether they outweigh the initial investment in a custom powder blender.

In conclusion: Despite minor deviations of less than 5 % in particle shape and particle size, the overall degradation in powder quality is negligible. As final blending settings, a rotational speed of 40 rpm for 10 minutes is selected.

5.1.4 Key Findings on Blending Methodology Validation

The successful validation of the blending methodology in three steps is summarized in Table 5-4. It is demonstrated that particle marking with thermal oxidation is possible without significant impairment of the particle characteristics. A validation of blending results is challenging. Two validation possibilities are used. A combination of light microscopy image processing with marked particles for initial operation and, in the case of PSD generation, an additional dynamic image analysis determining particle size and shape for operation to validate the blending result. This ensures accurate assessment of powder blending techniques, while also expanding validation capabilities across the entire powder handling process, including the design of handling components.

The investigations demonstrate the suitability of the self-developed V-blender in generating a homogeneous blend without significant degradation of particle quality. A rotational speed of 40 rpm for 10 minutes is selected as blending settings for PSD generation, providing a balance between minimal impact on the particles and efficient blending time. Based on this, the generation of PSD generation is enabled.

Table 5-4: Checklist of three-step blending validation criteria.

Step	Result	
Step 1: Validation of particle marking methodology	Thermal oxidation shows no significant influence on: • Particle size • Particle size distribution • Flowability: ▪ apparent, tapped density and Hausner ratio Minor reduction of Hall flowability detected	✓
Step 2: Determination of blending settings	A homogeneous blend is achieved with: • 20 rpm after 9 min, • 40 rpm after 5 min and • 60 rpm after 3 min. • Blend results remain consistent over 180 minutes Final blending settings: 40 rpm for 10 minutes	✓
Step 3: Assessment of powder degradation	No significant degradation for: • Particle size • Particle shape	✓

5.2 Determination of blended Powder Characteristics

With the successful validation of the V-blender, the desired powders are generated, as detailed in Section 4.1. To investigate the influence of PSD on processability and manufacturability, all powders are characterized to identify differences between them, allowing for the attribution of potential influencing factors. This characterization includes an analysis of:

- particle size,
- particle shape and
- chemical composition.

5.2.1 Particle Size and Particle Size Distribution Analysis

In the following sections, the results of the particle size and PSD analysis are presented and discussed, with the analysis first applied to AlMg11 and then to Ti-6Al-4V.

5.2.1.1 Results of AlMg11 Particle Size Analysis

The results for the PSD analysis of the AlMg11 powders, are summarized in Table 5-5. Target values for D10 and D90 are based on the specified size limits for each powder, as detailed in Section 4.2.1.

Table 5-5: D10, D50 and D90 and span targets and results for AlMg11 powders.

Powder	D10 in [µm]		D50 in [µm]		D90 in [µm]		Span in [µm]	
	target	result	target	result	target	result	target	result
LPBF_20-70	>20	29.8 ± 0.3	45	44.1 ± 0.3	<70	66.5 ± 0.4	50	↓ 36.7
OVS_70-170	>70	71.2 ± 2.2	120	↓ 108.4 ± 5.2	<170	170.7 ± 4.6	100	99.5
PSD1_20-45	>20	26.8 ± 0.0	32	34.8 ± 0.2	<45	↑ 47.3 ± 0.3	25	↓ 20.5
PSD2_45-70	>45	↓ 36.2 ± 0.2	57.5	↓ 53.7 ± 0.5	<70	↑ 71.9 ± 1.1	25	↑ 35.7
PSD3_70-125	>70	78.3 ± 1.3	97.5	↓ 107.8 ± 2.1	<125	↑ 147.5 ± 2.4	55	↑ 69.2
PSD4_20-100	>20	30.8 ± 0.4	60	↓ 53.0 ± 2.1	<100	101.7 ± 1.5	80	↓ 70.9
PSD5_20-125	>20	33.8 ± 0.8	72.5	↓ 67.4 ± 2.6	<125	123.4 ± 1.5	95	89.6
PSD6_20-170	>20	34.1 ± 1.2	95	↓ 74.2 ± 4.8	<170	166.1 ± 2.8	150	↓ 132.0

The LPBF_20-70 powder, which serves as a base for blending the other powders, remains within the acceptable limits, though its D10 value of 29.8 µm exceeds the target of 20 µm. The D10 values of all other powders meet their respective D10 target values, except for PSD2_45-70, where the D10 value is measured at 36.2 µm, which is 8.8 µm below the target size of 45 µm. The D90 value of PSD3_70-125 is notably high at 147.5 µm, exceeding the target by 22.5 µm. Despite this, the D90 values for most powders closely align with the expected upper particle size limits, based on the mesh sizes used during sieving. Additionally, the D50 of OVS_70-170 is 12 µm below the expected value, indicating a shift in the size distribution towards particles below 108 µm for this powder.

In Figure 5-5, the frequency distributions of the eight AlMg11 powders are demonstrated. The curves represent monomodal distributions, with each sample exhibiting a distinct particle size range and distribution shape.

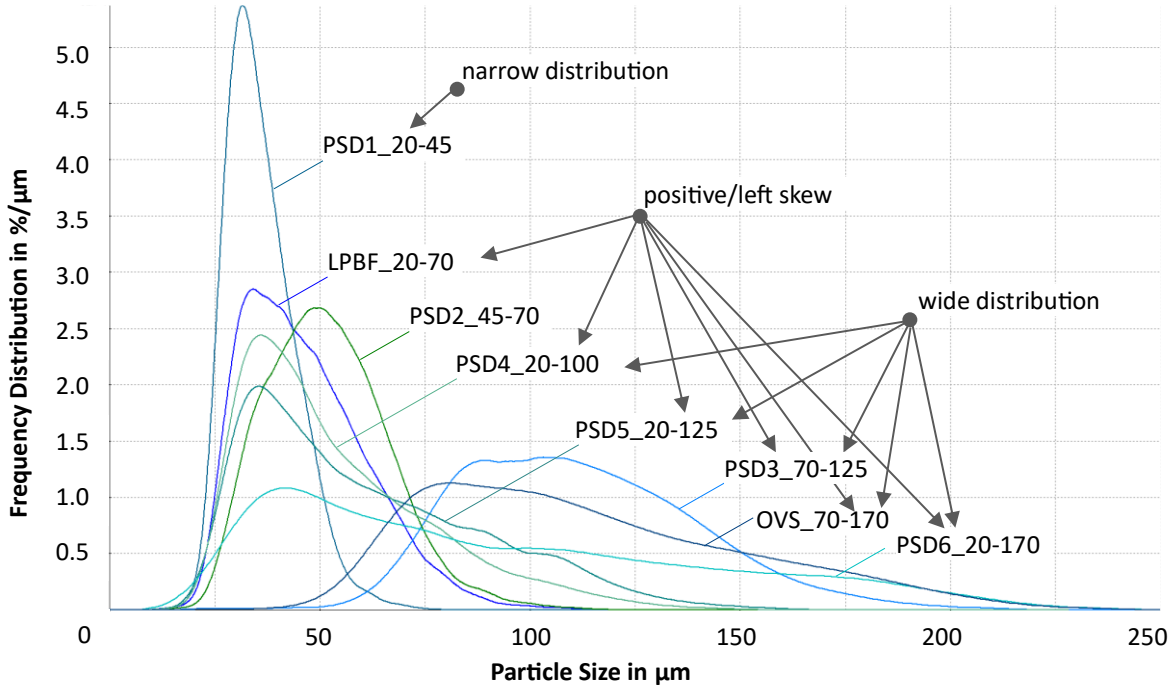

Figure 5-5: Diagram of the frequency distributions of investigated AlMg11 powders.

PSD1_20-45 shows a sharp peak with a steep rise and fall, indicating a narrow particle size range concentrated around 30 µm, with a smaller number (below 0.25 %/µm) of particles between 55-70 µm. LPBF_20-70, PSD2_45-70, PSD4_20-100 and PSD5_20-125 exhibit a positive skew, characterized by a steep increase in frequency distribution around 20-30 µm and a slower decline towards larger particle sizes (exact particle size is individual for each PSD). PSD3_70-125, PSD4_20-100, PSD5_20-125, PSD6_20-170, OVS_70-170 show broader, flatter peaks, indicating a wider and more even distribution of particle sizes, with spans above 70 µm.

5.2.1.2 Discussion of AlMg11 Particle Size Analysis

The particle size analysis proves that it is possible to generate desired PSDs using a V-blender and sieves. With 29.8 µm, the D10 value of the base powder LPBF_20-70 is 45 % higher than 20 µm, which leads to a coarsening of all generated powders including LPBF_20-70. This effect is enhanced by the typical loss of smaller particles, which is reported by Cordova et al. after eleven re-use cycles for Ti-6Al-4V with approximately 2 µm enlargement, and after six re-use cycles for AlSi10Mg approximately 8 µm increase [76]. The increase of D10 at 29.8 µm from LPBF_20-70 to D10 at 34.1 µm for PSD6_20-170 is likely due to the additional powder handing steps blending and sieving. This trend is more prone with increasing upper particle size limits, with PSD1_20-45 the smallest D10 at 26.8 µm and PSD6_20-170 the largest at 34.1 µm.

Compliance with the D90 values shows that the sieving process for the upper limit worked correctly. The exception for PSD3_70-125 leads to the conclusion that the sieving behaviour is affected without particles below 70 µm. Another reason for this is a higher irregularity of the particle sizes above 70 µm. Particles with a more elongated shape fit through the sieve on the shorter particle side. As the diameters are specified with their equivalent of a circle diameter with the same area, the overall larger area of these particles is considered in the size display. This assumption needs to be verified with the shape measurement in Subsection 5.1.2.2.

The absence of particles below 30 µm is reflected in the trend of smaller D50 values and narrower particle spans for most of the powders. Exceptions are PSD2_45-70 and PSD3_70-125, which fall outside their respective D10 and D90 limits, impacting their D50 and span results as well.

The diagrams of the frequency distribution highlight the trend towards smaller particles, with positively skewed curves. The monomodal distributions are expected due to the narrow gap of 4.7 µm between the D90 value (66.5 µm) of LPBF_20-70 and the D10 value (71.2 µm) of OVS_70-170 powder, both of which serve as base powders for PSD generation.

The D10, D50, and D90 values provide a baseline for future comparisons, reflecting the current PSDs of the AlMg11 powders. This baseline is essential for assessing changes in size distribution caused by subsequent processes such as blending, sieving, or material testing.

In conclusion: The generated AlMg11 powders are overall within their desired limits for D10 and D90. The absence of particles below 30 µm in LPBF_20-70 causes a shift towards smaller particles in the D50 and span values of the powders generated from LPBF_20-70. This is illustrated in the frequency distribution, which displays positive, left-skewed curves.

5.2.1.3 Results of Ti-6Al-4V Particle Size Analysis

In Table 5-6, the mean values for particle size of the Ti-6Al-4V powders are presented and compared with their specified limits. All D10 and D90 values fall within the acceptable range. However, the D90 values are significantly smaller, ranging from 11 % to 19.3 % below the specified limits. For instance, the Ti64_20-100 powder features a D90 value of 80.7 µm, which is 19.3 % less than the specified 100 µm. Similarly, the span of the powders is significantly lower for all three results, with a decrease ranging from 25 % to 34 % compared to their individual targets.

Table 5-6: D10, D50 and D90 and span targets and results for Ti-6Al-4V powders.

Powder	D10 in [µm]		D50 in [µm]		D90 in [µm]		Span in [µm]	
	target	result	target	result	target	result	target	result
LPBF_20-53	>20	22.2 ± 0.1	36.5	↓ 33.5 ± 0.1	<53	46.8 ± 0.2	33	↓ 24.6
Ti64_20-100	>20	25.6 ± 0.2	60	↓ 47.3 ± 0.9	<100	80.7 ± 0.5	80	↓ 55.1
EBM_45-106	>45	51.9 ± 0.4	75.5	↓ 71.2 ± 0.3	<106	92.1 ± 0.7	61	↓ 40.2

The frequency distributions of the particle size measurements are shown in Figure 5-6. The curves for the LPBF_20-53 and EBM_45-106 powders are nearly monomodal and Gaussian-shaped, exhibiting a slight positive skew or leftward deviation. In contrast, the Ti64_20-100 blend exhibits a bimodal distribution with two distinct local maxima around 30 and 70 µm, which align with the maxima of the two base powders.

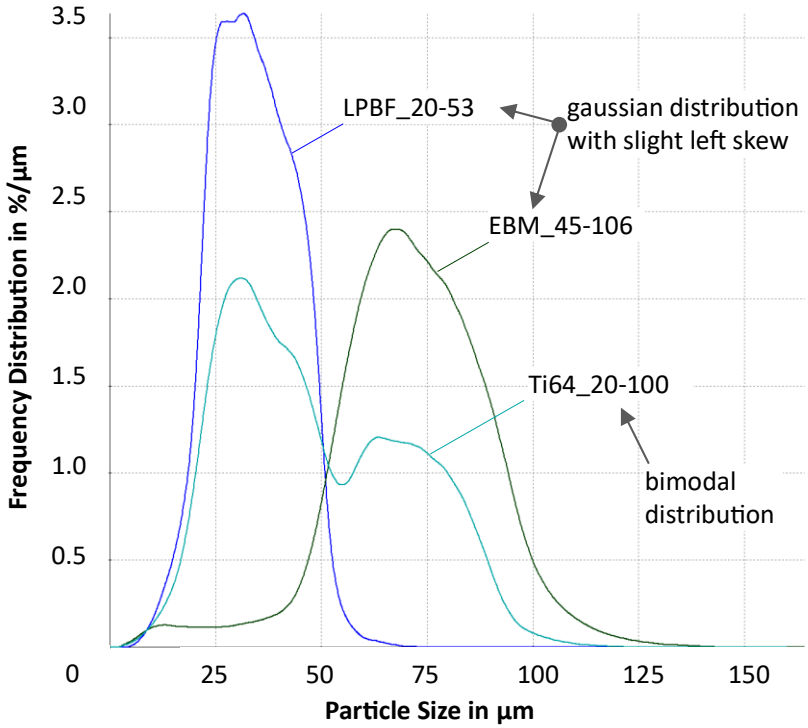

Figure 5-6: Diagram of the frequency distributions of Ti-6Al-4V powders.

5.2.1.4 Discussion of Ti-6Al-4V Particle Size Analysis

The D10 and D90 values for all three Ti-6Al-4V powders are within acceptable limits, although the D90 values are relatively low. For LPBF_20-53, the D90 value is 11.7 % lower, and for EBM_45-106, it is reduced by 13.1 %. This results in a lower D90 value for the blended Ti64_20-100 powder, measured at 80.7 µm, which is 19.3 µm below the target. A reduction in D90 by up to 10 % is common for metal powders, with a D90 of 90 µm marking the limit for Ti64_20-100 [166]. While, the two base powders are just slightly outside their limits, Ti64_20-100 exceeds these limits, indicating that an additional effect, such as segregation, potentially occurred before the blending process. This segregation likely took place during storage or filling of the V-blender, as stated by Schulze, preventing particles larger than 80 µm from being incorporated into the Ti64_20-100 blend [89].

The 100 µm sieve mesh is too small to effectively generate powders, with an upper limit of 100 µm. As reported by Smolina et al., it is typical to use a sieve with a mesh size larger than the target upper particle size; for example, they use a 75 µm sieve for a 20-60 µm powder [167]. Therefore, the sieving process likely excluded particles above approximately 90 µm, which is evident in the pronounced drop observed in the frequency distribution.

Additionally, the D10 value of Ti64-20-100 shows a typical increase of 3.4 µm compared to the D10 value of LPBF_20-53, consistent with common powder handling ranges as described by Cordova et al. [76]. The shift toward smaller distributions is reflected in the reduced D50 and span results, with all D50 values falling below target. The span for the powders is 25.4 % (LPBF_20-53), 31.1 % (Ti64_20-100) and 34 % (EBM_45-106) narrower than expected, which is notable considering that the narrowing of 25 % and 34 % is observed for commercially purchased powders.

The frequency distribution in Figure 5-6 of the EBM_45-106 powder shows an accumulation of small particles below 20 µm, a typical feature of virgin powder as described by Cordova et al. [76]. These small particles exhibit strong interparticle forces, making them difficult to separate through sieving and sifting. The resulting bimodal curve of Ti64_20-100 shows a gap in particles around 50 µm, corresponding to the particle sizes of LPBF_20-53 and EBM_45-106 powders. Xue et al. state that powder produced via plasma atomization typically exhibits a Gaussian distribution, as depicted in Figure 3-6 [50]. This suggests that particles around 50 µm are being excluded because they fall outside the limits for LPBF and EBM powders.

It should be noted that LPBF_20-53 and EBM_45-106 are sourced from different suppliers, which may contribute to this effect. The attempt to generate a wide, Gaussian-distributed PSD of 20-100 µm encounters limitations with these initial commercial powders, resulting in a bimodal distribution. This also suggests that further powder from the atomization process is usable for LPBF, if the particle gap around 50 µm is utilized.

In conclusion: The three Ti-6Al-4V powders fall within the specified limits for D10 and D90. The lower D90 values, particularly for the EBM_45-106 powder, result in the blended Ti64_20-100 being smaller than the targeted size. This trend is reflected in the D50 and span values of all three powders. The significant reduction in the D90 value of Ti64_20-100 is further influenced by prior segregation and the use of a 100 µm sieving mesh. Additionally, the gap between the two base powders contributes to the bimodal distribution observed in the blended powder.

5.2.2 Particle Shape

In the following sections, the results of the particle shape analysis are presented and discussed, with the analysis first applied to AlMg11 and then to Ti-6Al-4V.

5.2.2.1 Results of AlMg11 Particle Shape Analysis

The particle shape serves as well as a baseline characteristic for causal attributing differences in flowability, LPBF and mechanical properties for future comparisons. Therefore, potential differences in particle shape are identified. The sphericity, the symmetry, and the aspect ratio for each of the eight AlMg11 powders are presented in Table 5-7, with the morphology of LPBF_20-70 functioning as a reference. Deviations within a 5 % limit are classified as non-significant.

All investigated powders fall within the limits in terms of sphericity. For symmetry, PSD3_70-125 exhibits a value of 0.883, which is 0.001 below the lower limit of 0.884. Two significant deviations in aspect ratio are identified: 0.750 for OVS_70-170 and 0.739 for PSD3_70-125. Consequently, PSD3_70-125 displays the most irregular shape, with a symmetry reduction of 0.059 and an aspect ratio decrease of 0.083 compared to LPBF_20-70. Among the powders, PSD1_20-45 features the highest sphericity, with a value of 0.873.

Table 5-7: Sphericity (*SPHT*), symmetry (*Symm*) and aspect ratio (w_P/l_P) for AlMg11 powders, highlighting significant deviations.

	Powder	***SPHT**** [-]	***Symm**** [-]	w_P/l_P* [-]
reference	LPBF_20-70	0.856	0.930	0.793
deviation limits	± 5 %	0.813 - 0.899	0.884 - 0.977	0.754 - 0.833
	OVS_70-170	0.861	0.888	↓ 0.750
	PSD1_20-45	0.873	0.942	0.822
	PSD2_45-70	0.850	0.924	0.782
	PSD3_70-125	0.857	↓ 0.883	↓ 0.739
	PSD4_20-100	0.855	0.918	0.779
	PSD5_20-125	0.857	0.910	0.770
	PSD6_20-170	0.857	0.907	0.769

*STD < 0.006

Overall, the analysis of particle morphology reveals a trend of decreasing regularity with increasing particle size. A detailed breakdown of particle shape across defined size classes is demonstrated in Figure 5-7. The x-axis displays the upper limit of each particle size class, using PSD6_20-170 as an example. This powder includes both the LPBF_20-70 and OVS_70-170 powders, representing the full atomization batch, to illustrate shape variation with increasing particle size. The PSD of LPBF_20-70 µm is specifically highlighted to represent the shape characteristics typically intended for LPBF.

The most regular shapes are observed around 30 µm, within the LPBF 20-70 µm range. Shape characteristics decrease from 30 µm to 70 µm, then remain nearly consistent for particle size classes larger than 70 µm.

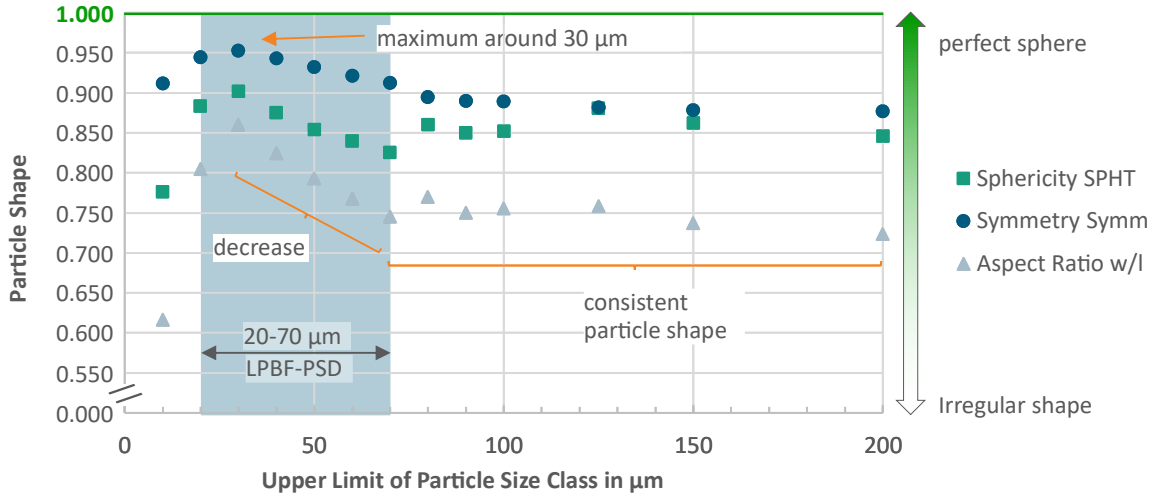

Figure 5-7: Diagram of particle shapes indicated by sphericity (*SPHT*), symmetry (*Symm*) and aspect ratio *(w/l*) across particle size classes for PSD6_20-170.

SEM images of LPBF_20-70 and PSD6_20-170 are shown in Figure 5-8 to qualitatively evaluate the particle shapes. A comparison between the reference sample, LPBF_20-70, and PSD6_20-170, representing the full atomization batch, reveals a mixture of spherical and irregular shaped particles. Agglomerations are visible in both powders, with larger particles (approximately above 100 µm) exhibiting more irregular shapes.

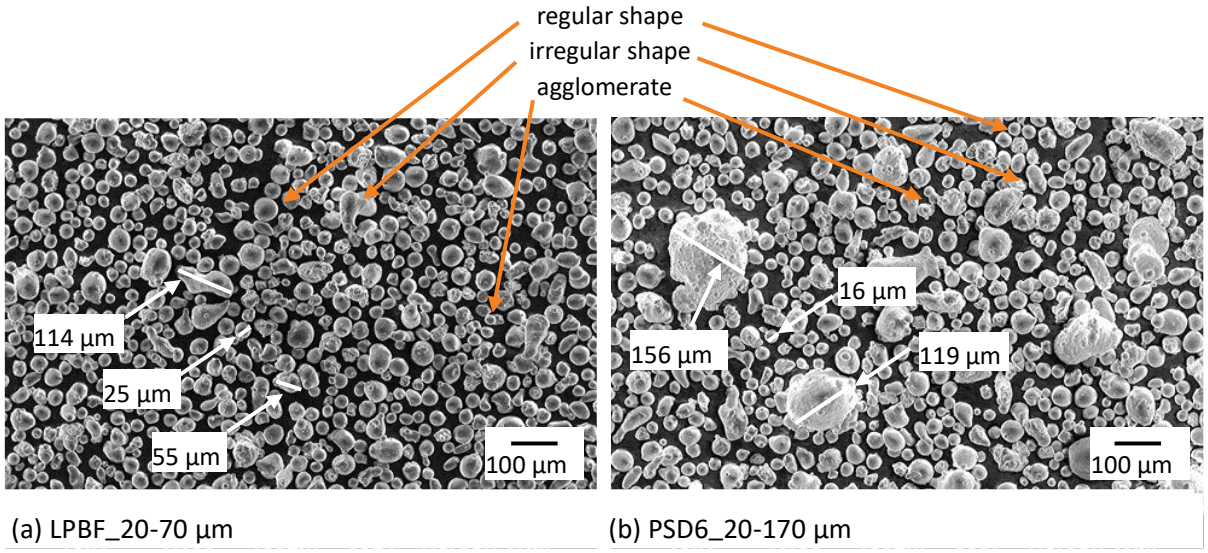

Figure 5-8: SEM images of (a) LPBF_20-70 and (b) PSD_20-170.

5.2.2.2 Discussion of AlMg11 Particle Shape Analysis

The sphericity of the AlMg11-PSDs remains within the 5 % deviation limit for similarity, with a slight decrease as particle size increases. The detailed analysis over particle size classes shows that particles in the LPBF range of 20-70 µm exhibit higher sphericity, symmetry and aspect ratio, whereas particles over 80 µm exhibit a consistent lower regularity. Two factors likely contribute to the lower regularity in particles above 80 µm: atomization process parameters and the initial sieving of the 20-70 µm powder.

According to Kassym and Perveen, during atomization, the particle surface solidifies first, preventing further deformation [168]. For particles up to 30 µm, the unsolidified particle's rotation and movement enhance sphericity. In the 30-70 µm range, slower solidification of larger surface areas leads to slightly more irregular shapes. Beyond 70 µm, the primary solidified surface inhibits further deformation. This material-dependent solidification is influenced by atomization parameters such as nozzle diameter and pressure, as outlined by Li et al. [8]. The higher sphericity observed within the 20-70 µm LPBF range suggests that atomization process parameters are adapted to this size distribution. Therefore, blending LPBF_20-70 with OVS_70-170 slightly reduces the sphericity of the larger generated PSDs.

Another factor contributing to the reduced shape values of particles above 70 µm, is the initial sieving of the LPBF_20-70 powder using a mesh size of 80 µm. The oversize powder is not sieved to the upper limit of around 170 µm. Irregularly shaped particles are less likely to pass through the mesh, so they are sorted out in the LPBF_20-70 powder, leaving more irregular particles in the larger PSDs. Therefore, the higher regularity of smaller powders, such as PSD1_20-45, results from sharper separation of irregular particles through sieving.

The qualitative SEM analysis confirms the quantitatively measured and calculated results from the dynamic image analysis. The slightly lower regularity of larger particles above 70 µm in PSD6_20-170, detected by dynamic image analysis, is confirmed, along with significantly larger particles such as the one highlighted with a size of 156 µm. Meier et al. also report that their SEM measurements for particle shape in four Ti-6Al-4V powders align with dynamic image analysis performed using a Camsizer XT [70]. The SEM analysis provides additional insights into particle surface characteristics and the formation of agglomerates and satellites. For efficiency and cost considerations, dynamic image analysis is sufficient to provide specific and quantitative results regarding powder morphology. Consequently, no further SEM images of PSD variations are analysed as extra qualitative verification in this thesis.

In conclusion: The particle shapes of the AlMg11 powders are comparable, in particular for sphericity no deviations are identified. PSD3_70-125 is slightly less irregular than the other powders, which aligns with the consistent lower regularity demonstrated in detailed analysis across particle size classes for particles above 70 µm. The detailed analysis demonstrates an adaption of the atomization process towards the LPBF PSD of 20-70, with the highest regularities in this particle size range. The SEM analysis supports the results from dynamic image analysis.

5.2.2.3 Results of Ti-6Al-4V Particle Shape Analysis

In Table 5-8, the particle shape characteristics of the Ti-6Al-4V powders are presented, with LPBF_20-53 serving as the reference. The other two powders fall within the 5 % deviation limits, indicating no significant deviations. Among the three powders, the EBM_45-106 powder exhibits the lowest degree of regularity, while Ti64_20-100, exhibits intermediate shape characteristics.

Table 5-8: Sphericity (*SPHT*), symmetry (*Symm*) and aspect ratio (w_P/l_P) for Ti-6Al-4V powders, including deviations.

	Powder	*SPHT**	Symm*	w_P/l_P*
reference	LPBF_20-53	0.893	0.954	0.896
deviation limits	target ± 5 %	0.848 – 0.938	0.906 - 1.0	0.851 - 0.941
	Ti64_20-100	0.888	0.943	0.881
no significant deviations identified	Δ in %	-0.005 ✓	-1.2 ✓	-1.7 ✓
	EBM_45-106	0.885	0.926	0.859
	Δ in %	-0.009 ✓	-2.9 ✓	-4.1 ✓

*STD ≤ 0.005

In Figure 5-9, a detailed visualization of the particle shapes across size classes for Ti64_20-100 is presented. As a blend of the other two powders, Ti64_20-100 encompasses the particle size range of 20-100 µm from the other two powders. Within the 20-80 µm range, particle shapes exhibit the highest values and therefore the highest regularity. Regularity decreases for particle sizes above 80 µm.

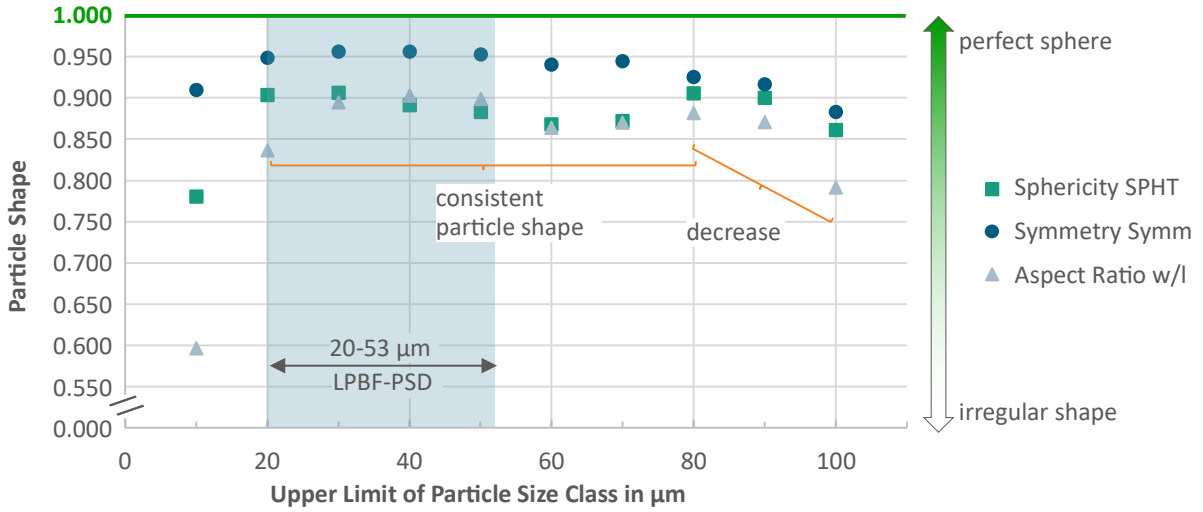

Figure 5-9: Diagram of particle shapes indicated by sphericity (*SPHT*), symmetry (*Symm*) and aspect ratio (*w/l*) across particle size classes for Ti64_20-100.

5.2.2.4 Discussion of Ti-6Al-4V Particle Shape Analysis

The morphology of the LPBF_20-53 exhibits higher regularity compared to the EBM_45-106 powder, resulting in an intermediate overall regularity for the blended Ti64_20-100 powder. The detailed analysis across particle size classes reveals that the particle shape remains consistent over a wide range from 20-80 µm. The Ti-6Al-4V powders, produced via plasma atomization, show higher regularity compared to powder produced via gas atomization, due to the precise control in plasma atomization, which aligns with Wallner's findings on the immediate melting of the electrode, resulting in highly spherical powder [74].

In conclusion: All three Ti-6Al-4V powders exhibit similar regularities, without significant deviations. The analysis across particle size classes confirms these results, with detailed insights into a consistent particle shape in the range of 20-80 µm.

5.2.3 Chemical Composition

In the following sections, the results of the chemical composition analysis are presented and discussed.

5.2.3.1 Results of Chemical Composition Analysis

The chemical composition of the powders is analysed to ensure consistency with the declared composition in the data sheet values and relevant standards. All deviations that potentially affect processability and manufacturability are identified to assess their possible influence. All chemical elements comply with the AlMg11 alloy data sheet shown in Table 5-9. The deviations, listed in the bottom row, indicate the highest variation as 0.08 wt.-% for titanium in LPBF_20-70.

Table 5-9: Chemical composition of AlMg11 compared to data sheet specification in wt.-% [9].

Powder	Al	Si	Fe	Cu	Mn	Mg	Be	Zn	Ti
Data sheet	Balance	0.07	0.07	< 0.01	<0.01	11	0.01	<0.01	0.00
LPBF_20-70	Balance	0.07	0.07	< 0,01	< 0,01	11	0.014	< 0,01	0.08
Δ	**-0.084**	0	0	0	0	0	**+0.004**	0	**+0.08**

The same applies to the chemical elements of the Ti-6Al-4V powders presented in Table 5-10. Both the LPBF_20-53 and the EBM_45-106 powders fall within the ELI-specification. Minor differences between LPBF_20-53 and EBM_45-106 are indicated in the bottom row, with the largest variation being 0.09 wt.-% in aluminium.

Table 5-10: Chemical composition of Ti-6Al-4V powders compared to ELI specification in wt.-% [41].

Powder	Ti	Al	V	Fe	C	N
Ti-6Al-4V - ELI	Balance	5.5-6.5	3.5-4.5	≤0.25	≤0.08	0.03
LPBF_20-53	Balance	6.26	4.02	0.16	0.005	0.014
EBM_45-106	Balance	6.15	4.0	0.15	0.01	0.02
Δ	**-0.055**	**-0.09**	**-0.02**	**-0.01**	**+0.005**	**+0.06**

For both AlMg11 and Ti-6Al-4V alloys, the oxygen, and hydrogen content of the reference PSDs (AlMg11: 20-70 µm; Ti-6Al-4V: 20-53 µm) and the larger PSDs (AlMg11: 20-125 µm; Ti-6Al-4V: 45-106 µm) are analysed. This analysis aims to determine whether differences in specific surface area contribute to variations in oxygen and hydrogen uptake.

The oxygen and hydrogen values of the AlMg11 powders, with LPBF_20-70 as the reference and PSD5_20-125 representing the wide PSD for increased atomization yield, are shown in Figure 5-10. Compared to LPBF_20-70, the PSD_20-125 powder features an oxygen content that is 35 µg/g (27.1 %) lower and a hydrogen content that is 6 µg/g (21.4 %) higher. Both differences exceed 5 % and therefore classify as significant.

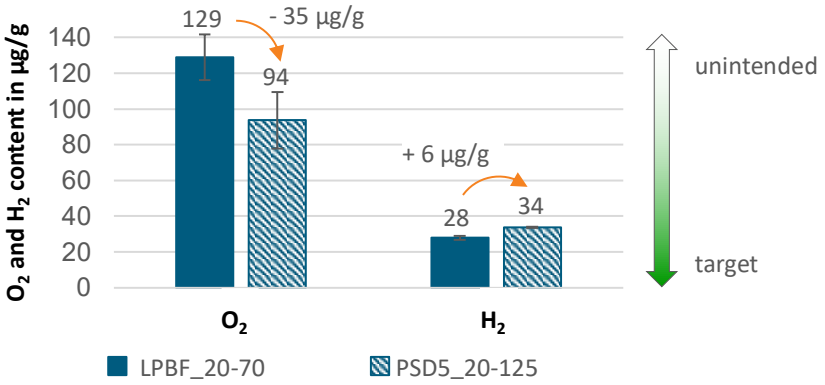

Figure 5-10: Diagram of O_2 and H_2 content of AlMg11-powders LPBF_20-70 and PSD5_20-125.

The results of the oxygen and hydrogen measurement for the Ti-6Al-4V powders, LPBF_20-53 and EBM_45-106, are shown in Figure 5-11. The decreases of 0.005 µg/g (0.6 %) for oxygen and 0.002 µg/g (66.7 %) for hydrogen in the EBM_45-106 powder are minimal in absolute terms. Hydrogen exceeds the 5 % deviation limit, classifying it as significant.

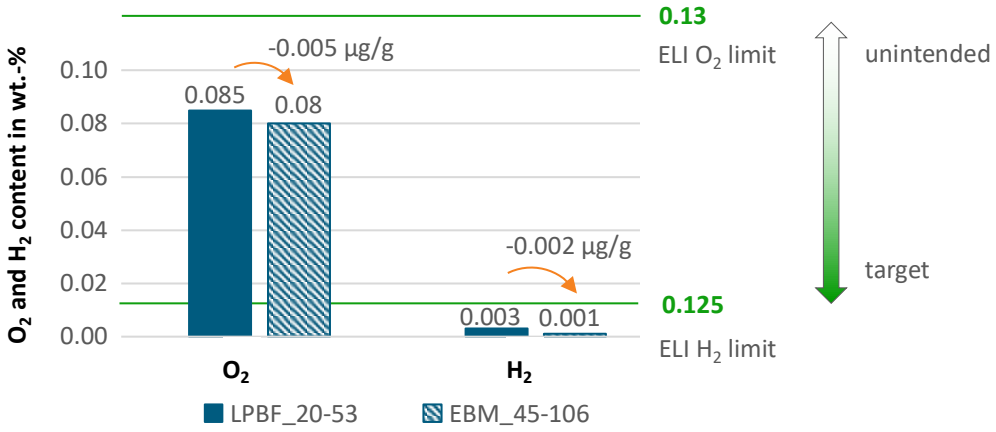

Figure 5-11: Diagram of O_2 and H_2 content of Ti-6Al-4V powders LPBF_20-53 and EBM_45-106.

5.2.3.2 Discussion of Chemical Composition Analysis

The individual alloying elements are well harmonized to achieve the desired alloy composition for both AlMg11 and Ti-6Al-4V alloys. Potential differences in processability or mechanical properties are therefore not attributable to the chemical composition of the powders.

The oxygen measurement shows in tendency towards decreasing oxygen content as particle sizes increases for AlMg11 above 70 µm, and for Ti-6Al-4V above 53 µm. Larger particles possess a relatively smaller specific surface area, resulting in a lower volume and mass to surface ratio. If all particles exhibit a similar rate of oxygen absorption (per alloy) and build up a thin oxide layer, smaller particles feature a higher relative oxygen uptake [70]. The larger surface area of smaller particles in a 0.25 g sample leads to higher oxygen content in smaller PSDs, such as LPBF_20-70, compared to PSD5_20-

125. For AlMg11, no established VDI, DIN or ISO standard is identified, to regulate oxygen and hydrogen content, leaving the material data sheet as the only reference for comparison. However, the current data sheet does not specify limits for oxygen and hydrogen levels.

The higher hydrogen content in the PSD5_20-125 powder suggests an assumption that requires further validation in future studies: During the atomization process, hydrogen may be absorbed from the atmosphere. Larger particles, due to slower cooling rates, remain in the melting phase for a longer period, which extends their exposure to hydrogen sources, potentially leading to higher hydrogen uptake.

The variations in oxygen and hydrogen content in the AlMg11 powder present a potential opportunity to influence its processability and manufacturability, for example increasing brittleness as reported by Meier et al. [70]. If such differences are observed, it becomes essential to account for these oxygen and hydrogen levels.

For the Ti-6Al-4V powders, the small deviations are unlikely to affect further analysis. Since all values remain below the limits set by the ELI-standard, these contents are not considered when evaluating processability and manufacturability. [41]

In Conclusion: The powders for both alloys, AlMg11 and Ti-6Al-4V, align with their respective data sheets and standard limits. No influence of the overall chemical composition is therefore expected. For AlMg11, the reference PSD_20-70 exhibits a significant larger oxygen content, which is likely to affect mechanical properties such as increased brittleness.

5.2.4 Key Findings on Powder Characterization

The particle size and distribution are measured to determine the gap between the target and actual generated PSDs. The characterization of particle shape and chemical composition aims to identify differences between the powders that potentially affect their processability and manufacturability, enabling the attribution of future deviations. The theoretical objective of the defined PSD variation is to ensure that PSD is the only differentiating factor between the powders to isolate their influence. Therefore, if no differences are identified, no influence of other powder characteristics is expected.

Table 5-11: Overview of the characterization results of particle size, particle shape and chemical composition for AlMg11 and Ti-6Al-4V powders.

Criteria	Result AlMg11		Result Ti-6Al-4V	
particle size	• PSDs are within D10 and D90 limits	✓	• PSDs are within D10 and D90 limits	✓
	• Shift towards smaller particles identified in D50 and span results	↯	• Ti64_20-100: small D90 value of 80.7 µm and bimodal distribution	↯
			• LPBF_20-53 and EBM_45-106 monomodal distribution	✓
particle shape	• Highest regularity around 30 µm	✓	• Highest regularity between 20-80 µm	✓
	• Decrease of regularity between 30-70 µm	✓		
	• Consistent particle shape above 70 µm	✓	• Increase in irregularity above 80 µm	✓
chemical composition	• Alignment to datasheet	✓	• Alignment to ELI specification	✓
	• PSD5_20-125 lower oxygen and higher hydrogen content than LPBF_20-70	↯	• Similar oxygen and hydrogen contents	✓

Identified differences in the powder characteristics include a bimodular distribution in the Ti64_20-100 powder, and for the AlMg11 powders, a lower oxygen and higher hydrogen content in PSD5_20-125 compared to LPBF_20-70. These differentiating factors are likely to influence subsequent investigations.

Despite gaps between the theoretical target and actual powder characteristics, the sub-question, “Can different PSDs be generated from commercial PSDs for LPBF?”, is overall confirmed. The foundation for analysing the processability and manufacturability of the PSD variations is established.

6 Processability and Manufacturability of varied PSDs using AlMg11

Processability refers to whether a powder (specifically a PSD in this thesis), exhibits the feasibility to generically print defect-free in LPBF. To assess processability, the effect of increased PSD on flowability and LPBF are considered. The AlMg11-tests focus on identifying the powder with the highest atomization yield that remains processable. The reference LPBF_20-70 and the two powders with the highest atomization yield and confirmed processability are then used to manufacture specimens for mechanical property analysis, using the same process parameters. This enables the examination of the influence of different PSDs on manufacturability.

6.1 Processability

In the following sections, the results of the processability analysis are presented, discussed and compared to the reference values from the AlMg11 data sheet.

6.1.1 Flowability

The influence of the PSD variation on the flowability as one indicator for the processability is analysed in this section. To apply distinct stresses to the powder, multiple tests are performed using a Hall funnel and a rotating drum.

6.1.1.1 Results of Flowability Analysis using the Hall Funnel

The results of the AlMg11-flowability measurements using the Hall funnel are presented in Table 6-1. PSD6_20-170 exhibits the highest apparent density at 1.40 g/cm³, while the narrow distributions, PSD1_20-45 and PSD2_45-70, feature the lowest apparent densities at 1.28 g/cm³. The highest tapped densities are observed for the large distributions, PSD5_20-125 and PSD6_20-170, at 1.52 g/cm³. With all powders showing similar tapped densities, except for PSD3_70-125 which, as the only powder consisting solely of particles larger than 70 µm, exhibits a lower tapped density. PSD6_20-170 features the lowest Hausner ratio at 1.09, while PSD1_20-45, PSD2_45-70 and PSD5_20-125 display the highest Hausner ratios at 1.16. In the Hall flowability measurements, there is a gap in the table for powders that cannot flow through the funnel without multiple tapping, rendering a valid measurement impossible. PSD3_70-125 demonstrates the fastest Hall flowability, taking 44.4 s to pass 50 g of powder.

Table 6-1: AlMg11 results of apparent and tapped density, Hausner ratio and Hall flowability measurements.

Powder	Apparent Density in [g/cm³]	Tapped Density in [g/cm³]	*Hausner Ratio* [-]	Hall Flowability in [s/50 g]
LPBF_20-70	1.32 ± 0.01	1.51 ± 0.00	*1.15*	/
PSD1_20-45	1.28 ± 0.00 ↓	1.49 ± 0.01 ↓	*1.16* ↑	/
PSD2_45-70	1.28 ± 0.00 ↓	1.48 ± 0.00 ↓	*1.16* ↑	/
PSD3_70-125	1.26 ± 0.00 ↓	1.41 ± 0.01 ↓	*1.12* ↓	48.5 ± 0.33
PSD4_20-100	1.34 ± 0.07 ↑	1.50 ± 0.01 ↓	*1.12* ↓	/
PSD5_20-125	1.31 ± 0.0 1 ↓	1.52 ± 0.00 ↑	*1.16* ↓	53.2 ± 0.20
PSD6_20-170	1.40 ± 0.10 ↑	1.52 ± 0.01 ↑	*1.09* ↓	51.7 ± 0.68

6.1.1.2 Discussion of Flowability Analysis using the Hall Funnel

According to Hausner's flowability classifications, PSD6_20-170 is rated as “excellent”, while all other powders fall into the “good” category [140]. However, no specific references for AlMg11 flowability measurements are found, limiting comparisons to the powders examined in this study. Baitimerov et al.'s investigations on AlSi12 powders report an apparent density of 1.28 g/cm³, which is within a comparable range [18]. Due to the strong dependency on the alloy’s relative density, a direct comparison of these results is not applicable.

Marchetti and Hulme recommend using a mix of small and large particles (20-40 and 56-71 µm) to achieve a plateau of tapped densities around 4.2 g/cm³ (steel), which aligns with the results of the AlMg11 funnel tests [108]. The widest PSD distributions (PSD5_20-125 and PSD6_20-170) show the highest tapped densities, likely due to fine particles filling the gaps between larger particles, reducing cavity formation and resulting in higher powder densities [99]. This is consistent with observations that a wider PSD tends to maximize packing efficiency. In contrast, the powder composed of only large particles (PSD3_70-125) exhibited the lowest tapped density, further supporting the advantage of a wide PSD in achieving higher tapping density. A similar trend is observed in apparent density, although it is less pronounced than in tapped density.

Since the particle shape is known for affecting the flowability, Haferkamp et al. proposed that a decrease in particle shape regularity increases the Hausner ratio [90]. This effect is not observed in the AlMg11 results, as the most regularly shaped powder, PSD1_20-45, exhibits the highest Hausner ratio and thus the lowest flowability. This suggests that interparticle forces among smaller particles play a more significant role in limiting flowability than particle shape. It also indicates that, beyond a certain point, the influence of interparticle forces, driven by surface area and particle size, surpasses the effects of particle shape on flowability. Given the overall similarity in particle shapes, these assumptions require further validation with powders exhibiting more pronounced differences in particle shape.

Only three powders meet the flowability requirements to pass the Hall flowability test. For future measurements, using a funnel with a larger diameter, such as a Carney funnel, is recommended for non-free-flowing powders [169]. This adjustment would ensure more accurate measurement of powders with poor flowability. PSD3_70-125, composed only of large particles, exhibited faster Hall flowability than PSD5_20-125 and PSD6_20-170, both of which contain particles smaller than 70 µm. This observation, where larger particles improve flowability by reducing interparticle interactions, is widely supported in the literature, for example by Balbaa et al. and Spierings et al. [20, 27]. It appears that the absolute particle size exerts a greater influence on flowability than the span of the PSD, as larger particles tend to overcome cohesive forces that inhibit the flow of smaller particles [18].

The transfer of compactibility to powder recoating is limited, as powder layers in LPBF are applied without tapping. Consequently, Spierings et al. and Soh et al. suggest that the Hausner ratio is a limited indicator of flowability for LPBF applications [27, 170]. However, the PSD applied, is influenced by the powder recoating speed. Lee et al. demonstrate through Discrete Element Method (DEM) simulations that higher recoating speeds tend to favour the deposition of smaller particles [169]. Therefore, while the Hausner ratio provides insight into powder packing characteristics, its direct application to LPBF requires careful consideration of the recoating speed and PSD [171].

In conclusion: The Hausner ratio classification indicates that the powders fall within the “good” and “excellent” categories. For achieving high apparent and tapped densities, a mixture of particles smaller and larger than 70 µm is recommended. Regarding Hall flowability, the presence of larger particles and a reduction in the amount of small particles leads to a decrease in the Hall flowability time.

6.1.1.3 Results of Flowability Analysis using the Rotating Drum

The rotating drum test offers a measurement that mimics the recoating process through the rotation. Therefore, combining compression and shear stresses are applied to the powder. In Figure 6-1, the results of the rotating drum measurements are presented, separated into (a) avalanche angle and (b) cohesion index.

The AlMg11 powders exhibit increasing avalanche angles with increasing rotational speed. PSD1_20-45 shows a distinct behaviour with a predominantly consistent avalanche angle, regardless of the increasing rotational speeds. The avalanche angles of LPBF_20-70, PSD4_20-100, and PSD6_70-170 are notably lower at higher speeds, particularly above 25 rpm. PSD2_45-70, PSD3_70-125, and PSD5_20-125 reach the highest avalanche angles. Except powder PSD2_45-70, all powders fall below the processable limit of 30° until a rotational speed of 15 rpm. Above that speed, all powders expect PSD1_20-45 exceed this limit.

The curves for the cohesion indices closely mirror those of the avalanche angles. PSD1_20-45, PSD2_45-70, and LPBF_20-70 demonstrate the highest cohesion indices, while PSD3_70-125 and PSD6_20-170 show the lowest across all rotational speeds. Fluctuations are observed at lower speeds, particularly in the range of 2-6 rpm. Until 15 rpm, all powders expect PSD1_20-45 and PSD2_45-70 are below the passable limit. At rotational speeds exceeding 25 rpm, the powders separate, with those containing particles smaller than 70 µm above the limit, while powders with particles larger than 70 µm remain below the limit.

The powders differ in the rotational speed at which their behaviour transitions from flowing to tossing. The narrow PSDs, such as PSD1_20-45 and PSD2_45-70, begin tossing at 35 rpm, whereas the large PSDs, such as PSD3_70-125, do not toss at all. Consequently, the results for these powders are truncated at the rotational speed where the first toss occurs.

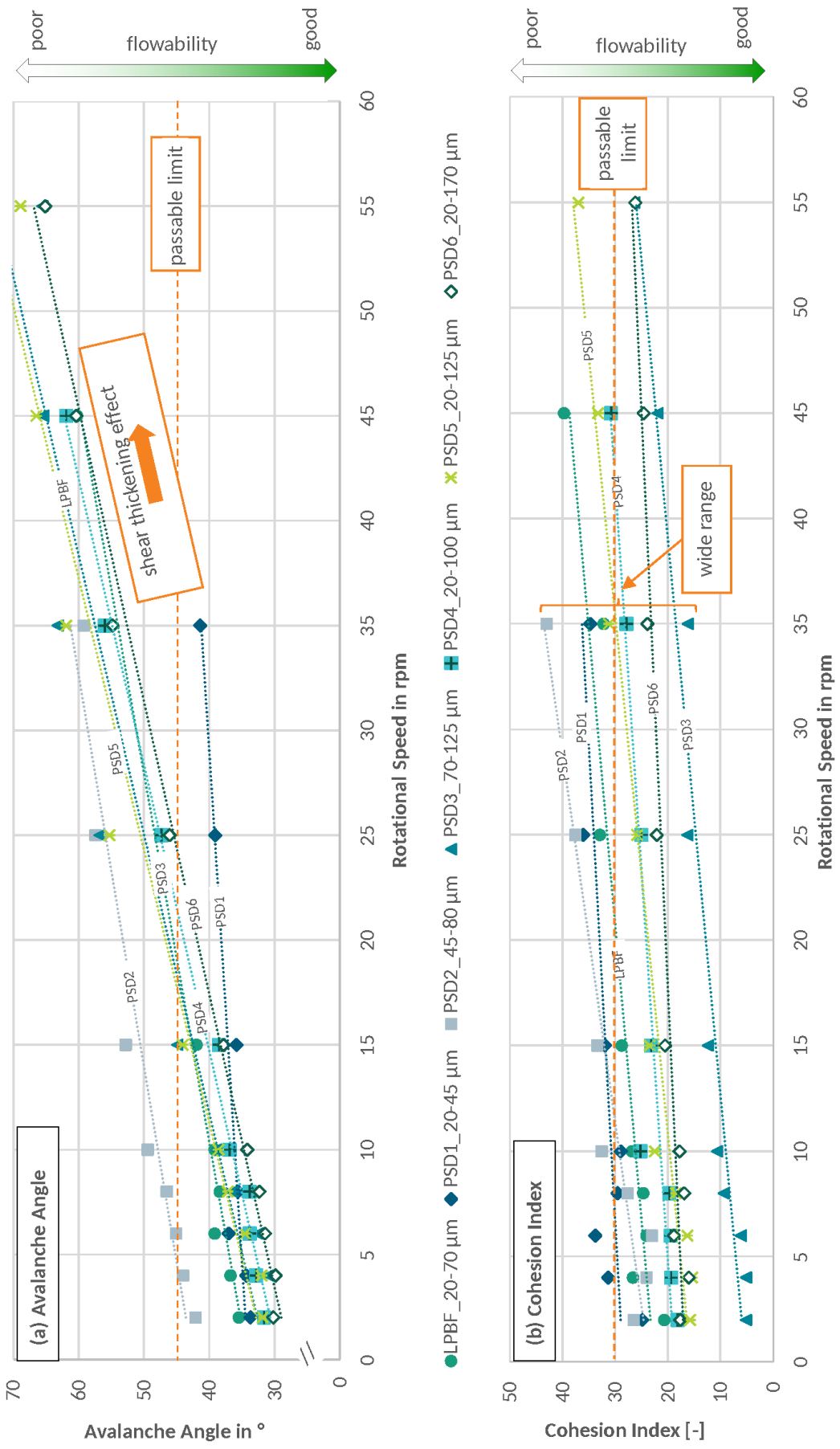

Figure 6-1: Diagrams of (a) avalanche angles and (b) cohesion indices across rotational speeds measured with GranuDrum for the AlMg11 powders.

For a detailed analysis of the correlation between particle size and avalanche angles, the avalanche angles for the AlMg11 powders are plotted in Figure 6-2 over the D10, D50, and D90 values at three exemplary rotational speeds: 4, 10, and 35 rpm. The outline connects the avalanche angles of each powder at these speeds. The D10 values in (a) show more variability around 30 µm, but remains consistent with the overall trend. In (b) D50 and (c) D90, a trend of larger outlines for higher particle sizes is observed.

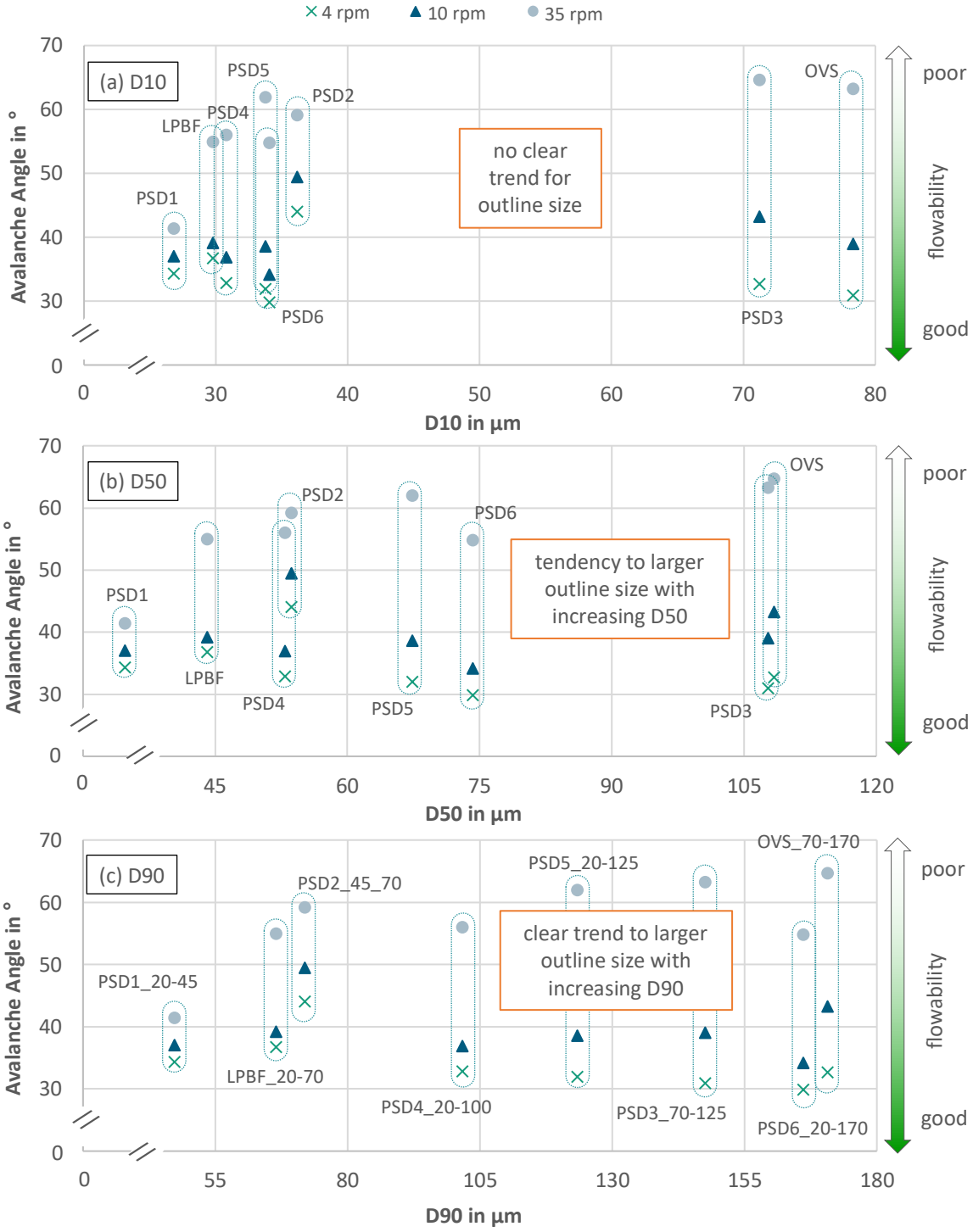

Figure 6-2: Diagrams of avalanche angles of AlMg11 powders measured at 4, 10 and 35 rpm over (a) D10, (b) D50, (c) D90.

6.1.1.4 Discussion of Flowability Analysis using the Rotating Drum

An avalanche angle below 35° is classified as “good” flowability, demonstrating ease of flow according to Muthuswamy et al. [71]. Up to 15 rpm, all powders except PSD2_45-70 remain below this threshold, showing “good” flowability. The tendency of increasing avalanche angles with higher rotational speeds across all AlMg11-powders, indicates a shear-thickening effect, which reduces ease of flow. No clear trend emerges to suggest that a particular PSD consistently leads to lower avalanche angles. PSD1_20-45 presents the overall lowest avalanche angles across the range of rotational speeds, while PSD2_45-70 shows the highest. Therefore, it is not possible to conclude that a narrow distribution enhances flowability. The PSDs LPBF_20-70, PSD4_20-100 and PSD6_20-170 display similar avalanche angles, but PSD5_20-125, despite featuring size and distribution between PSD4_20-100 and PSD6_20-170, exhibits an avalanche angle approximately 10° higher.

The cohesion index values reveal a comparably strong adhesion of the PSD1_20-45 particles due to interparticle forces. Studies by Li et al. and Meier et al. demonstrate that particles below 53 µm experience higher interparticle forces, reducing flowability [8, 84]. These smaller particles require higher external forces (gravity, shear stresses) to overcome interparticle forces, such as van der Waals or hydrogen bonds. The shear-thickening effect is less pronounced for the small PSD1_20-45, as the increase in avalanche angles across increasing rotational speeds occurs more gradual. This is likely due to the “break-up” of interparticle forces by shear stresses. In contrast, larger particles exhibit lower interparticle forces relative to their specific surface area, resulting in lower friction and higher gravitational forces, which facilitate easier flow.

The detailed analysis of the avalanche angle evolution with particle size, as shown in Figure 6-2, confirms an influence of PSD on the flowability. As particle sizes increase, there is a general trend toward higher avalanche angles, with shear thickening becoming more pronounced, illustrated by larger outlines in the graphs.

Cohesion indices for larger and wider PSDs, from PSD3_70-125 to PSD6_20-170, remain below 30 at rotational speeds up to 35 rpm. These powders form smoother and more even surfaces, with lower cohesion indices compared to the relatively smaller and narrower PSDs, PSD1_20-45 and PSD2_45-70. This is explained by lower interparticle forces due to the lower specific surface area of the larger particles. Additionally, smaller particles fill the voids between larger ones, counterbalancing the surface evenness. However, the slightly higher cohesion index for the wider PSD6_20-170 compared to the large PSD3_70-125 indicates that the sticking effect of interparticle forces among smaller particles is stronger than the void-filling effect, which evens out the surface. Notably, the avalanche angle may be a more sensitive indicator of powder flowability than the cohesion index.

At 35 rpm, the smaller PSDs, such as PSD1_20-45 and PSD2_45-70, begin to exhibit tossing behaviour instead of flowing, whereas the larger PSDs (PSD4-6) maintain flow. The earlier onset of tossing in narrow and small PSDs is attributed to the lower mass of smaller particles, which are more susceptible to tossing under stress compared to larger particles [8]. A slight trend toward delayed tossing at higher rotational speeds is observed in wider PSDs, PSD6_20-170 and PSD5_20-125, compared to narrower distributions, such as PSD2_45-70. The presence of additional small particles below 45 µm may contribute to higher friction and stronger interparticle forces, leading to more robust connections between particles [31, 84]. This suggests that powder recoating may be more even with a wider PSD compared to a narrow, solely large PSD.

The transfer of GranuDrum's rotating speed to LPBF's recoating angular speed is limited, as angular speed represents only a single radius at a time and does not account for the three-dimensional powder dynamics inside the drum [172]. An LPBF typical recoating speed of 150 mm/s is achieved at around 35 rpm at the drum's edge, which is the highest possible rotational speed for PSD1_20-45 and PSD2_45-70 without tossing. A transfer of flowability measurements results to LPBF recoating behaviour requires verification with other tests, such as specialized powder recoater test rigs or monitoring systems in the building chamber of the LPBF machine. Further research should explore adjusting recoating speeds based on PSD, as slower speeds may benefit larger particles to ensure an even powder bed during recoating.

In conclusion: Up to 15 rpm, most powders show "good" flowability, but shear thickening occurs at rotational speeds above 15 rpm without a clear PSD trend. Smaller PSDs (PSD1_20-45) exhibit strong interparticle forces, which shear stresses partially break up. Larger PSDs (PSD5_20-125) exhibit lower interparticle forces, leading to earlier flow, with an increase in shear thickening. Wider PSDs (PSD3-6) exhibit lower cohesion indices and therefore smoother surfaces, with smaller particles filling voids between larger ones. Smaller PSDs (PSD1-2) start tossing earlier at 35 rpm, while wider PSDs (PSD3-6) maintain more even flow, suggesting better recoating potential for wider distributions.

6.1.2 LPBF

In the following sections, the results of the LPBF analysis are presented and discussed.

6.1.2.1 Results of LPBF Analysis

The influence of increased PSD on LPBF is investigated by analysing the processability of the generated PSD variations. Subsequently, the two PSDs that exhibit defect-free processability with a relative density above 99.5 %, along with the highest atomization yield, are selected for comparison with LPBF_20-70 in terms of manufacturability. In Figure 6-3, the relative densities achieved for each scanning speed variation across the different powders are presented.

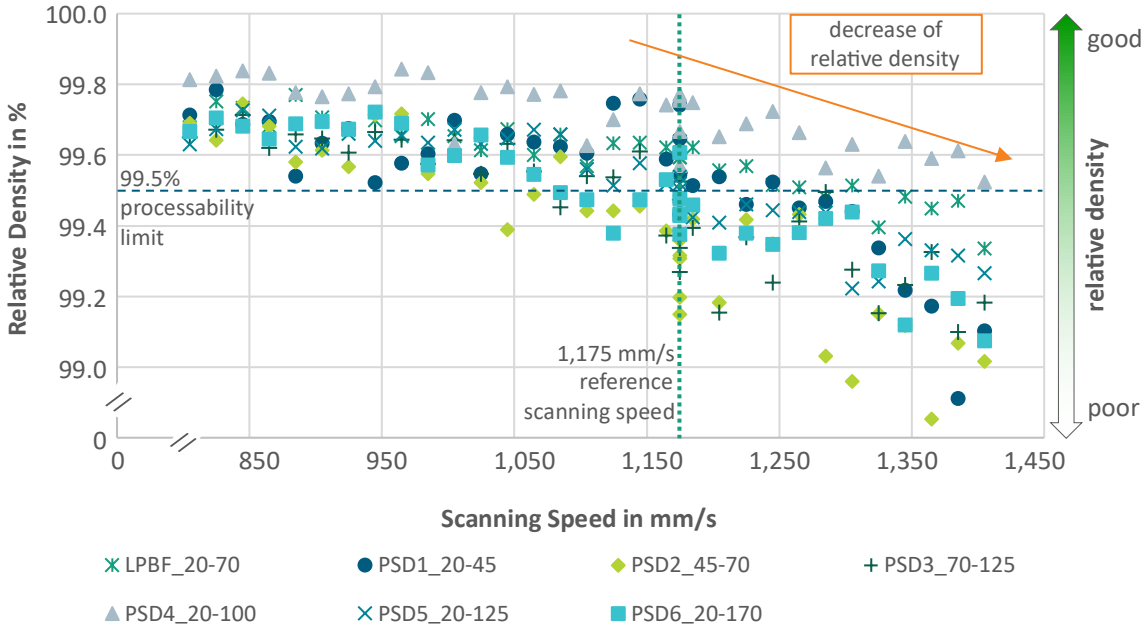

Figure 6-3: Diagram of the relative densities for AlMg11 powder across scanning speeds.

The reference scanning speed of 1,175 mm/s and the reference relative density threshold of 99.5 % (according to the data sheet) are highlighted. All the powders achieve relative densities above 99.0 %, across the scanning speed range, except for three outliers from PSD1_20-45 and PSD2_45-70 at scanning speeds from 1,305 until 1,385 mm/s. At scanning speeds above 1,050 mm/s, the relative density tends to decrease and exhibit higher deviations. PSD4_20-100 features the highest overall relative densities, followed by LPBF_20-70 and PSD5_20-125. The narrow distribution PSD2_45-70 demonstrates the lowest overall relative densities.

As powders with the highest atomization yield and sufficient processability, demonstrated by achieving relative densities above 99.5 % across a wide scanning speed range from 805 mm/s to 1,405 mm/s and 1,185 mm/s respectively, PSD4_20-100 and PSD5_20-125 are selected for manufacturability analysis. These powders, along with LPBF_20-70 as a reference, are used to manufacture specimens for mechanical testing. The same reference process parameters are applied to ensure an accurate assessment of the influence of increased PSDs on manufacturability.

6.1.2.2 Discussion of LPBF Analysis

The AlMg11-scanning speed variation reveals a clear trend toward higher relative densities at lower scanning speeds, irrespective of the PSD and other powder characteristics. This indicates that higher relative densities correlate with increased VED. A notable difference between the powders emerges at higher scanning speeds, particularly above 1,050 mm/s and therefore lower VEDs (< 71.4 J/mm³). While the reference scanning speed of 1,175 mm/s is set for balancing productivity and processability, PSD6_20-170 and PSD2_45-70 fail to achieve relative densities above 99.5 % at this speed.

Andani et al. observe that reducing scanning speed from 2100 mm/s to 1650 mm/s decreases melt pool dynamics for AlSi10Mg, with particle sizes comparable to LPBF_20-70, which aligns with these findings [173]. At scanning speeds above 1,050 mm/s, the increased turbulence in the melting zone creates critical disturbances that result in irregularities in the density cubes for the investigated powders [173]. Only PSD4_20-100 shows higher relative densities than the reference LPBF_20-70 powder, followed by PSD5_20-125. Both powders also exhibit higher tapped densities, which may lead to improved powder layer densities after recoating. The larger powders, PSD3_70-125 to PSD6_20-170, feature a lower cohesion index (below 30) at higher rotational speeds (15-45 rpm), enhancing the formation of a more homogeneous powder bed during recoating. This effect could contribute to reduced turbulences in the melt pool at speeds above 1,050 mm/s. These findings suggest that a broad, but not excessively wide (below a span of 90 µm) PSD promotes a more stable melting zone, resulting in higher relative densities.

However, powders consisting solely of larger particles, such as PSD2_45-70 and PSD3_70-125, show relative densities below 99.4 % at scanning speeds above 1,050 mm/s. The absence of particles below 45 µm in the distribution may increase turbulences in the melt zone. Across the full range of scanning speeds, PSD4_20-100 yields the highest relative densities, indicating the widest process window. This confirms that a balanced combination of small and large particles leads to more stable processing conditions. Nevertheless, overly broad distributions, such as PSD6_20-170, result in lower relative densities. While recoater movement differs from GranuDrum rotations, the process window observed aligns with the trends seen in the avalanche angle measurements.

Xue et al. state that insufficient energy input during LPBF causes only the particle surface to melt, leading to vaporization and spatter. Recoil pressure also presses unmelted particles into the melting

pool, contributing to porosity. Proper parameter adjustment to match the PSD is critical to achieving high relative densities [50]. The reproducibility of these results must be validated for all investigated powders. The target for future process parameter studies may vary, depending on the desired productivity or quality.

In conclusion: Based on the processability investigations, PSD4_20-100 and PSD5_20-125 are identified as the most promising powders combining processability and high atomization yield (62 and 74 %, see Table 4-1). Both powders are selected for manufacturability analysis in comparison with LPBF_20-70, using the same process parameter. Notably, the process parameters are primarily defined by the characteristics of the largest particles.

6.1.2.3 Results of Powder Application Test

The powder application test is performed for the three powders LPBF_20-70, PSD4_20-125 and PSD5_20-125 selected for manufacturability analysis. The results are shown in Figure 6-4.

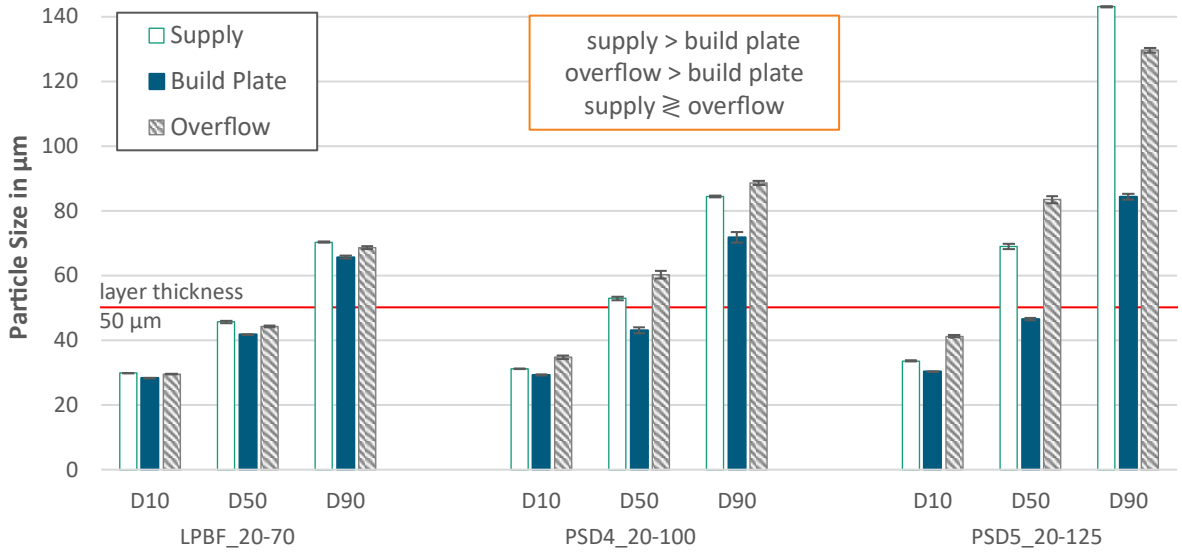

Figure 6-4: Bar chart of the particle size from the supply, build plate, and overflow measured for AlMg11 powders.

The set layer thickness of 50 µm is indicated with a red line. For all three powders, the particle size of samples taken on the build plate is smaller than of samples taken from the supply. For PSD4_20-100 with 45.5 % of particles and for PSD5_20-125 with 32 % of particles smaller than the 50 µm layer thickness, this trend is more pronounced. The average D90 values on the build plate are 65 µm for LPBF_20-70, 72 µm for PSD4_20-100 and 84 µm for PSD5_20-125, which is larger than the layer thickness.

6.1.2.4 Discussion of Powder Application Test

The observed decrease in particle size of samples taken from the build plate indicates that not all larger particles are successfully applied during the process. Although a layer thickness of 50 µm, particles exceeding 50 µm still appear on the build plate. Previous investigations, such as Wischeropp et al., report a gap over the parts three times higher than the layer thickness due to solidification shrinkage, which facilitates the placement of particles above 50 µm [26]. The D90 values of PSD4_20-100 with 71.8 µm and 84.33 µm, with 10 % of the particles exceeding these values, show that for example, 3.9 % of particles are between 100-125 µm for PSD5_20-125. Notably, the D90 of 84.33 µm of PSD5_20-125 on the build plate is similar to 84.4 µm of D90 of PSD4_20-100 in the supply, confirming the feasibility

of a placement of all applied particles size for PSD4_20-100. The simulation of Lee et al., demonstrates a segregation during recoating resulting in the application of smaller particles and shifting larger particles into the overflow. It appears that this segregation effect took place to a certain degree [171]. More detailed analysis is required to investigate the influence of the segregation compared to the limited space between previous applied powder layers for powders with increased PSD.

The effect of PSD coarsening due to powder re-use is identified for PSD4_20-100 and PSD5_20-125. Kohlwes et al. report a 4 % higher spatter count for a 20-125 µm powder compared to a 1 % increase in a powder with 20-100 µm compared to a typical LPBF PSDs, which aligns with the observed coarsening trends [162]. However, the decrease in D90 for PSD5_20-125, suggesting that either the spatters are smaller than D90 overflow of 129 µm for PSD5_20-125 or too few to influence the D90 values. Additionally, the D90 value from initial characterization for PSD5_20-125, is with 123.4 µm lower than 143 µm in the supply, which indicates particle segregation, potentially necessitating immediate processing after blending.

In conclusion: A decrease in particle size is observed in the powders on the build plate compared to the particle sizes in both the supply and overflow. The powder, with a D90 of 84 µm, is successfully applied at a layer thickness of 50 µm.

6.1.3 Key Findings on Processability

In this section, the research question “What is the effect of the PSD on processability?” is addressed. Processability is analysed as defined by the generic defect-free printability of a powder, including the key aspects such as sufficient flowability and effective powder application. The main findings are presented in Table 6-2.

Table 6-2: Key Findings of the investigations on the effect of AlMg11 PSDs on processability.

Criteria	Result AlMg11
Flowability using Hall funnel	• Hausner ratio: Powders within Hausner classification “good” and “excellent” • Apparent and tapped density: For high values, mix of small and large particles recommended • Hall flowability: larger particles and a reduced number of small particles reduce Hall flowability time
Flowability using rotating drum	• Shear thickening effect for all investigated powders • Avalanche angle: mixed results – no clear trend • Cohesion index: wide PSDs (PSD3 to PSD6) yield lower values
LPBF	• From 805 to 1,025 mm/s all PSD variations above 99.5 % relative density • PSD4_20-100 and PSD5_20-125: largest process windows • Selected for mechanical tests in comparison to LPBF_20-70
Application Test	• Decrease of particle size on build plate compared to particle size in supply and overflow • Application of powder with a D90 of 84 µm at 50 µm layer thickness

Increasing the PSD affects processability by enhancing flowability, increasing apparent and tapped densities, reducing Hausner ratios, and lowering Hall flow time. PSD4_20-100 and PSD5_20-125 increase the atomization yields up to 62 and 74 %, while achieving stable flow behaviour, and a large process window with relative densities above 99.5 %. They are selected to investigate the impact of increased PSD on LPBF manufacturability compared to LPBF_20-70.

6.2 Manufacturability

With each of the three selected powders, LPBF_20-70, PSD4_20-100 and PSD5_20-125, mechanical specimens are manufactured using the reference process parameters. The investigation of the mechanical properties allows for assessing the manufacturability of increased PSDs.

6.2.1 Mechanical Properties

The mechanical properties are analysed in terms of relative density, microstructure, hardness and tensile properties.

6.2.1.1 Results of Relative Density and Microstructure Analysis

In Figure 6-5, the microscopy images of the density cubes from (a) PSD4_20-100 and (b) PSD5_20-125, built as witness specimens in the tensile build jobs, are shown. All specimens demonstrate comparable relative densities exceeding 99.5 %, with standard deviations below 0.08 %. Numerous pores, both circular and irregular in shape, are observed throughout the specimens.

In addition, multiple cracks are detected along the building direction, with length ranging from just a few micrometres to as large as 200 µm. The largest pores exhibit diameters up to approximately 70 µm.

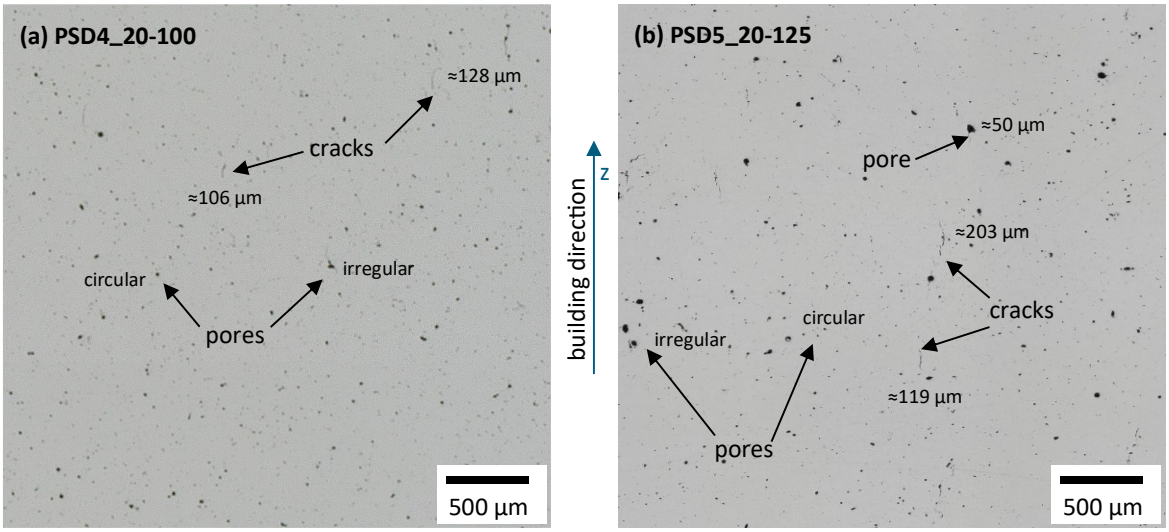

relative density 99.7 ± 0.08 %

relative density 99.5 ± 0.03 %

Figure 6-5: Microscopy images of polished density cubes in longitudinal section manufactured with (a) PSD4_20-100, and (b) PSD5_20-125.

In Figure 6-6, the reference microscopy image of LPBF_20-70 is presented. Compared to the images of the increased PSDs, more cracks are observed, with sizes reaching up to approximately 300 µm. The relative density of this specimen is 99.6 %, placing it between the values measured for the other two powders.

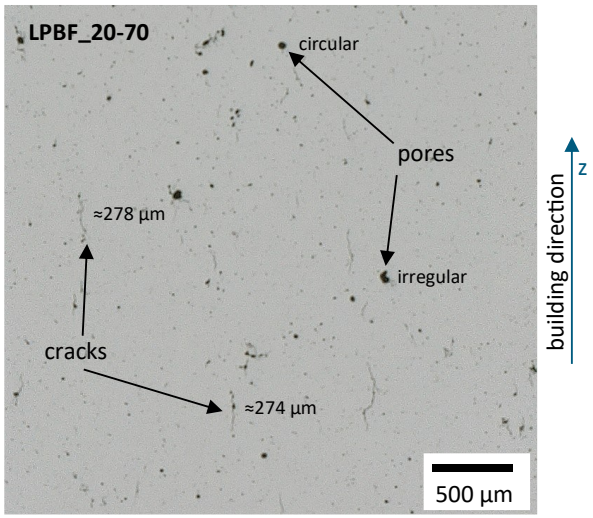

relative density 99.6 ± 0.02 %

Figure 6-6: Microscopy image of a polished density cube in longitudinal section manufactured with LPBF_20-70.

The SEM images of the three PSDs in Figure 6-7 reveal a similar microstructure. Fish scale patterns are observed, characterized by coarser, elongated grains within the fish scale and finer grains at melt pool boundaries. The grain growth is predominantly aligned with the build direction. Higher porosity is noted near the melt pool boundaries, with pores measuring between 5 and 10 µm. The images of PSD4_20-100 show a lower contrast compared to the other two specimens. In all samples, both pores and cracks are visible. The cracks are elongated and propagate in multiple directions along grain boundaries and melt pool boundaries, with lengths extending across multiple melt pool regions.

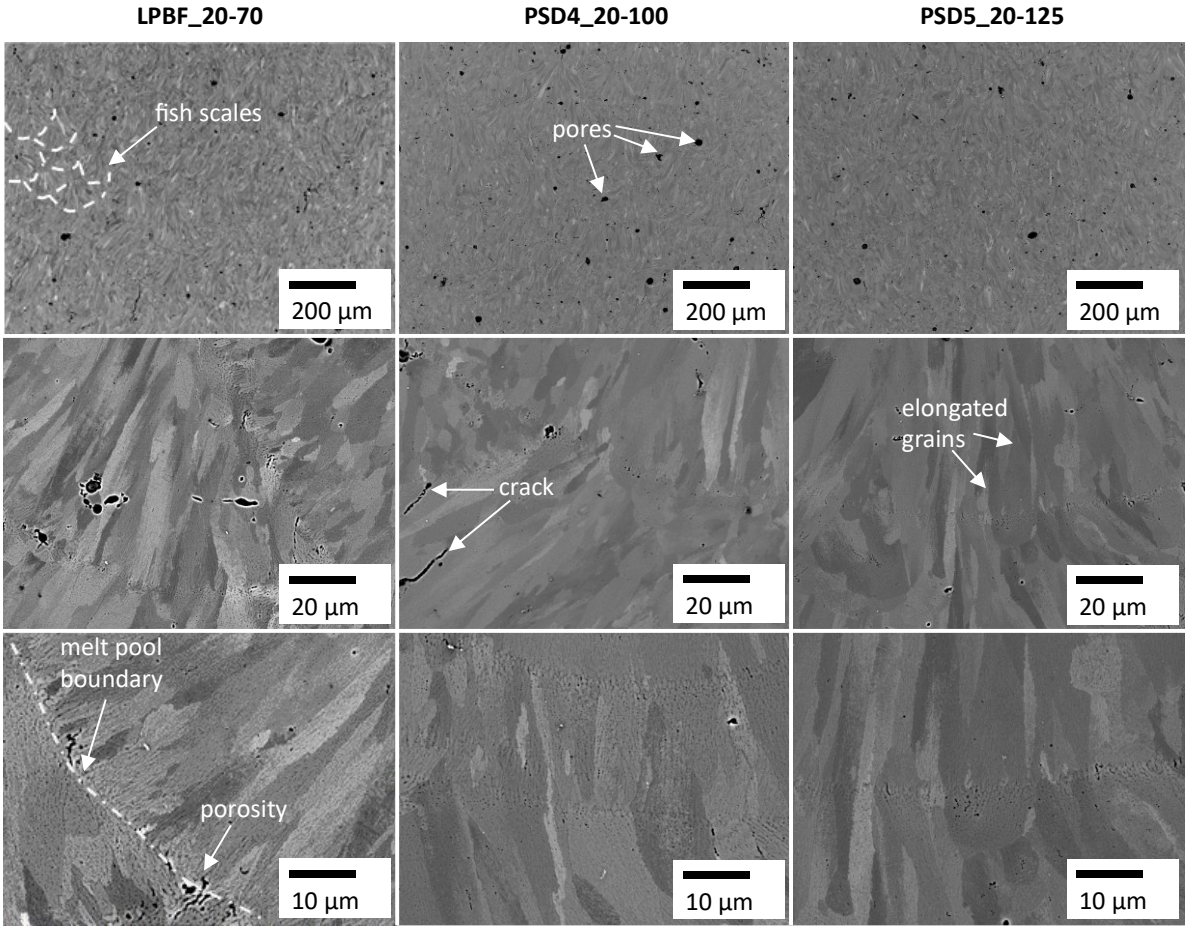

Figure 6-7: SEM images of AlMg11 polished density cubes in longitudinal section for microstructure analysis.

6.2.1.2 Discussion of Relative Density & Microstructure Analysis

The different pore geometries indicate distinct mechanisms of pore generation. Circular pores, commonly classified as gas pores, are in particular prevalent in aluminium alloys and arise from moisture or dissolved hydrogen, as stated in VDI 3405 sheet 2.8 [174]. Schmidtke describes how deep penetration welding, caused by excessive energy input, forms keyholes that trap gas, leading to pore formation [175]. Kimura et al. report a decrease in density from 99.9 % to 99.4 % with increasing Mg content in an Al-Si alloy from 0 to 2.5 wt.-% [176]. This is attributed to the formation of more gas pores, caused by the evaporation of Mg, which features a relatively low boiling point of 1110 °C compared to 2470 °C for Al [177]. Irregularly shaped pores result from insufficient particle melting, classifying them as lack-of-fusion pores [175]. However, the SEM images reveal that all particles are fully melted, suggesting that the process parameters are not properly balanced for defect free build up. Most pores are located near to melting pool boundaries, indicating solidification or composition issues. Zhao et al. propose that pores are trapped at the solidification front due to instabilities at the keyhole tip [178].

Tabatabaei et al. identified melt pool boundaries in AlSi10Mg specimens prone to cracking due to chemical composition issues and increased strain at the boundaries [179]. Similarly, cracks are visible in AlMg11 specimens along the building direction, with SEM-images showing cracks orthogonal to it as well. Some specimens exhibit more cracks than others, with cracks lengths extending up to three melt pools, indicating inconsistent results. VDI 3405 sheet 2.8 lists inappropriate temperature distribution, chemical composition issues, overheating or incomplete melting of the particles as potential causes [174]. These cracks are either hot or stress related. The presence of multiple types of defects indicates that the overall process parameter-powder interaction is inadequate. Despite achieving relative densities above the processability threshold of 99.5 %, the presence of pores and cracks is likely to degrade mechanical properties. Further process parameter tests are necessary to improve manufacturability.

The detected microstructure in the SEM images resembles that observed in other aluminium alloys, such as the aluminium-scandium alloy studied by Kuo et al. [180]. Since similar microstructures are formed under the same process parameters, no influence of the increased PSD on microstructure formation is identified.

In conclusion: Multiple types of detects, including gas pores, lack-of-fusion pores and cracks, are identified across all three PSDs. Given the similarity in microstructure and defect formation, no significant influence of increased PSD is identified. Further process parameter investigations are required to achieve defect free build-up.

6.2.1.3 Results of Hardness Analysis

The specimens exhibit similar Vickers hardness values, as demonstrated in Figure 6-8. Due to the simplicity of the hardness measurement, all AlMg11-PSD variations are tested. For each powder, the density cube, build using the same reference process parameter, is analysed.

The hardness specified by the powder supplier is indicated by the green bar, which ranges from 110 to 115 HV10. The mean values for all specimens fall between 112 and 114 HV10 with standard deviations ranging from 1.14 to 2.7 HV10 and therefore meet the reference hardness of 110-115 HV10. Among the powders, PSD2_45-70 achieves slightly higher hardness values, while LPBF_20-70 shows slightly lower values.

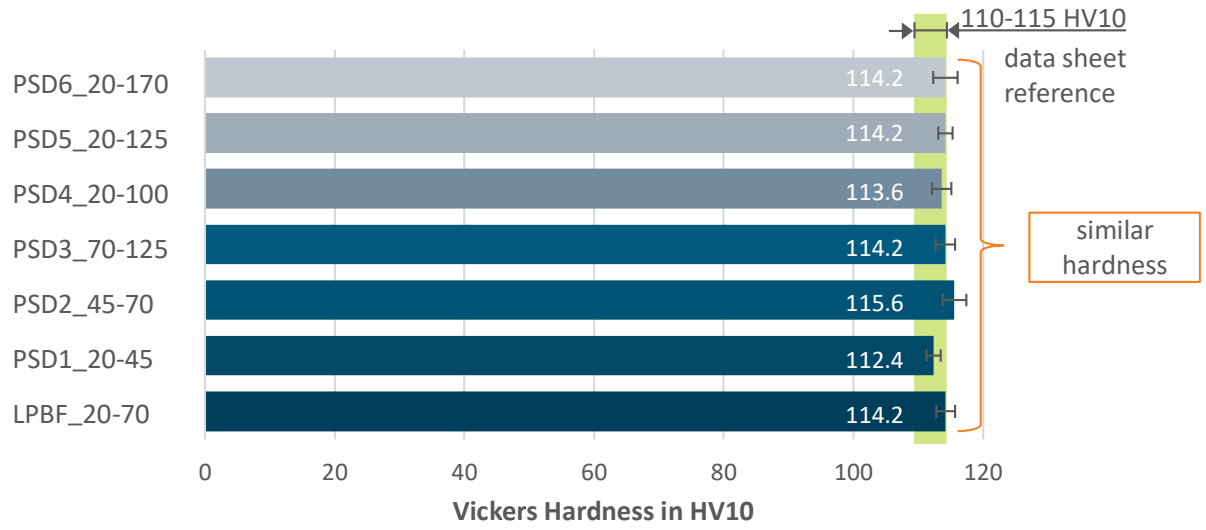

Figure 6-8: Bar chart of the measured Vickers hardness HV10 for AlMg11 powders compared to data sheet reference.

6.2.1.4 Discussion of Hardness Analysis

The aluminium alloy AlMg11 hardens through three main mechanisms: solid solution hardening, precipitation hardening, and grain hardening described by Roos et al. [37]. Magnesium in AlMg11 contributes to solid solution hardening by causing lattice distortion, which reduces dislocation mobility while maintaining ductility. A precipitation hardening cannot be confirmed based on the SEM images. In LPBF, full particle melting ensures the dissolution of alloying elements, while the high cooling rates largely prevent diffusion, and no precipitates are formed, forming a supersaturated solid solution. According to Bhattiprolu et al., grain hardening is influenced by cooling rates, where higher cooling rates produce smaller grain sizes, leading to increased hardness [181]. Since the same process parameters are applied to melt the particles fully, cooling rates remained consistent, resulting in uniform hardness values across all AlMg11 PSDs. Other powder characteristics, such as flowability, do not seem to affect hardness.

Although solid solution strengthening primarily determines the alloy's strength, precipitation and grain refinement offer supplementary contributions [37]. This combination of mechanisms explains the consistent hardness results observed across all PSDs. The hardness values for all PSDs fall within the target range specified for AlMg11.

In conclusion: All PSDs meet the reference data sheet values within a range of 112 to 115 HV10. No influence of PSD on hardness is identified.

6.2.1.5 Results of Tensile Tests

The yield strength $R_{p0.2}$, tensile strength R_m and elongation at break A are determined through tensile tests. In Figure 6-9, the results for the as-built specimens with varying properties across the orientations 0°, 45° and 90° are shown. PSD4_20-100 consistently achieves the highest yield strength in all orientations ranging between 229 and 235 N/mm², while PSD5_20-125 exhibits the highest tensile strength at 0° with 406 N/mm², but lower values of 340 N/mm² and 297 N/mm² at 45° and respective 90°. Maximum elongation varies, with PSD5_20-125 reaching the highest at 0° (23.2 % ± 1.26), PSD4_20-100 at 45° (15.5 % ± 1.0) and LPBF_20-70 at 90° (12.4 % ± 3.68).

The results also show mixed anisotropy trends. LPBF_20-70 exhibits slight anisotropy in tensile strength and elongation, with deviations of 1.1 % and 1.8 %, and a larger 11.6 % variation in yield strength across build orientations. For PSD4_20-100, this pattern is nearly reversed, with a small 1.1 % deviation in yield strength, 5.1 % for tensile strength, and 15 % for elongation. PSD5 _20-125 displays higher anisotropy, with deviations ranging between 8.2 % for yield strength and 37.8 % for elongation.

When compared to the reference data sheet values, no consistent trend is observed in relation to PSD or orientation. The results vary, with some values falling within and others outside the data sheet specifications [9]. Only PSD4_20-100 in the 45° build orientation meets all the data sheet values.

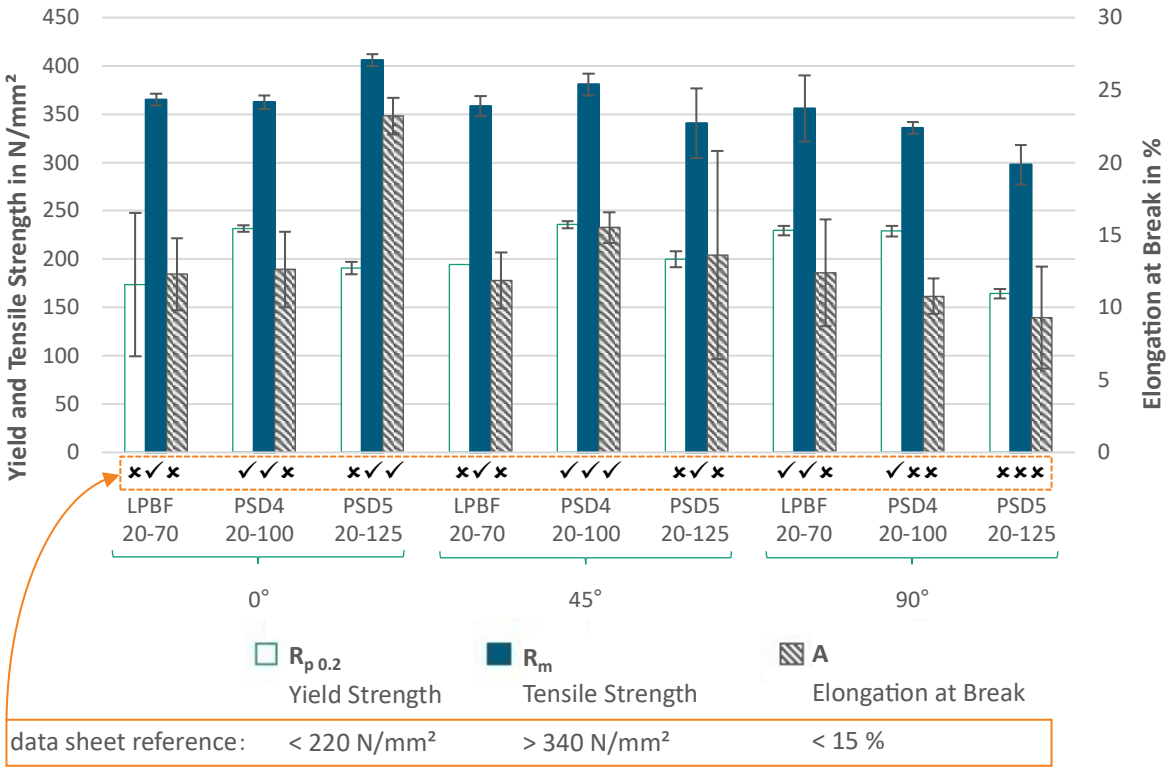

Figure 6-9: Diagram of the measured tensile properties in a 0°, 45° and 90° orientation for AlMg11 powders.

6.2.1.6 Discussion of Tensile Tests

The tensile test results for the as-built specimens reveal significant variation in mechanical properties across the tested orientations (0°, 45°, and 90°). PSD4_20-100 consistently exhibits the highest yield strength across all orientations, ranging from 229 to 235 N/mm². For LPBF_20-70, a trend emerges where higher or maintained yield strength are observed with increasing layers, particularly in the 90° orientation. In contrast, PSD5_20-125 shows a decline in yield strength as the number of layers increases. PSD4_20-100 demonstrates increased results at 45° and decreased values at 90°, with no clear progression linked to the number of layers.

Maconachie et al. investigate the influence of build orientation on tensile properties for AlSi10Mg and observe that while yield and tensile strength exhibited negelective anisotropy, ductility decreased from 6.7 % horizontally to 5 % vertically [182]. Fractures are initiated along the orientation of the melt pool boundaries, underscoring the dependence on build direction. Increased porosity and multiple cracks along the melt pool boundaries are identified in the AlMg11 specimens, which likely contributed

to fracture initiation. The visible cracks across multiple melt pools in various directions suggests that using the reference process parameter does not ensure a stable process. These defects are likely to affect mechanical properties, increasing standard deviations and reducing reproducibility.

The highest densities in the PSD4_20-100 and PSD5_20-125 specimens are achieved at scanning speeds of 845 mm/s, 965 mm/s, corresponding to VEDs of 77.7 and 88.7 J/mm³. In comparison, the reference process parameter used to manufacture the AlMg11 tensile specimens results in a VED of 63.8 J/mm³. Adjusting the process parameters to achieve a VED above 63.8 J/mm³, while reducing scanning speed to mitigate melt pool turbulences, appears promising for enabling a robust AlMg11-LPBF process. The higher yield strength of PSD4_20-100 aligns with the broader process window obtained by varying scanning speeds, suggesting an upper limit of PSD when using reference process parameters.

Across all PSDs, a trend of lower tensile properties in the 90° orientation is observed, which is attributed to an accumulation of defects as more layers are added. The anisotropy in mechanical properties is likely caused by variations in the thermal history of the part [33]. The higher heat storage in the lower layers, because of the larger scanning areas, may benefit larger particles such as PSD5_20-125, whereas the reduced heat input and storage in the upper layers is advantageous for smaller PSDs like LPBF_20-70.

Singh et al. further state that in 0° and 90°-oriented components, the deposition of a new layer over a previously solidified metallic layer results in high heat dissipation due to the high thermal conductivity of a metal part compared to powder. The greater thermal gradient between the newly solidified layer and the previous layer leads to increased residual stress. Residual stress is also influenced by component height and the presence of defects like pores and cracks. In the 90°-oriented components, where the number of layers is higher, residual stress and the number of pores increase compared to other build orientations. [183]

In conclusion: The multiple defects observed lead to tensile properties with significant deviations, without establishing a clear trend regarding the influence of PSD on these properties. Anisotropy is identified for all three PSDs, and reference data sheet values are only partially achieved.

6.2.2 Correlation Analysis

A correlation analysis is performed for the six PSD variations PSD1-PSD6 and the reference LPBF_20-70 to statistically assess relationships. The results are presented and discussed in the following.

6.2.2.1 Results of Correlation Analysis

The correlation matrix for AlMg11 is shown in Figure 6-10, revealing several notable correlations. Decile values (D10, D50, D90) and particle size span exhibit a negative correlation with the cohesion index at multiple rotational speeds. The avalanche angles show mixed correlations (positive, negative, and insignificant) across the data set, with low significance in all cases. Apparent and tapped densities present a similar pattern, with the Hausner ratio negatively correlating with particle sizes. Additionally, the particle size span and D10 correlate negatively with tapped density, while D10, D50, and symmetry present a negative correlation with Hausner ratio. Tapped density correlates positively with part density. Particle shape characteristics negatively correlate with hardness but seem to positively correlate with flowability results, though these correlations are weak. The correlations for the avalanche angle

at 35 rpm show a reversed trend compared to the other rotational speeds. The correlation between flowability characteristics and mechanical properties does not show any clear trends.

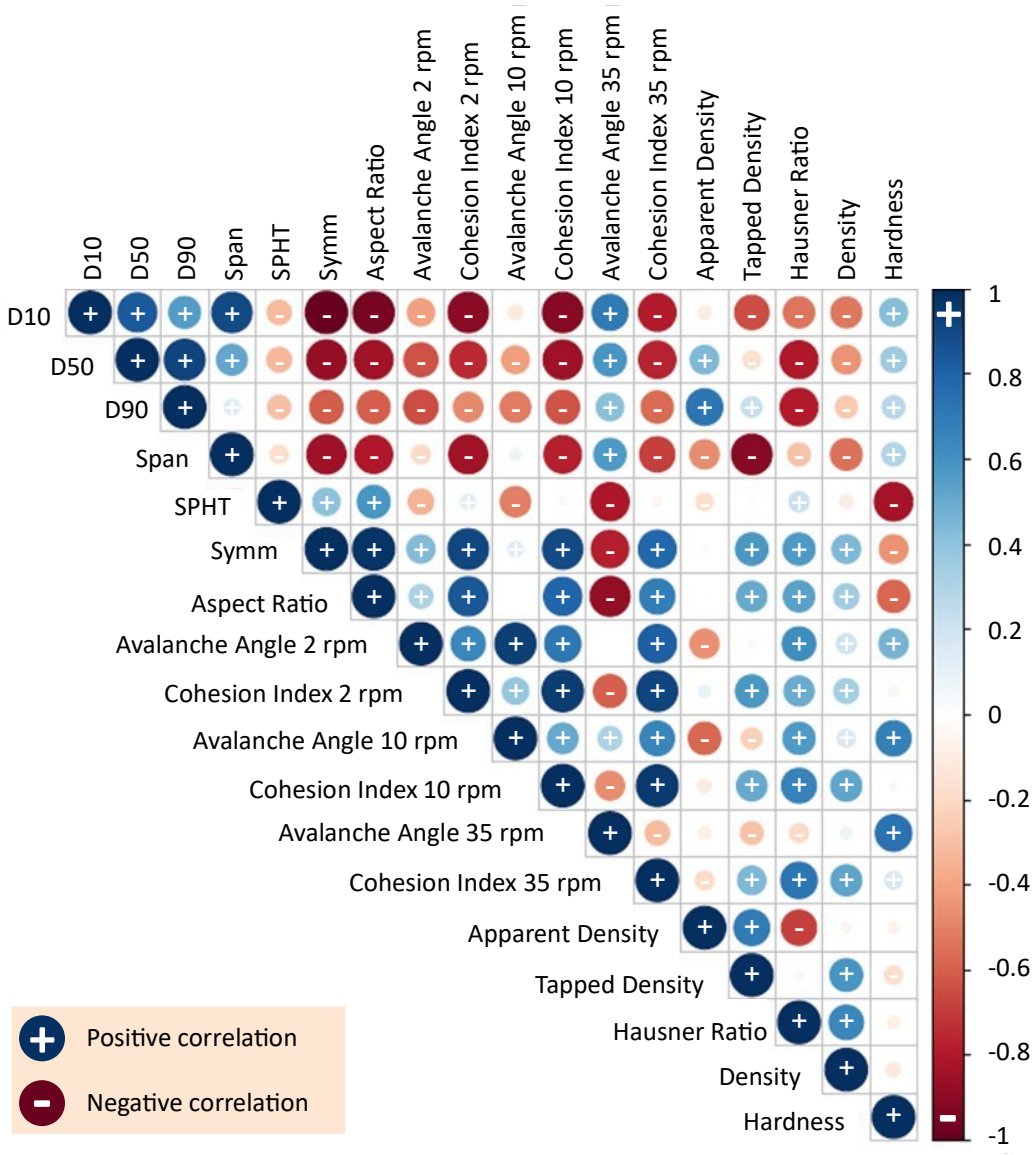

Figure 6-10: Correlation matrix based on Pearson coefficient of AlMg11 results.

The correlation matrix is generated for all PSDs. While the tensile test results are only performed for the selected PSDs, PSD4, PSD5, and LPBF, summarizing their results from different orientations does not yield sufficiently significant trends for mechanical properties.

6.2.2.2 Discussion of Correlation Analysis

The aim of this discussion is to identify causal relationships and distinguish correlations that may lack a direct logical basis.

1. Flowability

The results from the correlation analysis confirm a slight trend for higher tapped densities with broader PSDs. As supported by Marchetti and Hulme, mixing small and large particles enhances tapped density due to smaller particles filling the voids between larger ones, leading to denser powder packing. This

aligns with the AlMg11 funnel tests, where the widest distributions (PSD5_20-125 and PSD6_20-170) exhibited the highest tapped densities [108]. This is further corroborated by Li et al. [8], who observe that larger particles alone (approximately 53 µm) result in lower tapped densities, emphasizing the value of a wide PSD. For apparent density, the trend is similar but less pronounced. Although the correlation analysis hints at these relationships, the causality is primarily rooted in how particle size distributions influence packing efficiency.

The correlation between particle size and Hausner ratios is clearer. Larger particles tend to show lower Hausner ratios, which indicates lower compactibility, consistent with the correlation analysis results. The wider PSDs, particularly PSD4_20-100 and PSD5_20-125, improve flowability by reducing cohesion indices and avalanche angles at lower rotational speeds (up to 25 rpm). These factors, influence the effectiveness of powder spreading during recoating, particularly for PSDs larger than the layer thickness. While the results support this trend, further investigation into PSD would provide more clarity on the causal relationship between flowability and PSD during processing.

2. Relative Density

Decile values and particle size span correlate negatively with relative density. This trend is only partially supported by a detailed analysis of the measured results. Although the overall trend may hold true for particle sizes up to 170 µm, these investigations demonstrate comparable processability and manufacturability for PSDs with upper limits of 100 µm and 125 µm to the reference PSD of 20-70 µm. A detailed analysis of the three PSDs used in the tensile tests shows reversed results, indicating a positive correlation between decile values and relative density. This underscores a limit in PSD of 125 µm for enhanced mechanical properties when using these LPBF settings. Higher avalanche angles and cohesion indices correlate with increased density; however, this relationship is overall of limited validity of causal relationships in this context.

3. Vickers Hardness

A significant negative correlation (r_C = -0.905) is identified between particle sphericity and hardness. While this suggests that less spherical particles may result in higher hardness, the practical significance of this correlation is low due to the similar values across the powders. The relative densities of the cubes are comparable, suggesting that minor relative density variations do not lead to substantial changes in hardness. Therefore, the correlation between particle shape and hardness lacks a strong causal basis.

The negative correlation between avalanche angle and hardness also does not imply a clear trend. Given the slight negative correlation between the cohesion index and relative density, there is insufficient evidence to establish a direct link between powder morphology and hardness.

In conclusion: Multiple correlations are mathematically identified. Causal attribution indicates that increased particle sizes enhance flowability, suggesting a positive influence of larger particles on the material's ability to flow during processing.

6.2.3 Key Findings on Manufacturability

In this section, the manufacturability of increased PSDs, PSD4_20-100 and PSD5_20-125, is investigated, covering the mechanical properties based on relative density, microstructure, hardness and tensile properties. Because of the low information level identified for AlMg11-mechanical properties, the values of the material data sheet are used as target values.

The relative densities align with data sheet specifications, though pores and cracks are observed across all PSDs, with no clear link to increased PSD, but potential solidification and composition issues are noted. Hardness values remain consistent, while tensile properties slightly decrease with increased layer counts, likely due to heat storage effects. Process parameter adjustments are anticipated to stabilize the process and improve mechanical properties. The Key findings are summarized in Table 6-3.

Table 6-3: Key findings of the investigations on AlMg11 manufacturability.

Criteria	Result AlMg11
relative density and microstructure	• Similar defect formation: Multiple defects identified: gas and lack of fusion pores, cracks • Similar relative density (>99.5 %) meet reference data sheet • similar microstructure identified using same process parameters • No influence of PSD identified
Vickers hardness	• Similar Vickers hardness for all AlMg11-PSDs within 112 – 115 HV10 • Data sheet reference of 110-115 HV10 is met • No influence of PSD identified
tensile properties	• No clear trend across PSDs and specimens' orientations • Anisotropy identified for LPBF20-70; PSD4_20-100 and PSD5_20-125 • Reference data sheet values partially met
correlation analysis	• Multiple correlations are mathematically identified • Causal attribution: Increased particle sizes enhance flowability

The research question "How do the different PSDs affect the mechanical properties of the manufactured parts?" is answered for AlMg11 as follows: Increased PSDs exhibit no discernible effect on relative density, hardness, microstructure, and tensile specimens, printed using the same process parameters. The PSD4_20-100 exhibits slightly higher values compared to PSD5_20-125 and is comparable to LPBF_20-70. The presence of multiple defects in the specimens indicates the need for further process parameter adaptations.

AlMg11, as an alloy, specifically atomized for LPBF, demonstrates potential for resource and cost savings by increasing atomization yield, thereby reducing the quantity of unused particles. For further investigations, the high-cost powder Ti-6Al-4V recognized for its stable LPBF processability is selected.

7 Processability and Manufacturability of varied PSDs using Ti-6Al-4V

The processability of Ti-6Al-4V is assessed through flowability measurements and process parameter adaptions for each PSD to achieve relative densities above 99.9 %. For manufacturability investigations, the adapted process parameters are used to produce the specimens. This approach allows for comparability of the achieved mechanical properties across different PSDs with reference values from industry.

7.1 Processability

In the following sections, the results of the processability analysis are presented and discussed.

7.1.1 Flowability

The influence of the PSD variation on the flowability as one indicator for the processability is analysed. Distinct stresses are applied to the powder with multiple tests using the Hall funnel and the rotating drum.

7.1.1.1 Results of Flowability Analysis using the Hall Funnel

The flowability of the three Ti-6Al-4V powders, assessed using the Hall funnel, is presented in Table 7-1. The Ti64_20-100 powder exhibits the same apparent density as the LPBF_20-53 powder with a higher tapped density, resulting in a higher Hausner-ratio of 1.13 for Ti64_20-100. The Hall flowability of EBM_45-106 is measured at 25.2 s/50g, surpassing that of the other two powders, while LPBF_20-53 does not flow freely and requires additional tapping. Ti64_20-100 demonstrates the fastest Hall flowability.

When compared to industry reference values in Table 4-5, the apparent density and Hall flowability of the powders are consistent with these benchmarks. The industry tapped densities range from 2.84 to 2.92 g/cm³, which is higher than the measured range of 2.53 to 2.77 g/cm³. Consequently, the resulting Hausner ratios for the investigated powders, between 1.09-1.13, are comparatively lower than industry references, which range from 1.20 to 1.24.

Table 7-1: Ti-6Al-4V results of apparent and tapped density, Hausner ratio and Hall flowability measurements.

Powder	Apparent Density in [g/cm³]	Tapped Density in [g/cm³]	*Hausner Ratio* [-]	Hall Flowability in [s/50g]
LPBF_20-53	2.46 ± 0.00	2.68 ± 0.01	*1.09*	24.67 ±3.61*
Ti64_20-100	2.46 ± 0.01→	2.77 ± 0.01 ↑	*1.13* ↑	24.23 ± 0.15 ↓
EBM_45-106	2.30 ± 0.01 ↓	2.53 ± 0.01 ↓	*1.10* ↑	25.20 ± 0.20 ↑

* No free flow, residual powder in the funnel

7.1.1.2 Discussion of Flowability using the Hall Funnel

For the Ti64_20-100 and LPBF_20-53 powders, smaller particles appear to fill the voids between larger particles, resulting in higher apparent and tapped densities. Ti64_20-100 exhibits the highest tapped density and a Hausner ratio of 1.13, suggesting higher compactibility due to its wide PSD, similar to what is observed for AlMg11. In contrast, the EBM_45-106 powder, which lacks smaller particles, displays lower apparent and tapped densities. Despite expectations that the absence of small particles

would lead to improved Hall flowability due to reduced interparticle forces, EBM_45-106 shows a slower flow rate of 25.2 s/50g, contrary to predictions. The Hausner ratios for LPBF_20-53 and EBM_45-106 are classified as “excellent”, while Ti64_20-100 is rated as “good” according to Hausner's classification [140]. This indicates superior flowability for these powders compared to the industry reference values in Table 4-5, which are classified as “fair”.

A notable finding is the high standard deviation of 3.61 s/50g for the LPBF_20-53 powder, which is attributed to powder sticking in the funnel. Additional tapping is required to initiate flow, indicating its slower flowability, with a measured Hall flowability of 24.67 s/50g, making it the least free-flowing powder among those tested [137]. This aligns with literature findings, where interparticle forces from small particles hinder flow, even with the same sphericity as the other powders (**Table 3-5**). The flow behaviour of EBM_45-106, despite its larger particle size, does not follow the expected trend of increased flowability with particle size, as seen in studies by Xue et al. and Xiongfei et al. [7, 50]. It is expected that the missing small particles should increase the Hall-flowability of EBM_45-106 due to lower interparticle forces and a higher effect of gravity. The particle shape as an influencing factor is neglectable due to the similar sphericity of all three powders, as shown in Table 5-6 and Figure 5-9.

External factors, such as humidity, potentially influence flowability. Higher humidity levels in the atmosphere are known to increase particle cohesion, potentially affecting the results. The absolute humidity is recorded for each test day, with Ti64_20-100 measured at 8.13 g/cm³, EBM_45-106 at 10.29 g/cm³, and LPBF_20-53 at 11.49 g/cm³. This trend corresponds to the Hall flowability results, suggesting that with similar humidity levels, EBM_45-106 exhibits flowability closer to that of Ti64_20-100. Despite the lower humidity for Ti64_20-100, its larger particles seemed to improve flowability, supporting the idea that larger particles enhance flow.

In conclusion: The analysis of apparent and tapped densities reveals that achieving high densities necessitates the incorporation of small particles below 45 µm to effectively fill voids. The Hausner ratio analysis indicates that the LPBF_20-53 and EBM_45-106 powders fall within the “excellent” classification, while the Ti64_20-100 powder is classified as “good”, demonstrating overall similar performance. Furthermore, the Hall flowability assessment shows that a wide PSD of 20-100 µm results in the fastest Hall flowability.

7.1.1.3 Results of Flowability Analysis using the Rotating Drum

The avalanche angles and cohesion indices, for increasing rotational speeds, are presented in Figure 7-1 for all three Ti-6Al-4V powders. The curves progress similarly for all powders, with EBM_45-106 powder exhibiting higher values compared to the other two powders, which display nearly identical values. The LPBF_20-53 powder shows lower avalanche angles and cohesion indices at lower rotational speeds (2-10 rpm) compared to the Ti64_20-100 powder, which features the lowest values at speeds above 10 rpm.

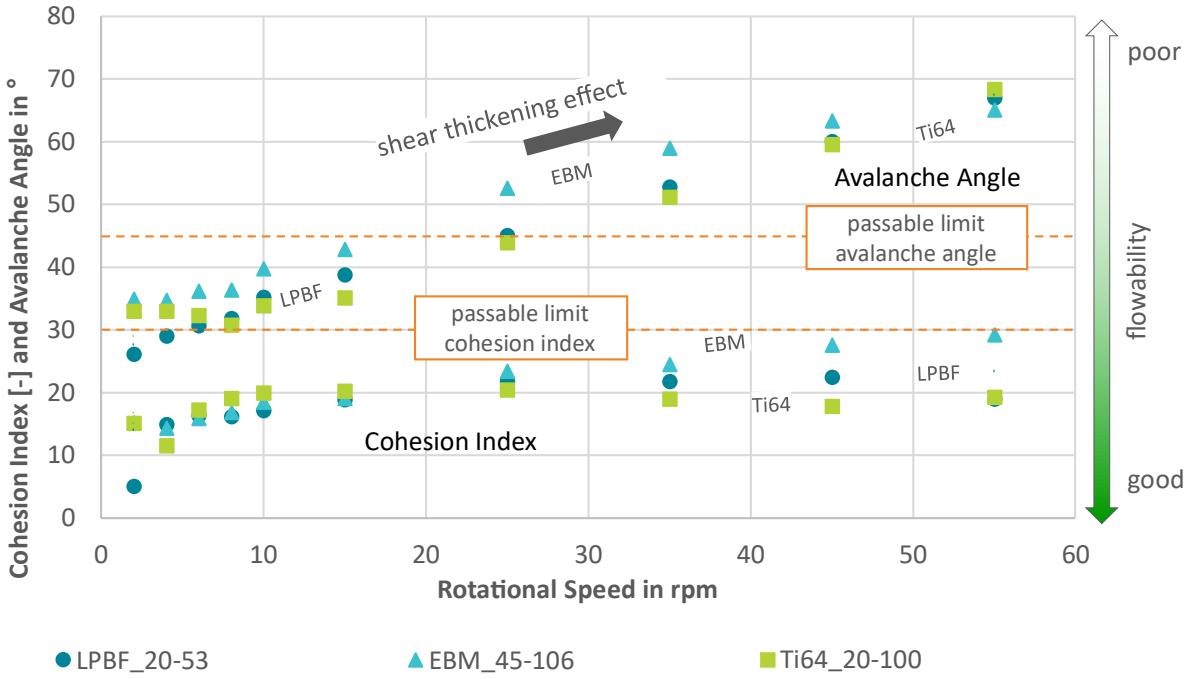

Figure 7-1: Diagram of the cohesion indices and avalanche angles across rotational speeds for three Ti-6Al-4V powders.

7.1.1.4 Discussion of Flowability using the Rotating Drum

The flowability measurements using the rotating drum method reveal shear thickening behaviour for all three powders, which seems to be a typical effect for LPBF powders and aligns with the AlMg11 results. The blended Ti64_20-100 exhibits enhanced flowability compared to the base powders LPBF_20-53 and EBM_45-106. As with AlMg11, the smaller particles below 45 µm fill in the voids between larger particles to smoothen the powder surface without suffering from increased interparticle forces, demonstrated by lower cohesion indices, particularly for rotational speeds above 10 rpm. This is an indication of higher processability of a wider distribution of 20-100 µm, compared to just large PSDs of 45-106 µm.

In conclusion: Particles smaller than 45 µm reduce the avalanche angle. All PSD show a shear thickening effect, though a wide span of 55 µm as in Ti64_20-100, maintains the cohesion indices for rotational speeds above 10 rpm.

7.1.2 LPBF

To analyse the processability of the increased PSDs, the next step after assessing flowability is to investigate their effects on LPBF. The results are presented and discussed in the following sections.

7.1.2.1 Results of LPBF Analysis

In Table 7-2, an overview of the process parameters and the variation range are provided. Additionally, it displays the number of build jobs required to achieve the target relative density of 99.9 %.

The two bottom lines show the VED and build rate for the final process parameters used in manufacturing the mechanical specimens. The final process parameters for EBM_45-106 and Ti64_20-100 are identical, explaining the similarity in VED and build rate. These process parameters differ from those used for LPBF_20-53, specifically in featuring a 0.05 mm smaller hatch distance, a 10 W higher laser power, and 300 mm/s slower scanning speed.

Table 7-2: Ti-6Al-4V parameter variation and final volume energy densities and build rates for the investigated powders.

Parameter Variation	LPBF 20-53 µm	Ti64 20-100 µm	EBM 45-106 µm
Build Jobs	2x	1x	3x
Laser Power in [W]	290-310	300-320	280-360
Scanning Speed in [mm/s]	1100- 1300	1100-1400	1000-1500
Hatch Distance in [mm]	0.11-0.17	0.08-0.14	0.08-0.14
Final Volume Energy Density in [J/mm³]	36.13	47.62	47.62
Final Build Rate in [cm³/h]	30.89	24.19	24.19

In Figure 7-2, the relative densities achieved for each process parameter combination across VEDs, are displayed. All three powders are successfully processed into cubes with relative densities surpassing 99.9 %. The LPBF_20-53 powder generated the highest number of density cubes exceeding this processability limit. The blended Ti64_20-100 powder consistently reached relative densities above 99.9 % across a wide VED range from 30 to 60 J/mm³, although some process parameter variations lead to occasional drops. The EBM_46-106 powder also achieved relative densities above 99.9 %, but no distinct process window is identified.

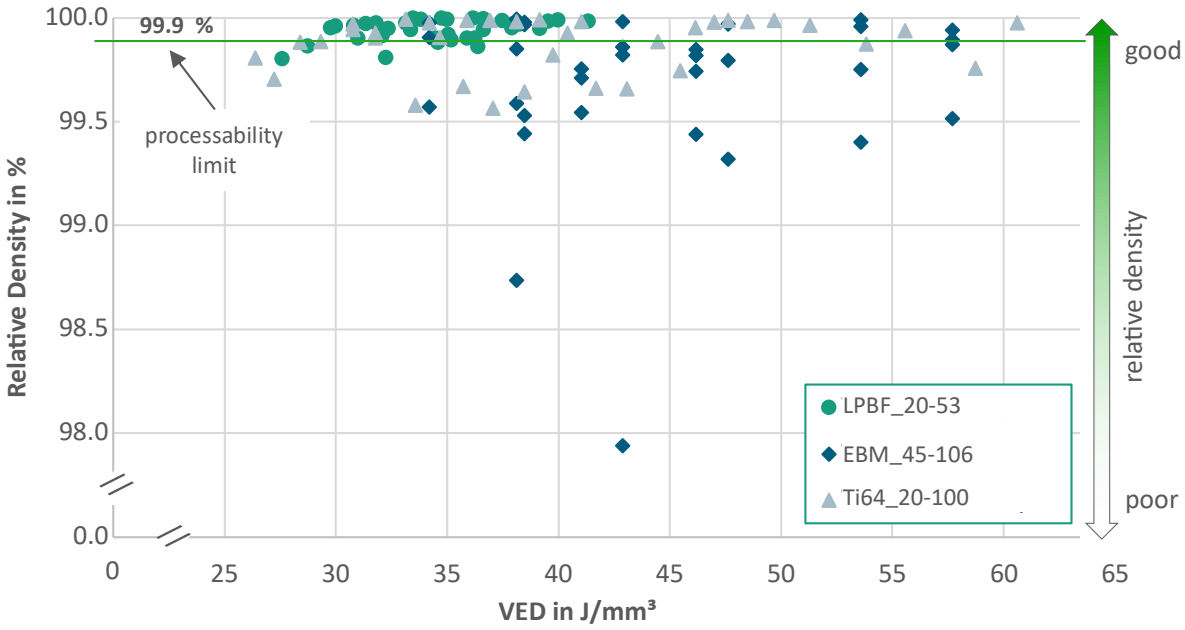

Figure 7-2: Diagram of the relative densities across VEDs for each LPBF parameter combination per Ti-6Al-4V PSD variation.

7.1.2.2 Discussion of LPBF Analysis

To investigate the processability of larger PSDs up to 106 µm for Ti-6Al-4V, the process parameters are adapted for each PSD. The LPBF_20-53 process parameters are used as a baseline for developing the process parameters for EBM_45-106 and Ti64_20-100 powders. For EBM_45-106, the adaptions are based on the approach for higher energy input to melt larger particles, as observed by Spurek et al. [107]. Both EBM_45-106 and Ti64_20-100 require higher VEDs to match the relative densities of LPBF_20-53. In detail, a smaller hatch distance increases the overlap of the scan vectors, while a slower scanning speed stabilizes the melt pool dynamics and reduces spatters as stated by Andani et al. [173].

The use of the same scanning speed as used for LPBF_20-53 results in excessive energy input, resulting in increased porosity.

The increase in laser power, although minimal, is unlikely to vaporize small particles. Instead, the combination of higher VED and remelting from vector overlap acts as a form of in situ heat treatment. To achieve relative densities similar to those of the LPBF_20-53 PSD, a balance of higher scanning speed, reduced hatch distance, and slightly increased laser power is necessary. Additional research is recommended to refine the process parameters. Overall, all three powders exhibited processability.

In conclusion: All three PSDs achieve 99.9 % relative density. EBM_45-106 and Ti64_20-100 require the same process parameters with a VED of 47.62 J/mm³ for manufacturing mechanical specimens. In contrast, LPBF_20-53 requires a lower VED of 36.13 J/mm³.

7.1.2.3 Results of Powder Application Test

The application of the Ti64_20-100 powder is tested, serving as the entire investigated PSD range of 20–100 µm. The results are presented in a bar chart in Figure 7-3. A slight decrease of approximately 1–5 µm is observed in the D10, D50, and D90 values for samples collected at the supply compared to those taken from the build plate. The samples from the overflow show a coarsening of 1 µm for D50 relative to the build plate samples. For D90, the overflow samples exhibit a coarsening of 5 µm compared to the supply samples and 8 µm compared to the build plate samples. D10 continues to decline in the overflow samples. The D90 value of 76.97 µm on the build plate indicates that 10 % of the particles exceed this size. A more detailed size-class analysis reveals that 1 % of the particles range between 90 and 100 µm.

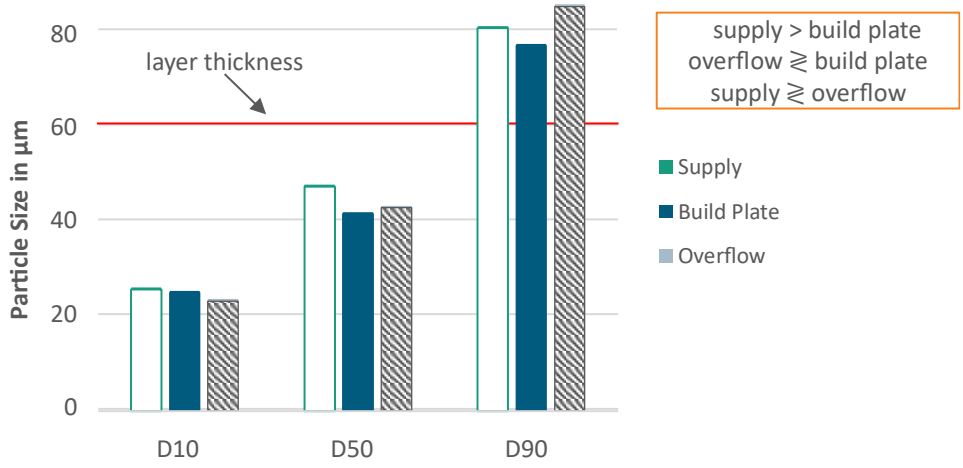

Figure 7-3: Bar chart of the particle size from the supply, build plate, and overflow measured for Ti64_20-100.

7.1.2.4 Discussion of Powder Application Test

The application test reveals a slight decrease in particle size on the build plate, indicating that smaller particles (≤20 µm) are removed by the gas stream during recoating and printing. Larger particles (≥75 µm) segregate in front of the recoating blade, refining the PSD, as suggested by simulations from Lee et al. [171]. They identify a coarsening from 15 % to 25 % for 22 µm particles by increasing the scanning speed from 254 mm/s to 1270 mm/s. This segregation effect likely prevents the larger particles from being fully deposited onto the build platform, causing them to be pushed in the overflow. However, the application of particles up to 100 µm is still demonstrated. The coarsening observed in

the overflow could also be influenced by spatters and the reduction in D10, consistent with Cordova et al.'s findings on powder re-use [76].

In conclusion: A decrease in particle size on the build plate compared to the particle size in the supply and overflow is observed. The application of powder with a D90 of 77 µm at a 60 µm layer thickness is feasible.

7.1.3 Key Findings on Processability

The research question “What is the effect of the PSD on processability?” is answered for the investigated Ti-6Al-4V powders as follows: The effect of increased PSD on processability for Ti-6Al-4V is a slight enhancement in flowability, particularly for the wider distribution in Ti64_20-100. Additionally, the phenomenon of shear thickening appears characteristic of LPBF powders, similar to that observed in AlMg11 powders. PSDs with particles up to 106 µm require an 11.5 J/mm³ higher VED, necessitating adaptations such as reduced hatch distances and increased scanning speeds to achieve comparable relative densities to LPBF_20-53. Notably, the adaption of process parameters is primarily defined by the largest particles. The adding of small particles (20-45 µm) does not require further adjustments to the process parameters. A subtle PSD refinement on the build plate due to segregation leads to a slight increase of the PSD in the overflow. In Table 7-3, the key findings are summarized.

Table 7-3: Key Findings of the investigations on the effect of Ti-6Al-4V PSDs on processability.

Criteria	Result Ti-6Al-4V
Flowability using Hall funnel	• Apparent and tapped density: For high densities, small particles below 45 µm required to fill voids • Hausner ratio: LPBF_20-53 and EBM_45-106 within Hausner classification “excellent” and Ti64_20-100 “good”, overall similar • Hall flowability: wide distribution 20-100 µm achieves fastest Hall flowability

Flowability using rotating drum	• Shear thickening effect for all investigated powders
	• Avalanche angle: particles <45 µm reduce results
	• Cohesion index: comparably lower cohesion achieved by
	  • < 10 rpm, base powders LPBF_20-53 and EBM_45-106 with spans below 40 µm
	  • > 10 rpm, blended Ti64_20-100 with span of 55 µm

LPBF	• Processability with 99.9 % relative density achieved by all three PSDs
	• Selected process parameters for manufacturing of mechanical specimens
	  • EBM_45-106 and Ti64_20-100 same process parameters with VED of 47.62 J/mm³
	  • LPBF_20-53 lower VED of 36.13 J/mm³

Application Test	• Decrease of particle size on build plate compared to particle size in supply and overflow • Application of powder with a D90 of 77 µm at 60 µm layer thickness

7.2 Manufacturability

With processability demonstrated, the identified process parameters are used to manufacture mechanical specimens. The next step is the investigation of the mechanical properties to assess the manufacturability of increased Ti-6Al-4V PSDs.

7.2.1 Mechanical Properties

In the following sections, the results of the analysis of relative density, microstructure, hardness and tensile properties are presented and discussed.

7.2.1.1 Results of Relative Density and Microstructure Analysis

In Figure 7-4, a representative density cube manufactured from each Ti-6Al-4V powder, serving as a witness specimen for the tensile tests, is displayed. The average relative density is provided for each density cube. All results demonstrate high reproducibility, displayed with standard deviations below 0.02 %. No cracks are detected, and only minimal porosity is observed.

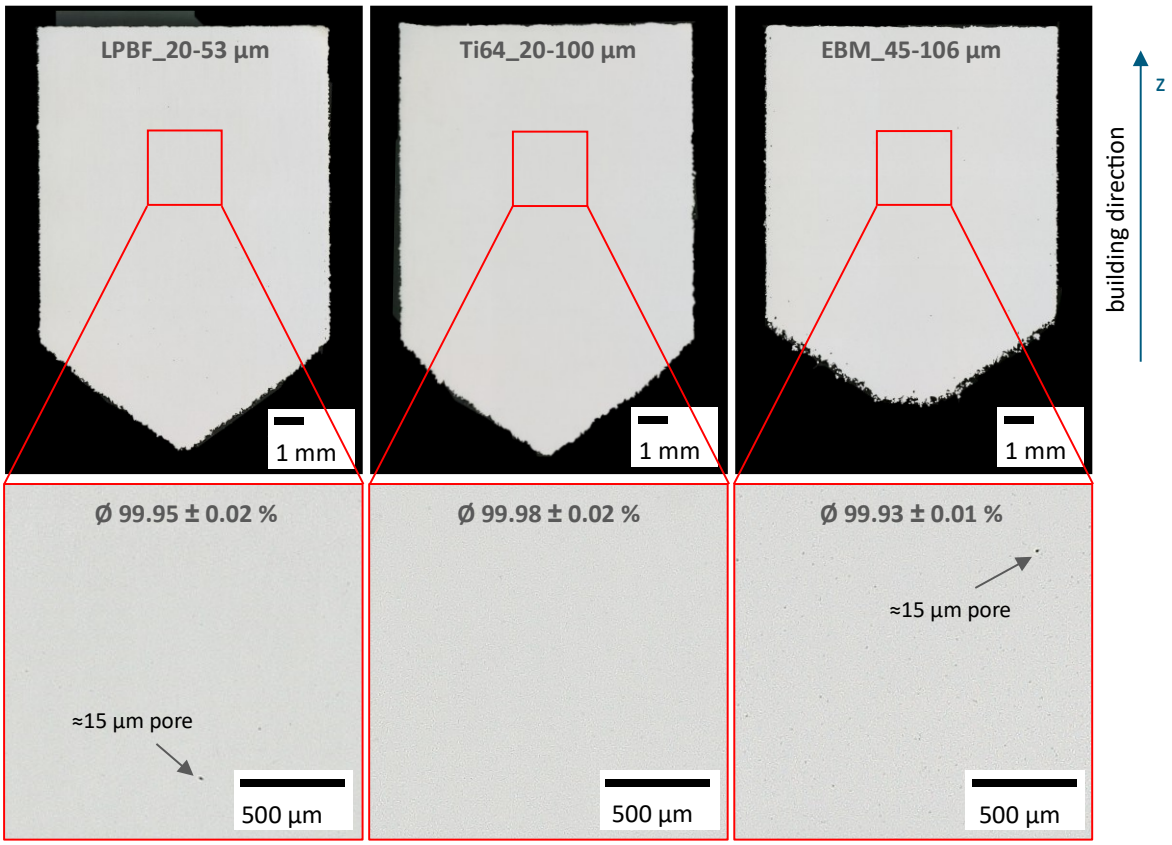

Figure 7-4: Microscope images of polished Ti-6Al-4V density cubes.

The microstructures of the three Ti-6Al-4V specimens are analysed exemplarily and presented in Figure 7-5. Similar columnar prior β-grain boundaries are revealed, partially filled with acicular α-structures. White β-bits are identified. The grains show no significant differences in size and length between the samples. The elongated grain growth in the build direction exceeds the 60 µm layer thickness and exhibits an approximate width of 50 µm. The EBM_45-106 specimen shows higher contrast and a distinct α-phase orientation. An angle of 45° is detected between the prior β-grain boundaries and the α-lamellae.

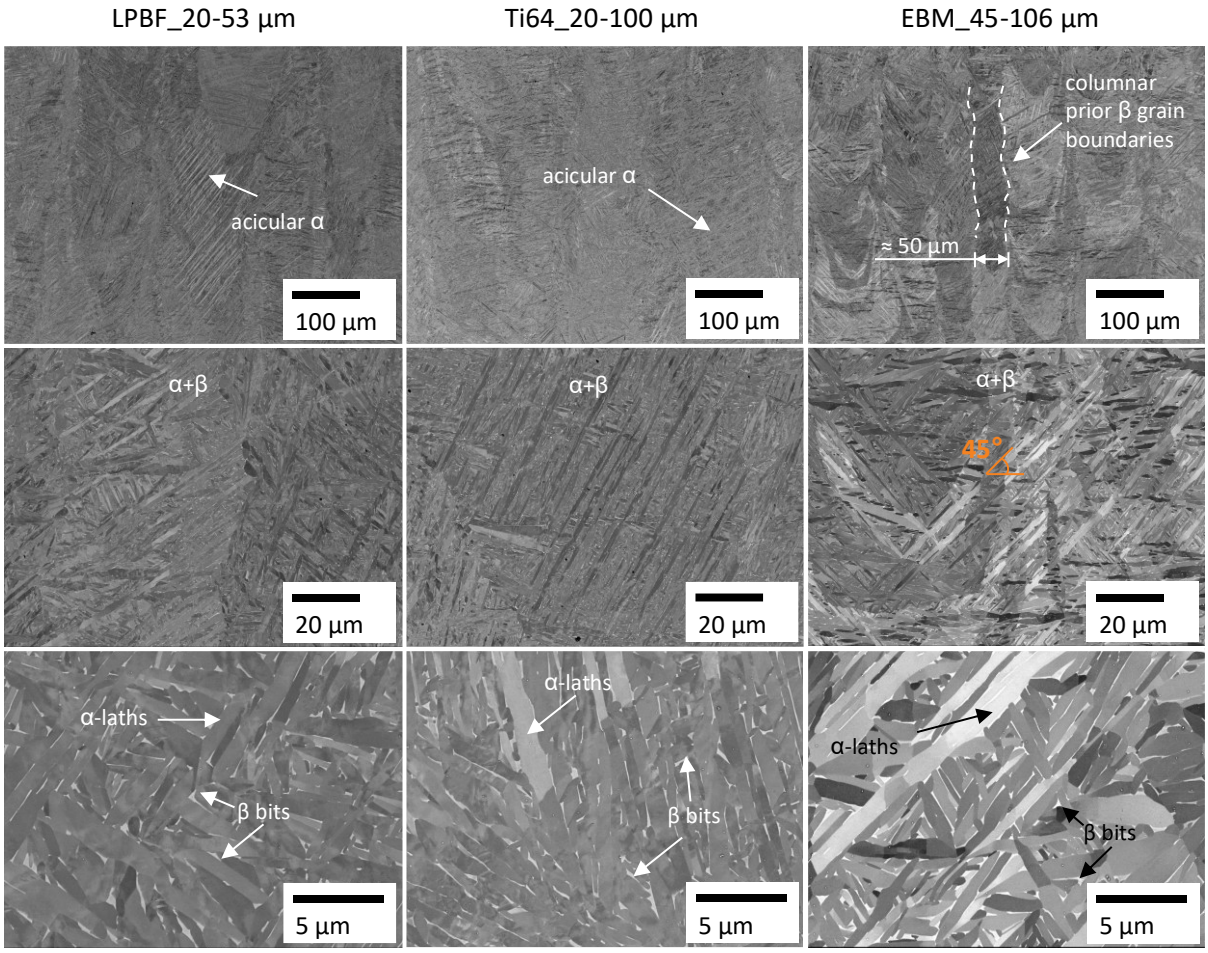

Figure 7-5: Exemplary SEM images for each investigated Ti-6Al-4V powder for microstructural analysis.

7.2.1.2 Discussion of Relative Density and Microstructure Analysis

All three powders consistently achieve relative densities above 99.93 %, meeting the industry reference target of 99.9 %. Although further comparison is limited by potential nanometre-level deviations due to measurement and process fluctuations, the successful adaptation of process parameter for each PSD results in high relative densities.

The microstructures exhibit similarities among the specimens, featuring an acicular α-structure with β-bits, a result of the heat treatment at 800 °C for 2 h. This aligns with findings of Zheng et al., who observed β-columnar growth enforced by a scanning pattern of 90°, consistent with these results [145]. The microstructures, acicular and lamellar α-phases, visible prior β-grain boundaries, and β-bits, are in accordance with the work of Zheng et al. and Cepeda et al. and typical for LPBF [145, 184]. The Burgers relationship, described by Zhang et al., suggests a 45° angle between the α- and prior β-phases, which may be visible in this study, though further validation is required [145]. Contrast variations in the EBM_45-106 specimen are attributed to differences in α-phase orientations and grinding imperfections, as reported by Thijs et al. [42]. A longer columnar prior β-grain growth due to the higher VED applied for Ti64_20-100 and EBM_45-106, as described by Cepeda et al., is not detected [184]. Overall, no significant influence of PSD or other powder characteristics on the microstructure is identified, indicating that the adapted process parameters result in comparable microstructures across PSDs ranging from 20–53 µm to 20–100 µm.

In conclusion: The similar relative densities (above 99.9 %) meet reference industry values. Despite different process parameters, a similar microstructure is identified. No influence of PSD is observed.

7.2.1.3 Results of Hardness Analysis

In Figure 7-6, the Vickers hardness values are presented for the three Ti-6Al-4V PSDs, manufactured using adapted process parameters. The green bar indicates the reference industry hardness values, as outlined in Table 3-4. Both EBM_45-106 and Ti64_20-100 exhibit similar hardness values, while LPBF_20-53 shows a slightly lower hardness at 322 HV10. LPBF_20-53 and Ti64_20-100 exhibit higher standard deviations of 7.4 and 9.7 HV10 respectively, while EBM_45-106 demonstrates higher consistency with a standard deviation of 2.5 HV10.

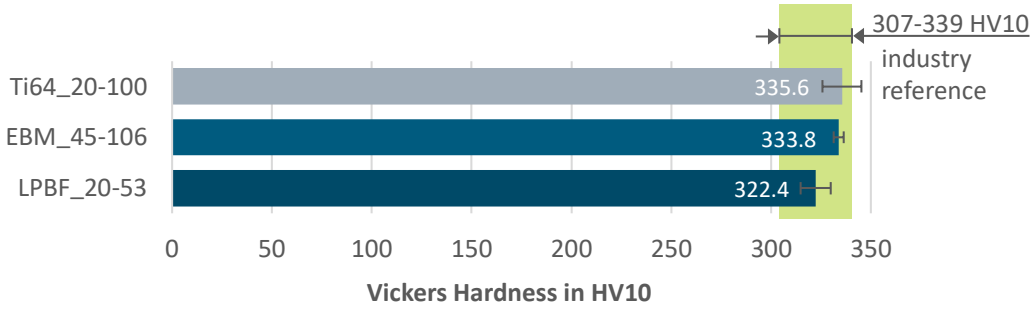

Figure 7-6: Bar chart of the measured Vickers hardness HV10 for Ti-6Al-4V powders compared to industry references.

7.2.1.4 Discussion of Hardness Analysis

The Vickers hardness results for all Ti-6Al-4V-powders fall within the reference industry range for Ti-6Al-4V produced with LPBF [58]. The standard deviations of LPBF_20-53 and Ti64_20-100, both below 3 %, are comparable to those observed in the AlMg11 hardness test. EBM_45-106 and Ti64_20-100 exhibit similar hardness values, due to the identical process parameters, resulting in similar VEDs and therefore cooling rates. The slightly lower hardness observed in LPBF_20-53 may be attributed to the lower VED used. Bhattiprolu et al. observe a correlation between reduced hardness and slower cooling rates [181]. However, in this case, no significant microstructural differences are detected.

In conclusion: The Vickers hardness for the large PSDs, EBM_45-106 and Ti64_20-100, is similar, ranging between 334 and 336 HV10, while LPBF_20-53 shows a slightly lower hardness at 322 HV10. The industry reference range of 307-339 HV10 is met for all powders. The difference in hardness is attributed to variations in process parameters.

7.2.1.5 Results of Tensile Tests

The tensile test results are presented in Figure 7-7, demonstrating that all three PSDs achieve tensile properties within the industry standard values listed in Table 3-4.

For the 0°-orientation, tensile and yield strength are comparable across all powders. LPBF_20-53 and Ti64_20-100 display similar elongation, both exceeding the elongation of EBM_45-106 by four percentage points.

In the 90°-orientation, the tensile strength for EBM_45-106 and Ti64_20-100 decreases by 31 and 48 N/mm², respectively. In contrast, LPBF_20-53 shows only a minor decrease in tensile strength (10 N/mm²), while its yield strength increases by 14 N/mm². Elongation increases for all powders by about 10 %, with LPBF_20-53 achieving values above 20 %.

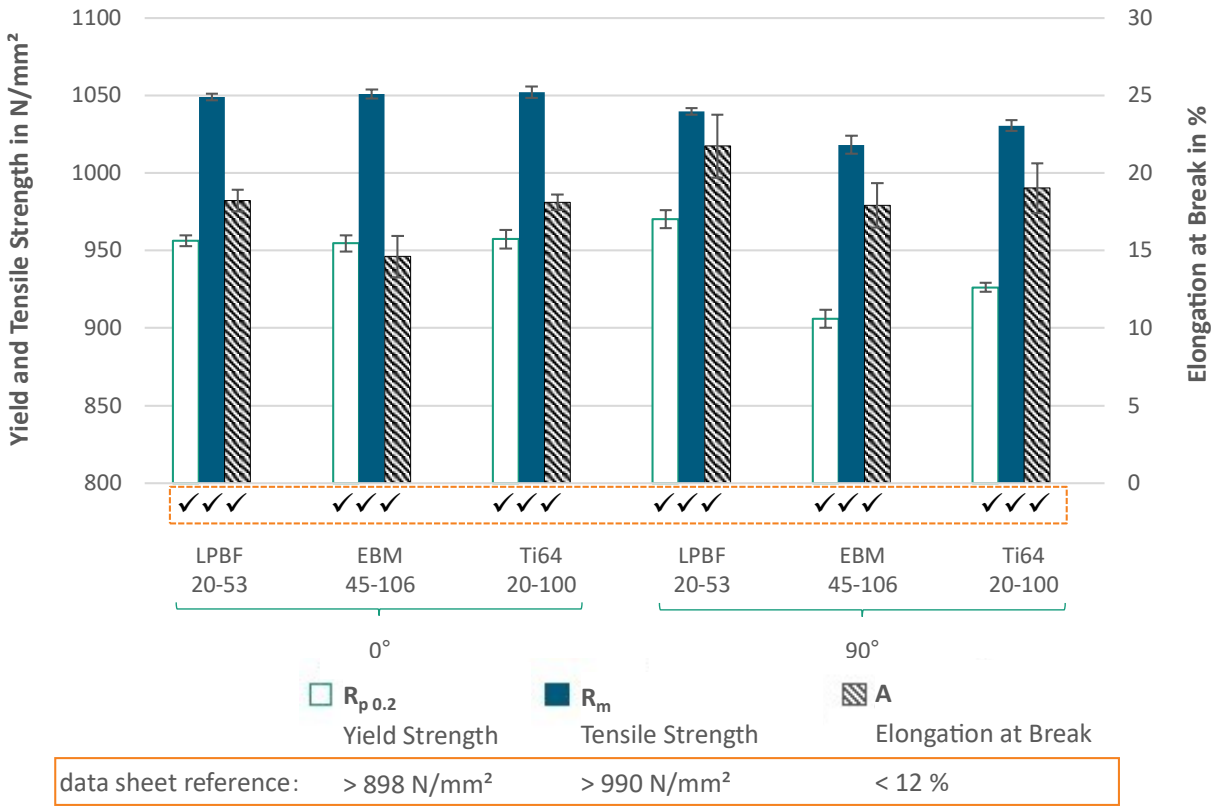

Figure 7-7: Diagram of the measured tensile properties in a 0° and 90° orientation for Ti-6Al-4V powders after heat treatment (800 °C for 2 h).

7.2.1.6 Discussion of Tensile Tests

The tensile specimens achieve values comparable to industry reference values (compare Table 3-4), meeting the target requirements. The adapted process parameters allow for evaluating the manufacturability of increased PSDs under conditions adapted for melting large particles, though this reduces direct comparability with standard powders. However, slight anisotropy is observed, with decreased tensile strength and increased ductility in the vertical orientation for all PSDs.

Several factors influence the mechanical properties, including build height, PSD, and process parameters. Lower build heights (e.g., 6 mm in the 0°-orientation) are less prone to defects compared to higher builds (e.g., 51 mm in the 90°-orientation), as reported by Singh et al. and Xue et al. [50, 183]. This results in consistent strength values in the 0°-orientation, with minor deviations in elongation. This effect is particularly noticeable for the two increased PSDs and slightly more pronounced for the specimens of the larger EBM_45-106 powder. Assuming higher energy input in the upper layers, it appears the upper energy limit required for these powders is already reached in higher layers. Yadroitsev et al. report no effect of heat treatment below the β-transus temperature ($T_{transus}$ = 1000±20 °C) on anisotropy [43]. Slight anisotropy persists even after annealing at 800 °C for 2 hours, indicating that further adjustments to process or heat-treatment parameters are required to achieve isotropy. Singh et al. demonstrate that residual stresses in as-built conditions are nearly eliminated by heat treatment of 800 °C for 1.5 h, though interlayer defects remain the primary cause of anisotropy after heat treatment [183]. This suggests that higher builds are more susceptible to defects due to the increased number of layers.

Another potential cause of anisotropy is the prior-β grain orientation, which aligns with the build direction in the 0°-orientation and with the test/loading axis in the 90°-orientation. This alignment allows

for easier slip along the prior-β grain boundaries at 90°, while the perpendicular 0°-orientation hinders dislocation slip [50, 183]. This could explain the higher ductility observed in all specimens at 90°, though the increase of only 4 % for Ti64_20-100, which remains almost consistent. This effect is also known to enhance tensile strength [50]. It is important to note that the tensile strength and yield strength only vary by 1-5 %, which is classified as negligible. Another influencing factor on anisotropy is the scan pattern. Singh et al. observe reduced anisotropy with a 67° scan variation, indicating that further investigation of the scan pattern potentially contribute to isotropy [183]. Additionally, the increased number of layers in the 90°-orientation may enhance heat dissipation, contributing to higher strength and ductility [184]. Larger particles, up to 106 µm, feature a lower specific surface area, which alters their melting behaviour compared to smaller particles (20–53 µm). This variation in melting requires compensation through adapted process parameters to ensure consistent performance. The microstructure analysis, using density cubes with a total height of 15 mm, shows no significant influence of increased PSDs. Investigating higher specimens (50 mm) may reveal deviations in microstructure that contribute to anisotropy and affect mechanical properties.

The elongation at break achieved by all three PSDs is noteworthy. EBM_45-106, despite exhibiting the lowest average elongation at break at 14.6 %, still exceeds the industry standard of 13.8 % (average value based on Table 3-4). LPBF_20-53 and Ti64_20-100 show even higher values, at 18.6 % and 20 %, respectively. These results indicate that the process parameters are adapted to enhance ductility rather than strength.

In conclusion: In the horizontal orientation, all PSDs exhibit similar yield and tensile strength. In the vertical orientation, LPBF_20-53 shows higher strength and ductility compared to the other powders. All results meet industry reference values.

7.2.2 Correlation Analysis

For statistical evaluation, a correlation analysis is performed. The results are presented and discussed in the following sections.

7.2.2.1 Results of Correlation Analysis

The correlation analysis for the Ti-6Al-4V-results is presented in an upper-half correlation matrix in Figure 7-8. Positive correlations are observed between the D10, D50, and D90 deciles and both the avalanche angles and cohesion indices. Conversely, negative correlations are detected with apparent and tapped densities, as well as with tensile properties. A more regular particle shape appears to reduce the avalanche angle and cohesion index, while increasing apparent and tapped densities, along with the tensile properties.

Higher avalanche angles and cohesion indices are associated with decreased relative density, which in turn reduces tensile properties. Increased relative density correlates positively with tensile properties, while hardness correlates negatively with tensile properties.

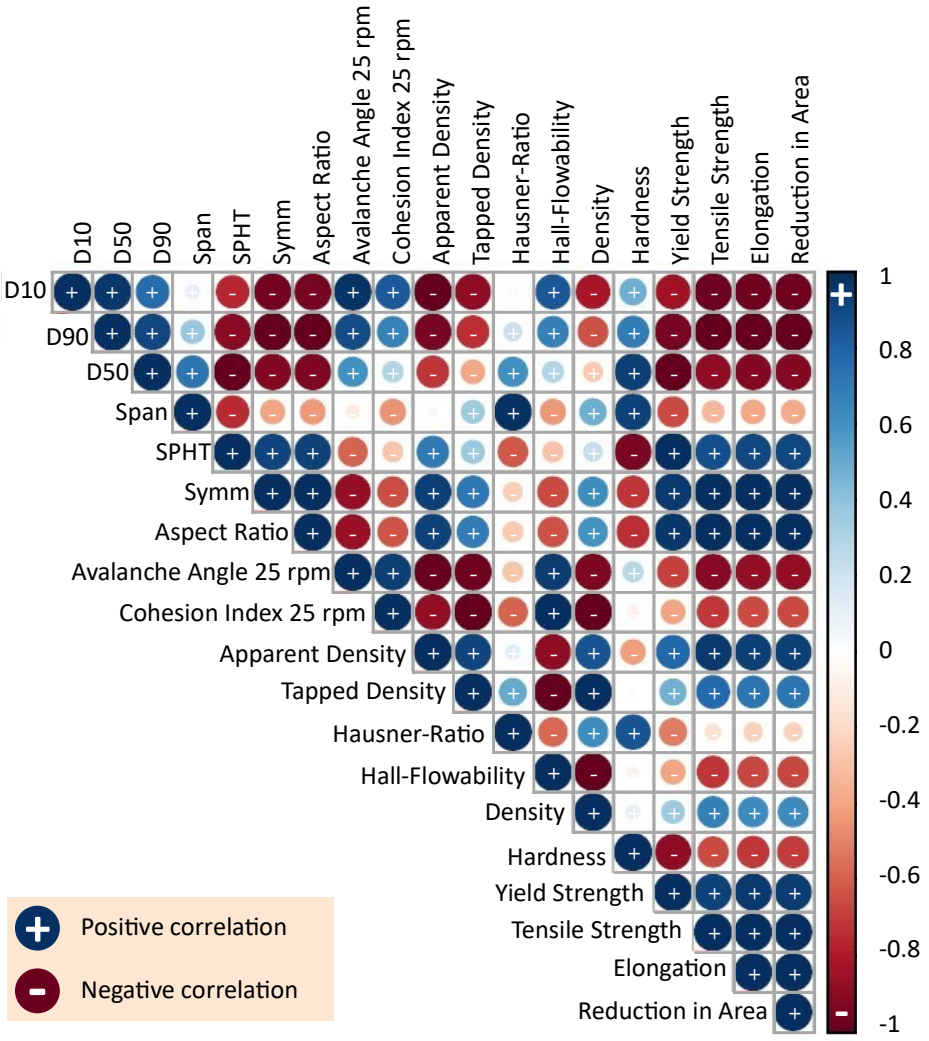

Figure 7-8: Correlation matrix based on Pearson coefficient of Ti-6Al-4V results.

7.2.2.2 Discussion of Correlation Analysis

The statistical evaluation indicates lower apparent and tapped densities for larger particle sizes, as observed with EBM_45-106. An increased PSD increases avalanche angle and cohesion index, thus reducing flowability. Conversely, a larger PSD also correlates with decreased relative density and tensile properties. This could be due to a less homogeneous and dense powder application, increasing the likelihood of voids and irregularities in the powder bed, which in turn influences the melt pool and diminishes the mechanical properties. Another potential reason is the process parameters, which are specifically adapted to maximize relative density rather than strength or ductility. Since high relative densities and industry-reference mechanical properties are achieved across all PSDs, it is more likely that the process parameters contributed to the observed reduction in tensile properties. The complexity of the causal relationship between powder properties, processing conditions, and part qualities, as discussed by Sun et al., underscores the need for further investigation [185].

Although particle shape is correlated with improved flowability and tensile properties, this needs to be relativized due to the similarity in particle shapes across the powders. Previous studies of Meier et al. and Muthuswamy et al. observe a correlation of higher particle sphericity with higher mechanical properties [70, 71]. In contrast, Vickers hardness analysis exhibits an inverse relationship, with higher hardness associated with increased PSDs and particle irregularity. The cooling rates from different

process parameters seem to be the dominant factor influencing hardness. One overlooked factor is the lower specific oxygen content in larger particles, which results from their lower specific surface area. This effect warrants further investigation. A significant challenge in interpreting the correlation analysis arises from the similarity in the Ti-6Al-4V test results. Most deviations fall within the standard deviations, making it difficult to identify clear trends in this investigation. Notably, the particle size does not exhibit any clear negative impact on manufacturability.

In conclusion: Multiple correlations are identified through mathematical analysis. However, causal attribution is limited because of the similarity in the results. The influence of PSD appears to be indirect, with process parameters playing a more significant role in the outcomes.

7.2.3 Key Findings on Manufacturability

In this section, the research question: "How do different PSDs affect the mechanical properties of the manufactured parts?" is investigated for Ti-6Al-4V powders. Adapted process parameters enable consistent microstructures and comparable densities across varying PSDs, although larger PSDs up to 106 µm require an 11.5 J/mm³ higher VED for manufacturing. Despite this, comparable hardness values are achieved, demonstrating that increased PSDs meet industry reference values and produce sound quality parts. For Ti-6Al-4V, the influence of larger particles becomes negligible with adapted process parameters, as both EBM_45-106 and Ti64_20-100 show reliable manufacturability. Furthermore, the findings highlight the feasibility of substituting PSDs from 20-53 µm to 20-100 µm while maintaining sound mechanical properties. An overview of the key findings is presented in Table 7-4.

Table 7-4: Key Findings of the investigations on Ti-6Al-4V manufacturability.

Criteria	Result AlMg11
relative density and microstructure	• Similar relative density (>99.9 %) meet reference industry values • Similar microstructure identified though different process parameters • No influence of PSD identified
Vickers hardness	• Similar Vickers hardness for large PSDs EBM_45-106 and Ti64_20-100 within 334 – 336 HV10; LPBF_20-53 slightly lower at 322 HV10 • Industry reference of 305-345 HV10 is met • Difference attributed to different process parameters
tensile properties	• Horizontal orientation, similar yield and tensile strength for all PSDs • Vertical orientation, LPBF_20-53 higher strength and ductility • Industry reference values are reached
correlation analysis	• Multiple correlations are mathematically identified, with causal attribution limited due to similarity in results • Indirect influence of PSD due to high influence of process parameters

8 Investigation of Resource and Cost-Saving Potential

In this chapter, the effect of the manufacturable PSD on achievable resource and cost savings is examined.

8.1 Results of Resource Analysis

The average powder yield from atomization varies between 10 % and 55 % for a typical LPBF PSD of 20-70 µm, depending on the atomization technologies and parameters [5–8]. Consequently, all economic analyses of resource reduction potential are based on approximations. In Figure 8-1, AlMg11 PSD6_20-170 is used as an example of a fully atomized powder yield. Fine particles below 20 µm are sifted out of this powder. Based on the cumulative curve, the atomization yield for LPBF_20-70 is 43 %, while the use of PSD4_20-100 increases the yield to approximately 62 %, representing an increase of 44 % per atomization process.

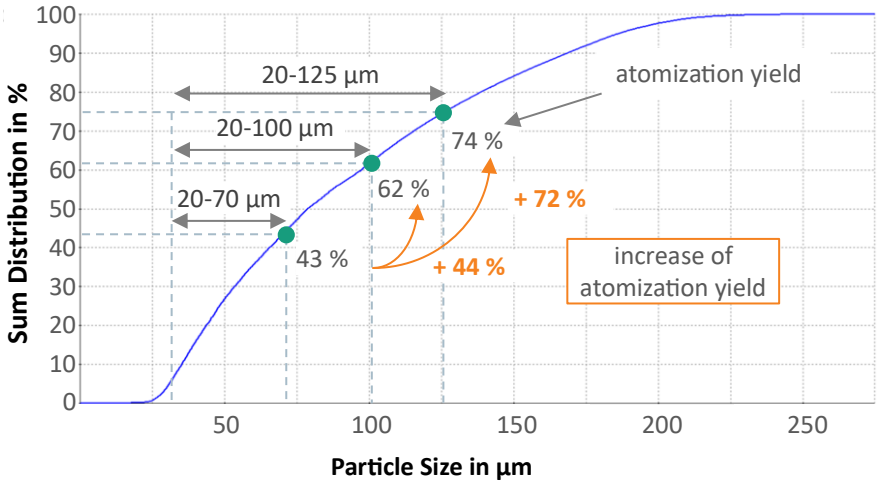

Figure 8-1: Diagram of AlMg11 PSD6_20-170 sum distribution representing the full atomization yield with utilized PSDs indicated across particle sizes.

In Figure 8-2, the effect of increasing the PSD from 20-70 µm to 20-100 µm on atomization yield is analysed using literature data from (a) Qi et al. and (b) Anderson and Terpstra.

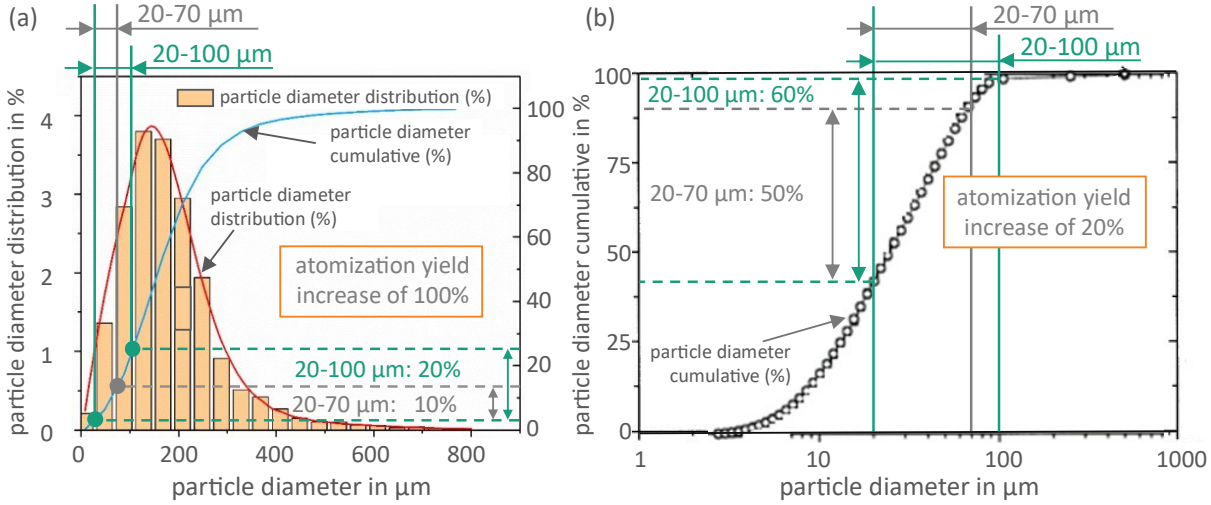

Figure 8-2: Diagram of cumulative particle diameters and particle diameter distribution across particle sizes with utilized powder yield indicated for LPBF 20-70 and for 20-100 µm (a) from Qi et al. [5], and (b) from Anderson and Terpstra [6].

Qi et al. present a particle diameter graph for FeCrNiBSiNb in Figure 8-2 (a), showing an increase in yield from 10 % for 20-70 µm to 20 % for 20-100 µm, representing an 100 % increase, and further to 30 % for 20-125 µm [5]. Anderson and Terpstra report a 20 % increase in atomization yield for 316L when utilizing the PSD range of 20-100 µm, as shown in Figure 8-2 (b) [6]. In further studies, Li et al. investigate different nozzle inner diameters ranging from 1 to 4 mm, reporting powder yields of approximately 20-55 % for 20-70 µm and 30-70 % for 20-100 µm. This demonstrates a potential increase of 27-50 % in yield for utilizing 20-100 µm [8]. Xiongfei et al. vary the feed rate of an electrode inert gas atomization process and observe yields of 30-40 % for 20-70 µm, 50-60 % for 20-100 µm, and 60-70 % for 20-125 mm for γ-TiAl. The use of 20-100 µm PSD increases the powder yield by approximately 50-67 %, and the use of 20-125 µm by 75-100 % [7].

8.2 Discussion of Resource Analysis

The comparison of literature atomization yields with the cumulative values from PSD6_20-170 indicates sufficient transferability of the investigated results to the literature. It is concluded that increasing the PSD from 20-70 µm to 20-100 µm features the potential to increase the LPBF atomization yield by 44 %. An exact atomization yield increase is not determinable, since powder yield data from commercial atomizers remain a closely guarded trade secret. For AM-tailored, atomized alloys such as AlMg11, this results in cost reduction possibilities for the powder atomizer by reducing the effort for sieving and classification. The resource saving effects are particular notable in reduced re-melting efforts (such as oxygen reduction), lower overall energy consumption and fewer process steps such as sieving [168]. The extent of cost reductions passed on to the customer largely depends on the powder atomizer.

8.3 Results of Cost Analysis

To assess the potential cost savings for LPBF through the additional use of larger powders, such as 45–106 µm EBM powder, a market survey is performed as described in Section 4.6.

The offers received as part of the market survey are anonymously presented in Figure-8-3. In the category “LPBF” the prices are summarized that cover typical LPBF PSDs between 20-53 and 20-63 µm. In “EBM”, the PSDs are summarized of 44-106 µm, 45-100 µm and 45-125 µm. The suppliers offer fixed PSDs, it is therefore not possible to compare the same PSDs.

For both PSDs, LPBF and EBM, scaling effects are identified. The average price for LPBF powder falls by 12 % and the average price for EBM powder by 19 %, if the order quantity is increased from 100 kg to 1,000 kg. With EBM PSD, the quantity of 100 kg costs on average 38 % less, while 1,000 kg costs 44 % less.

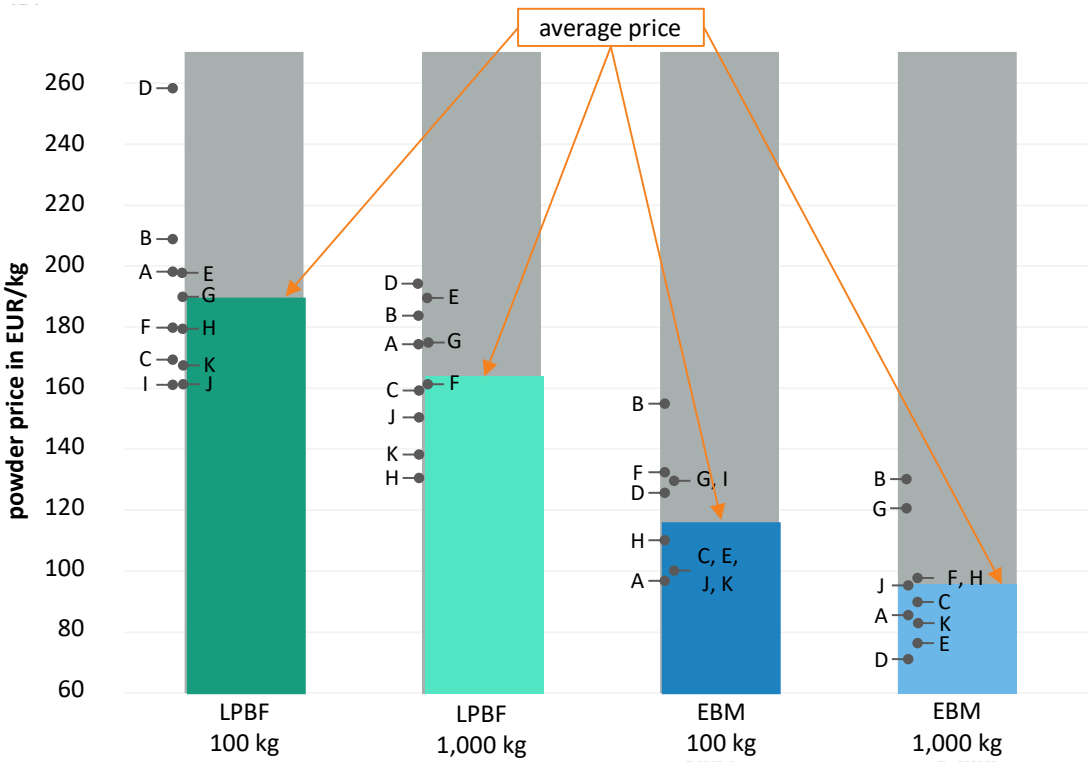

Figure-8-3: Diagram of Ti-6Al-4V prices of LPBF and EBM PSDs for 100 kg and 1,000 kg.

Overall, the comparison of the various suppliers shows large differences between the lowest and the highest offers of up to almost 100 EUR/kg, as highlighted in Table 8-1.

Table 8-1: Ti-6Al-4V Comparison of the lowest and highest powder prices for LPBF and EBM.

	LPBF		**EBM**	
	100 kg	**1,000 kg**	**100 kg**	**1,000 kg**
Lowest Prices	162.31 EUR/kg	130.20 EUR/kg	97.20 EUR/kg	71.20 EUR/kg
Highest Prices	260.00 EUR/kg	196.30 EUR/kg	155.00 EUR/kg	130.00 EUR/kg

In Figure 8-4, the costs of the investigated powders blended in a 1:1 ratio, based on the prices for 100 kg and excluding any additional blending costs, are illustrated. By incorporating a blend of 50 % LPBF powder and 50 % EBM powder to achieve a PSD of 20–100 µm, an average cost reduction of approximately 20 % is realized.

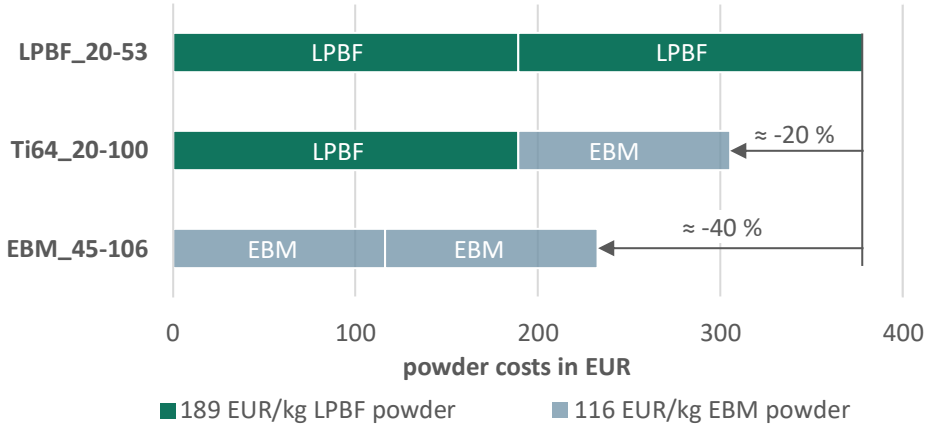

Figure 8-4: Diagram of powder costs distribution for an equal-proportion blend per investigated PSD.

8.4 Discussion of Cost Analysis

For alloys already supplied as powders to other industries in various PSDs, such as Ti-6Al-4V, this investigation highlights the potential of purchasing larger PSDs for LPBF. EBM powders are 40 % more cost-effective, leading to a 20 % cost reduction when using a 1:1 blend of 20-100 µm.

A more profound understanding of PSDs, powder characteristics, LPBF and mechanical properties, additionally allows for precise process adaptions to PSD deviations, such as increased PSDs. These deviations are proven by Cordova et al. to occur due to powder re-use [76]. The powder application tests confirmed the coarsening effect. Adjusting process parameters to account for this coarsening could extend the re-use life of powders, resulting in further resource and cost savings.

8.5 Key Findings on Resource and Cost-Saving Potential

The investigation of resource and cost savings addresses the question: “How does PSD influence resources and costs?” The findings demonstrate that utilizing a 20-100 µm PSD, given its achieved processability and manufacturability, potentially increases atomization yield by 44 % compared to typical LPBF PSDs, such as 20-70 µm. For Ti-6Al-4V, market data indicate a potential cost reduction of 20 % when using a 20-100 µm PSD. The quantitative contribution of this thesis is summarized in Figure 8-5.

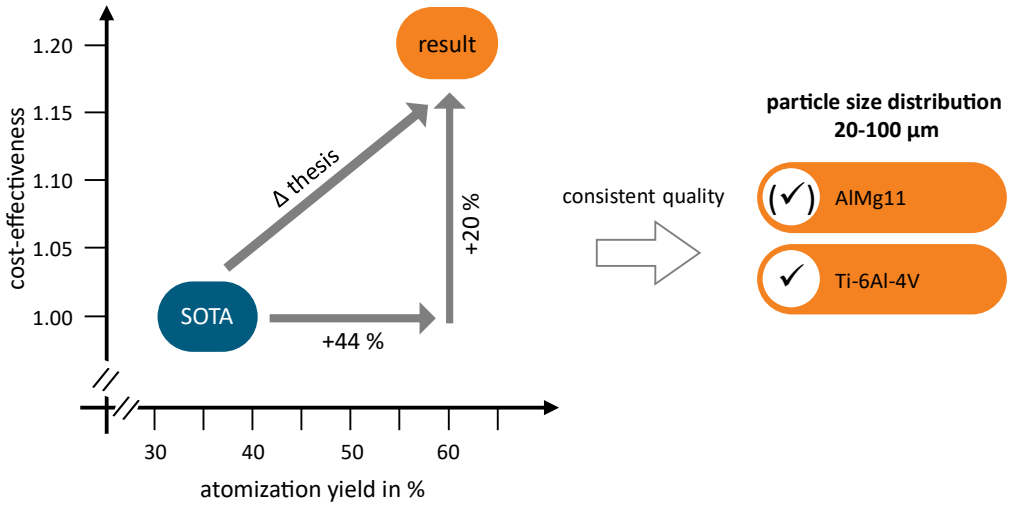

Figure 8-5: Diagram of the variables for a quantitative description of the contribution to the SOTA (left) and level of achievement for 20-100 µm (right).

9 Conclusion and Outlook

The influence of integrating larger PSDs (up to 20-125 µm) into LPBF of aluminium and titanium alloys to examined. Unexploited potential for significant resource and material cost savings is identified by increasing atomization yields up to 74 %. The findings are summarized as follows:

1. Can you generate different PSDs from commercial PSDs for LPBF?

The generation of distinct PSDs through blending and sieving is successfully confirmed. The developed V-Blender is verified as a suitable methodology for generating homogeneous blends in an inert gas atmosphere without significant particle degradation. Thermal oxidation proved to be an effective method for particle marking to verify blending homogeneity, which is achieved after approximately 10 minutes of blending at 40 rpm.

2. What is the effect of the PSD on processability?

For AlMg11, a mix of particles smaller and larger than 70 µm favours higher apparent and tapped density and faster Hall flowability compared to LPBF_20-70. Although no clear link to avalanche angle is observed, wider PSDs (spans between 69-132 µm) exhibit lower cohesion indices and enhanced flowability. All PSDs achieve a relative density of 99.5 % in manufactured parts for scanning speeds up to 1,025 mm/s. PSD4_20-100 and PSD5_20-125 achieve the widest process windows, with scanning speeds of 805-1,405 mm/s and 805-1,175 mm/s, respectively, to reach relative part densities above 99.5 %.

For Ti-6Al-4V, blending LPBF_20-53 and EBM_45-106 powders into Ti64_20-100 results in increased tapped density and faster Hall flowability compared to LPBF_20-53. Powders containing particles below 45 µm exhibit overall lower avalanche angles. The wide PSD of 20-100 µm achieves the lowest cohesion indices at rotational speeds above 15 rpm. A shear thickening effect is observed across all PSDs for both alloys. Two adapted process parameter combinations are identified, with one for LPBF_20-53 and another for EBM_45-106 and Ti64_20-100, the latter requiring an 11.5 J/mm³ higher VED due to the larger particles. The adaptation to 10 W higher laser power, 300 mm/s faster scanning speed, and a 0.05 mm smaller hatch distance, enables EBM_45-106 and Ti64_20-100 to reach relative part densities above 99.9 %.

PSD affects the processability in terms of mixed flowability results (reduced and increased) and similar relative part densities are achieved, for Ti-6Al-4V with adapted process parameters.

3. How do the different PSDs affect the mechanical properties of the manufactured parts?

For AlMg11, relative part densities are consistent with data sheet specifications (above 99.5 %), although pores and cracks are observed across all PSDs, possibly due to solidification or compositional issues rather than PSD alone. Hardness values remain within a narrow range (112-115 HV10), while tensile properties decrease slightly with increased layer counts, likely due to heat storage effects, particularly in larger PSDs (PSD4_20-100 and PSD5_20-125).

For Ti-6Al-4V, process parameters are adapted, which results in comparable mechanical properties across all PSDs. The relative densities exceed 99.9 %, with similar microstructures. The 4 % lower hardness (322 HV10) of LPBF_20-53 is attributed to slower cooling rates. In the horizontal orientation, tensile properties are similar, while in the vertical orientation, LPBF_20-53 slightly outperformed Ti64_20-100 and EBM_45-106, with all specimens meeting industry reference values. The influence of larger

particles on mechanical properties diminished when appropriate process parameters are applied, indicating reliable manufacturability for both EBM_45-106 and Ti64_20-100.

By implementing the identified adapted process parameters, the manufacturability of an increased PSD is successfully demonstrated, achieving mechanical properties comparable to industry reference values.

4. How does PSD influence resources and costs?

For AlMg11, the wider PSDs (PSD4_20-100 and PSD5_20-125) exhibit increased atomization yields of 62 % and 74 %, compared to 43 % for LPBF_20-70. For Ti-6Al-4V, blending EBM powder with LPBF powder in equal proportions offers 20 % material costs saving potential for additive manufacturing users. The utilization of increased atomization yields enhances the efficiency of customized AM alloy atomization by reducing the need for remelting and minimizing handling steps.

In conclusion, the posed research question “Can you manufacture sound-quality parts with increased particle size using LPBF aluminium and titanium alloys?” is answered as follows: it is possible to manufacture sound quality parts using LPBF with increased particle sizes in both aluminium and titanium alloys. For aluminium, minor limitations are observed, while for titanium alloys, part quality meets industry reference values. This approach offers potential resource savings of 44-72 % and cost reductions of 20 %, making it a viable method for enhancing the efficiency and cost-effectiveness of LPBF.

To further investigate resource and material cost savings, the powder life cycle offers potential through adjusted atomization processes or extended re-use and recycling strategies. Suggestions to increase atomization yield utilization include:

The selected V-blender represents one blending type, but no conclusions are drawn about the performance of other techniques. Future work should explore alternative blender designs and their impact on powder characteristics. Increased automation in blender handling enhances consistency, efficiency, and reduces manual labour. Current particle marking via thermal oxidation raises oxygen content, limiting further powder use. Sustainable marking methods require further study for viability in both initial and serial operations.

Advancements in process parameters, such as higher productivity through layer thickness larger than 60 µm, enhanced energy input, and laser beam shaping, show promise for manufacturability with larger particles. Findings on powder flowability and recoating behaviour suggest adjusting recoater speeds to powder characteristics, with slower speeds tending to be more effective for larger particles. These observations align with simulation results from Lee et al. [171].

Process parameter selection depends on alloy characteristics, requiring dedicated studies to implement particles larger than 70 µm in LPBF. The greatest potential for resource and cost savings from increased PSDs lies in developing alloys specifically for LPBF. Excess particles from these alloys must be re-atomized for re-use. Collaboration with powder atomizers is essential for sourcing larger PSDs directly. The economic feasibility of powder blending should be assessed for each LPBF setup, considering machine capacity and usage. Regulatory requirements in regulated industries must also be carefully addressed when blending powders from different batches.

10 References

[1] *DIN EN ISO/ASTM 52900:2017-06, Additive Manufacturing-General Principles*, DIN EN ISO 52900, Berlin, Jun. 2017.

[2] M. Munsch, M. Schmidt-Lehr and E. Wycisk, "AMPOWER REPORT 2024: Additive Manufacturing Market Report," AMPOWER GmbH & Co. KG, 2024.

[3] A.B. Spierings and N. Herres and G. Levy, "Influence of the particle size distribution on surface quality and mechanical properties in AM steel parts," *Rapid Prototyping Journal*, vol. 17, no. 3, pp. 195–202, 2011, doi: 10.1108/13552541111124770].

[4] I. M. Kusoglu, B. Gökce, and S. Barcikowski, "Research trends in laser powder bed fusion of Al alloys within the last decade," *Additive Manufacturing*, vol. 36, p. 101489, 2020, doi: 10.1016/j.addma.2020.101489.

[5] H. Qi, X. Zhou, J. Li, Y. Hu, and L. Xu, "Performance Testing and Rapid Solidification Behavior of Stainless Steel Powders Prepared by Gas Atomization," *Materials*, vol. 14, no. 18, 2021, doi: 10.3390/ma14185188.

[6] I. Anderson and R. L. Terpstra, "Progress toward gas atomization processing with increased uniformity and control," *Materials Science and Engineering*, A326, pp. 101–109, 2002.

[7] Z. Xiongfei, C. Shiqi, L. Yong, L. Ruidi, and W. Hong, "Preparation of Ti6Al4V Powder with High Yield of Fine Particle by Crucible-less Gas Atomization Technology," *Rare Metal Materials and Engineering*, 48(5), pp. 1461–1466, 2019.

[8] X. Li, Q. Zhu, S. Shu, J. Fan, and S. Zhang, "Fine spherical powder production during gas atomization of pressurized melts through melt nozzles with a small inner diameter," *Powder Technology*, vol. 356, pp. 759–768, 2019, doi: 10.1016/j.powtec.2019.09.023.

[9] R. Franke, "AlMgty80 Material Data sheet," Fehrmann, 2022.

[10] *VDI 3405 2.4 Additive manufacturing processes Laser powder bed fusion of metal (L-PBF-M) parts: Material data sheet titanium alloy Ti-6Al-4V grade 5*, 3405 Part 2.4, VDI – The Association of German Engineers, Berlin, Nov. 2019.

[11] I. Ludwig and M. Kluge, "Investigation of an Increased Particle Size Distribution of Ti-6Al-4V Powders Used for Laser-Based Powder Bed Fusion of Metals," *Materials*, vol. 17, no. 12, 2024, doi: 10.3390/ma17122942.

[12] *DIN 8580:2022-12, Manufacturing processes - Terms and classifications*, DIN 8580:2003-09, DIN-Normenausschuss Schweißtechnik (DVS), Berlin, 2003.

[13] T. Kimura, T. Nakamoto, M. Mizuno, and H. Araki, "Effect of silicon content on densification, mechanical and thermal properties of Al-xSi binary alloys fabricated using selective laser melting," *Materials Science and Engineering: A*, vol. 682, pp. 593–602, 2017, doi: 10.1016/j.msea.2016.11.059.

[14] Andreas Gebhardt, *Additive Fertigungsverfahren: Additive Manufacturing und 3D-Drucken für Prototyping - Tooling - Produktion*: Carl Hanser Verlag GmbH & Co. KG, 2016.

[15] B. P. Conner *et al.,* "Making sense of 3-D printing: Creating a map of additive manufacturing products and services," *Additive Manufacturing*, 1-4, pp. 64–76, 2014, doi: 10.1016/j.addma.2014.08.005.

[16] V. Bhavar, P. Kattire, V. Patil, S. Khot, K. Gujar, and R. Singh, "A review on powder bed fusion technology of metal additive manufacturing," pp. 251–253, 2017, doi: 10.1201/9781315119106-15.

[17] MESAGO, "AM field guide compact," Mesago Messe Frankfurt GmbH, 2022.

[18] R. Baitimerov, P. Lykov, D. Zherebtsov, L. Radionova, A. Shultc, and K. G. Prashanth, "Influence of Powder Characteristics on Processability of AlSi12 Alloy Fabricated by Selective Laser Melting," 2018.

[19] D. Wimler, S. Kardos, J. Lindemann, H. Clemens, and S. Mayer, "Aspects of Powder Characterization for Additive Manufacturing," *Practical Metallography*, vol. 55, no. 9, pp. 620–636, 2018.

[20] M. A. Balbaa, A. Ghasemi, E. Fereiduni, M. A. Elbestawi, S. D. Jadhav, and J.-P. Kruth, "Role of powder particle size on laser powder bed fusion processability of AlSi10mg alloy," *Additive Manufacturing*, vol. 37, p. 101630, 2021, doi: 10.1016/j.addma.2020.101630.

[21] D. Jafari and W. W. Wits, "The utilization of selective laser melting technology on heat transfer devices for thermal energy conversion applications: A review," *Renewable and Sustainable Energy Reviews*, vol. 91, pp. 420–442, 2018, doi: 10.1016/j.rser.2018.03.109.

[22] E. Louvis, P. Fox, and C. J. Sutcliffe, "Selective laser melting of aluminium components," *Journal of Materials Processing Technology*, vol. 211, no. 2, pp. 275–284, 2011, doi: 10.1016/j.jmatprotec.2010.09.019.

[23] E. Brandl, U. Heckenberger, V. Holzinger, and D. Buchbinder, "Additive manufactured AlSi10Mg samples using Selective Laser Melting (SLM): Microstructure, high cycle fatigue, and fracture behavior," *Materials & Design*, vol. 34, pp. 159–169, 2012, doi: 10.1016/j.matdes.2011.07.067.

[24] Z. Young *et al.,* "Effects of Particle Size Distribution with Efficient Packing on Powder Flowability and Selective Laser Melting Process," *Materials*, vol. 15, no. 3, 2022, doi: 10.3390/ma15030705.

[25] T. Wohlers, R. I. Campbell, O. Diegel, J. Kowen, N. Mostow, and I. Fidan, *Wohlers Report 2022: 3D Printing and Additive Manufacturing*. Global State of the Industry. Fort Collins, Colorado, Washington, DC: Wohlers Associates; ASTM International, 2022.

[26] T. M. Wischeropp, C. Emmelmann, M. Brandt, and A. Pateras, "Measurement of actual powder layer height and packing density in a single layer in selective laser melting," *Additive Manufacturing*, vol. 28, pp. 176–183, 2019, doi: 10.1016/j.addma.2019.04.019.

[27] A. B. Spierings, M. Voegtlin, T. Bauer, and K. Wegener, "Powder flowability characterisation methodology for powder-bed-based metal additive manufacturing," *Progress in Additive Manufacturing*, vol. 1, 1-2, pp. 9–20, 2016, doi: 10.1007/s40964-015-0001-4.

[28] P. Wang, D. Chen, Y. Tang, J. Fan, and G. Li, "The effect of process parameters on the stability and efficiency in the laser powder bed fusion of Ti-6Al-4 V based on the interval powder layer

thickness," *The International Journal of Advanced Manufacturing Technology*, vol. 127, 7-8, pp. 3537–3556, 2023, doi: 10.1007/s00170-023-11704-7.

[29] Y. Jing, P. Wang, and X. Yan, "Effect of Process Parameters and Layer Thickness on the Quality and Performance of Ti-6Al-4V Fabricated by Selective Laser Melting," *Coatings*, vol. 11, no. 11, p. 1323, 2021, doi: 10.3390/coatings11111323.

[30] F. Bosio *et al.,* "A time-saving and cost-effective method to process alloys by Laser Powder Bed Fusion," *Materials & Design*, vol. 181, p. 107949, 2019, doi: 10.1016/j.matdes.2019.107949.

[31] F. Chu *et al.,* "Influence of satellite and agglomeration of powder on the processability of AlSi10Mg powder in Laser Powder Bed Fusion," *Journal of Materials Research and Technology*, vol. 11, pp. 2059–2073, 2021, doi: 10.1016/j.jmrt.2021.02.015.

[32] A. Bauch, P. Kohlwes, and I. Kelbassa, "Laser powder bed fusion of pure copper using ring-shaped beam profiles," *Journal of Laser Applications*, vol. 36, no. 4, 2024, doi: 10.2351/7.0001562.

[33] I. Gibson, D. Rosen, B. Stucker, and M. Khorasani, Eds., *Additive Manufacturing Technologies*. Cham: Springer International Publishing, 2021.

[34] C. D. Boley, S. A. Khairallah, and A. M. Rubenchik, "Calculation of laser absorption by metal powders in additive manufacturing," *Applied optics*, vol. 54, no. 9, pp. 2477–2482, 2015, doi: 10.1364/AO.54.002477.

[35] A. Suzuki, T. Miyasaka, N. Takata, M. Kobashi, and M. Kato, "Control of microstructural characteristics and mechanical properties of AlSi12 alloy by processing conditions of laser powder bed fusion," *Additive Manufacturing*, vol. 48, p. 102383, 2021, doi: 10.1016/j.addma.2021.102383.

[36] *Aluminium and aluminium alloys - Chemical composition and form of wrought products: Part 1: Numerical designation system; German version EN_573-1:2004*, DIN EN 573-1:2005-02, Berlin.

[37] E. Roos, K. Maile, and M. Seidenfuß, *Werkstoffkunde für Ingenieure*. Berlin, Heidelberg: Springer Berlin Heidelberg, 2022.

[38] U.S. Titanium Industry Inc., "Titanium Alloys - Ti6Al4V Grade 5," 2002.

[39] S. Keaveney, A. Shmeliov, V. Nicolosi, and D. P. Dowling, "Investigation of process by-products during the Selective Laser Melting of Ti6AL4V powder," *Additive Manufacturing*, vol. 36, p. 101514, 2020, doi: 10.1016/j.addma.2020.101514.

[40] *Titanium alloys - Chemical composition*, DIN 17851:2023-05, Berlin.

[41] *Specification for Titanium and Titanium Alloy Bars and Billets*, ASTM B 348/B 348M:2021, B10 Committee, West Conshohocken, Pennsylvania.

[42] L. Thijs, F. Verhaeghe, T. Craeghs, J. van Humbeeck, and J.-P. Kruth, "A study of the microstructural evolution during selective laser melting of Ti–6Al–4V," *Acta Materialia*, vol. 58, no. 9, pp. 3303–3312, 2010, doi: 10.1016/j.actamat.2010.02.004.

[43] M. Asherloo *et al.,* "Understanding process-microstructure-property relationships in laser powder bed fusion of non-spherical Ti-6Al-4V powder," *Materials Characterization*, vol. 198, p. 112757, 2023, doi: 10.1016/j.matchar.2023.112757.

[44] P. G. Partridge, "Cyclic twinning in fatigued close-packed hexagonal metals," *The Philosophical Magazine: A Journal of Theoretical Experimental and Applied Physics*, vol. 12, no. 119, pp. 1043–1054, 1965, doi: 10.1080/14786436508228133.

[45] N. Kazantseva, P. Krakhmalev, M. Thuvander, I. Yadroitsev, N. Vinogradova, and I. Ezhov, "Martensitic transformations in Ti-6Al-4V (ELI) alloy manufactured by 3D Printing," *Materials Characterization*, vol. 146, pp. 101–112, 2018, doi: 10.1016/j.matchar.2018.09.042.

[46] T. Vilaro, C. Colin, and J. D. Bartout, "As-Fabricated and Heat-Treated Microstructures of the Ti-6Al-4V Alloy Processed by Selective Laser Melting," *Metallurgical and Materials Transactions A*, vol. 42, no. 10, pp. 3190–3199, 2011, doi: 10.1007/s11661-011-0731-y.

[47] J. Yang, H. Yu, J. Yin, M. Gao, Z. Wang, and X. Zeng, "Formation and control of martensite in Ti-6Al-4V alloy produced by selective laser melting," *Materials & Design*, vol. 108, pp. 308–318, 2016, doi: 10.1016/j.matdes.2016.06.117.

[48] M. Asherloo *et al.,* "Fatigue performance of laser powder bed fusion hydride-dehydride Ti-6Al-4V powder," *Additive Manufacturing*, vol. 59, p. 103117, 2022, doi: 10.1016/j.addma.2022.103117.

[49] H. Gu, H. Gong, J. Dilip, and D. Pal, "Effects of Powder Variation on the Microstructure and Tensile Strength of Ti6Al4V Parts Fabricated by Selective Laser Melting," *Solid Freeform Fabrication Symposium*, 2014.

[50] M. Xue, Xinyue Chen, Xia Ji, Xinliang Xie, and Qi Chao and Guohua Fan, "Effect of Particle Size Distribution on the Printing Quality and Tensile Properties of Ti-6Al-4V Alloy Produced by LPBF Process," *Metals*, vol. 13, no. 604, 2023, doi: 10.3390/met13030604.

[51] W. Xu *et al.,* "Additive manufacturing of strong and ductile Ti–6Al–4V by selective laser melting via in situ martensite decomposition," *Acta Materialia*, vol. 85, pp. 74–84, 2015, doi: 10.1016/j.actamat.2014.11.028.

[52] I. Yadroitsev, P. Krakhmalev, and I. Yadroitsava, "Selective laser melting of Ti6Al4V alloy for biomedical applications: Temperature monitoring and microstructural evolution," *Journal of Alloys and Compounds*, vol. 583, pp. 404–409, 2014, doi: 10.1016/j.jallcom.2013.08.183.

[53] C. Charles, "Modelling microstructure evolution of weld deposited Ti-6Al-4V," Department of Applied Physics and Mechanical Engineering Division of Material Mechanics, Luleå University of Technology, Luleå, Sweden, 2008.

[54] R. Coleman, "Microstructural analysis of TI6Al4V components made by EBM," Department of Metallurgical and Materials Engineering, The University of Alabama, Tuscaloosa, Alabama, US, 2017.

[55] S. Siddique, M. Imran, E. Wycisk, C. Emmelmann, and F. Walther, "Influence of process-induced microstructure and imperfections on mechanical properties of AlSi12 processed by selective laser melting," *Journal of Materials Processing Technology*, vol. 221, pp. 205–213, 2015, doi: 10.1016/j.jmatprotec.2015.02.023.

[56] Z. Liang, Z. Sun, W. Zhang, S. Wu, and H. Chang, "The effect of heat treatment on microstructure evolution and tensile properties of selective laser melted Ti6Al4V alloy," *Journal of Alloys and Compounds*, vol. 782, pp. 1041–1048, 2019, doi: 10.1016/j.jallcom.2018.12.051.

[57] E. Sallica-Leva, R. Caram, A. L. Jardini, and J. B. Fogagnolo, "Ductility improvement due to martensite α' decomposition in porous Ti-6Al-4V parts produced by selective laser melting for orthopedic implants," *Journal of the mechanical behavior of biomedical materials*, vol. 54, pp. 149–158, 2016, doi: 10.1016/j.jmbbm.2015.09.020.

[58] N.N., "Material Data Sheet: Titanium Ti64 Grade 23," EOS GmbH Electro Optical Systems, Krailling/Munich, Germany, Jul. 2022. [Online]. Available: https://uk.eos.info/03_system-related-assets/material-related-contents/metal-materials-and-examples/metal-material-datasheet/titan/ti64/material_datasheet_eos_titanium_ti64_grade23_premium_en_web.pdf

[59] D. Scheel, "Material Data Sheet: Ti-Alloy Ti6Al4V ELI (Grade 23) / 3.7165 / B348 / F136," Nikon SLM Solutions GmbH, Oct. 2020. [Online]. Available: https://www.slm-solutions.com/fileadmin/Content/Powder/MDS/MDS_Ti-Alloy_Ti6Al4V__ELI_0719_EN.pdf

[60] L. Cordova, T. Bor, M. de Smit, M. Campos, and T. Tinga, "Measuring the spreadability of pre-treated and moisturized powders for laser powder bed fusion," *Additive Manufacturing*, vol. 32, p. 101082, 2020, doi: 10.1016/j.addma.2020.101082.

[61] C. Weiss, J. Heslenfeld, J. K. Saewe, S. Bremen, and C. L. Häfner, "Investigation on the influence of powder humidity in Laser Powder Bed Fusion (LPBF)," *Procedia CIRP*, vol. 111, pp. 115–120, 2022, doi: 10.1016/j.procir.2022.08.102.

[62] F. Ostermann, *Anwendungstechnologie Aluminum*. Berlin, Heidelberg: Springer Berlin Heidelberg, 2007.

[63] D. M. Bauer, E. Schwarzenböck, I. Ludwig, N. Schupp, F. Palm, and G. Witt, "Investigations of aging behaviour for aluminium powders during an atmosphere simulation of the LBM process," *Powder Metallurgy*, vol. 60, no. 3, pp. 175–183, 2017, doi: 10.1080/00325899.2017.1288841.

[64] M. Murtomaa, J. Peltonen, and J. Salonen, "One-step measurements of powder resistivity as a function of relative humidity and its effect on charging," *Journal of Electrostatics*, vol. 76, pp. 78–82, 2015, doi: 10.1016/j.elstat.2015.05.016.

[65] V. Seyda, "Werkstoff- und Prozessverhalten von Metallpulvern in der laseradditiven Fertigung," Doctoral Thesis, Institute of Laser and System Technologies, Technical University of Hamburg, 2018.

[66] Q. Li, I. Kucukkoc, and D. Z. Zhang, "Production planning in additive manufacturing and 3D printing," *Computers & Operations Research*, vol. 83, pp. 157–172, 2017, doi: 10.1016/j.cor.2017.01.013.

[67] C. Weingarten, D. Buchbinder, N. Pirch, W. Meiners, K. Wissenbach, and R. Poprawe, "Formation and reduction of hydrogen porosity during selective laser melting of AlSi10Mg," *Journal of Materials Processing Technology*, vol. 221, pp. 112–120, 2015, doi: 10.1016/j.jmatprotec.2015.02.013.

[68] G. Drossel, S. Friedrich, C. Kammer, W. Lehnert, W. Thate, M. Ullman, H.-W. Wenglorz, St. Zeltner, Ed., *Aluminium Taschenbuch 2: Umformung von Aluminium-Werkstoffen, Gießen von Aluminium-Teilen, Oberflächenbehandlung von Aluminium, Recycling und Ökologie*: Beuth Verlag GmbH, 2018.

[69] V. Seyda, D. Herzog, and C. Emmelmann, "Relationship between powder characteristics and part properties in laser beam melting of Ti–6Al–4V, and implications on quality," *Journal of Laser Applications*, vol. 29, no. 2, p. 22311, 2017, doi: 10.2351/1.4983240.

[70] B. Meier *et al.,* "Influence of Powder Production Process and Properties on Material Properties of Ti 6Al 4V Manufactured by L-PBF," *The International Journal of Advanced Manufacturing Technology*, vol. 123, 5-6, pp. 1577–1588, 2022, doi: 10.1007/s00170-022-10250-y.

[71] P. Muthuswamy, "Influence of powder characteristics on properties of parts manufactured by metal additive manufacturing," *Lasers in Manufacturing and Materials Processing*, 2022, doi: 10.1007/s40516-022-00177-3.

[72] G. Chen, S. Y. Zhao, P. Tan, J. Wang, C. S. Xiang, and H. P. Tang, "A comparative study of Ti-6Al-4V powders for additive manufacturing by gas atomization, plasma rotating electrode process and plasma atomization," *Powder Technology*, vol. 333, pp. 38–46, 2018, doi: 10.1016/j.powtec.2018.04.013.

[73] S. E. Brika, M. Letenneur, C. A. Dion, and V. Brailovski, "Influence of particle morphology and size distribution on the powder flowability and laser powder bed fusion manufacturability of Ti-6Al-4V alloy," *Additive Manufacturing*, vol. 31, p. 100929, 2020, doi: 10.1016/j.addma.2019.100929.

[74] S. Wallner, "Powder Production Technologies," *BHM Berg- und Huettenmaennische Monatshefte*, vol. 164, no. 3, pp. 108–111, 2019, doi: 10.1007/s00501-019-0832-2.

[75] I. Ludwig and M. Kluge, "Alliance Deep Dive: Cost Effective Powders for LBM," Fraunhofer Institution for Additive Manufacturing Technologies IAPT, 2021.

[76] L. Cordova, M. Campos, and T. Tinga, "Revealing the Effects of Powder Reuse for Selective Laser Melting by Powder Characterization," *JOM*, vol. 71, no. 3, pp. 1062–1072, 2019, doi: 10.1007/s11837-018-3305-2.

[77] W. WINTER, "Form and Meaning in Morphological Analysis," *Linguistics*, vol. 2, no. 3, 1964, doi: 10.1515/ling.1964.2.3.5.

[78] H. Wadell, "Volume, Shape, and Roundness of Rock Particles," *The Journal of Geology*, 1932.

[79] H. Fritsche, "Untersuchungen zur pneumatischen Förderung von Kohlenstaub zum Einblasen in den Hochofen unter besonderer Berücksichtigung instabiler Förderzustände," Fakultät für Natur- und Materialwissenschaften, Institut für Metallurgie, TU Clausthal, 2012.

[80] T. Brock, M. Groteklaes, P. Mischke, and B. Strehmel, *Lehrbuch der Lacktechnologie,* 4th ed. Hannover: Vincentz Network, 2012.

[81] *Powder metallurgy: Vocabulary*, DIN EN ISO 3252:2019, DIN-Normenausschuss Werkstofftechnologie (NWT), Berlin, Dec. 2019.

[82] W. Schatt, K.-P. Wieters, and B. Kieback, *Pulvermetallurgie*: Springer Berlin Heidelberg, 2007.

[83] *Additive manufacturing processes, rapid manufacturing Beam melting of metallic parts: Qualification, quality assurance and post processing*, VDI 3405 part 2, VDI – The Association of German Engineers, Aug. 2013.

[84] C. Meier, R. Weissbach, J. Weinberg, W. A. Wall, and A. J. Hart, "Critical Influences of Particle Size and Adhesion on the Powder Layer Uniformity in Metal Additive Manufacturing," *Journal of Materials Processing Technology*, vol. 266, pp. 484–501, 2019, doi: 10.1016/j.jmatprotec.2018.10.037.

[85] L. Haferkamp, S. Liechti, A. Spierings, and K. Wegener, "Effect of bimodal powder blends on part density and melt pool fluctuation in laser powder bed fusion," *Progress in Additive Manufacturing*, vol. 6, no. 3, pp. 407–416, 2021, doi: 10.1007/s40964-021-00179-1.

[86] A. M. Rausch, M. Markl, and C. Körner, "Predictive simulation of process windows for powder bed fusion additive manufacturing: Influence of the powder size distribution," *Computers & Mathematics with Applications*, vol. 78, no. 7, pp. 2351–2359, 2019, doi: 10.1016/j.camwa.2018.06.029.

[87] J. Zhang *et al.,* "Influence of Particle Size on Laser Absorption and Scanning Track Formation Mechanisms of Pure Tungsten Powder During Selective Laser Melting," *Engineering*, vol. 5, no. 4, pp. 736–745, 2019, doi: 10.1016/j.eng.2019.07.003.

[88] Z. Li, B.-Q. Li, P. Bai, B. Liu, and Y. Wang, "Research on the Thermal Behaviour of a Selectively Laser Melted Aluminium Alloy: Simulation and Experiment," *Materials*, vol. 11, no. 7, 2018, doi: 10.3390/ma11071172.

[89] D. Schulze, *Pulver und Schüttgüter: Fließeigenschaften und Handhabung*. Berlin, Heidelberg: Springer, 2014.

[90] L. Haferkamp *et al.,* "The Influence of Particle Shape, Powder Flowability, and Powder Layer Density on Part Density in Laser Powder Bed Fusion," *Metals*, vol. 11, no. 3, p. 418, 2021, doi: 10.3390/met11030418.

[91] M. Krantz, H. Zhang, and J. Zhu, "Characterization of powder flow: Static and dynamic testing," *Powder Technology*, vol. 194, no. 3, pp. 239–245, 2009, doi: 10.1016/j.powtec.2009.05.001.

[92] N.N., "Dynamic testing for secure powder characterisation," 1, 2013.

[93] A. Castellanos, "The relationship between attractive interparticle forces and bulk behaviour in dry and uncharged fine powders," *Advances in Physics*, vol. 54, no. 4, pp. 263–376, 2005, doi: 10.1080/17461390500402657.

[94] I. Baesso, D. Karl, A. Spitzer, A. Gurlo, J. Günster, and A. Zocca, "Characterization of powder flow behavior for additive manufacturing," *Additive Manufacturing*, vol. 47, p. 102250, 2021, doi: 10.1016/j.addma.2021.102250.

[95] H. P. Goh, P. W. S. Heng, and C. V. Liew, "Comparative evaluation of powder flow parameters with reference to particle size and shape," *International journal of pharmaceutics*, vol. 547, 1-2, pp. 133–141, 2018, doi: 10.1016/j.ijpharm.2018.05.059.

[96] A. T. Sutton, C. S. Kriewall, M. C. Leu, and J. W. Newkirk, "Powder characterisation techniques and effects of powder characteristics on part properties in powder-bed fusion processes," *Virtual and Physical Prototyping*, vol. 12, no. 1, pp. 3–29, 2016 // 2017, doi: 10.1080/17452759.2016.1250605.

[97] M. Habibnejad-korayem, J. Zhang, and Y. Zou, "Effect of particle size distribution on the flowability of plasma atomized Ti-6Al-4V powders," *Powder Technology*, vol. 392, pp. 536–543, 2021, doi: 10.1016/j.powtec.2021.07.026.

[98] Y. M. Akib, E. Marzbanrad, F. Ahmed, and J. Li, "A Numerical Study on the Powder Flowability, Spreadability, Packing Fraction in Powder Bed Additive Manufacturing," in *Proceedings of the ASME 2022 17th International Manufacturing Science and Engineering Conference*.

[99] T. Abu-Lebdeh, R. Damptey, V. Lamberti, and S. Hamoush, "Powder Packing Density and Its Impact on SLM-Based Additive Manufacturing," in *The Minerals, Metals & Materials Series, TMS 2019 148th Annual Meeting & Exhibition Supplemental Proceedings*, Cham: Springer International Publishing, 2019, pp. 355–367.

[100] M. C. H. Karg *et al.,* "Expanding particle size distribution and morphology of aluminium-silicon powders for Laser Beam Melting by dry coating with silica nanoparticles," *Journal of Materials Processing Technology*, vol. 264, pp. 155–171, 2019, doi: 10.1016/j.jmatprotec.2018.08.045.

[101] N. T. Aboulkhaira, I. Maskery, I. Ashcroft, C. Tuck, and N. M. Everitt, "The role of powder properties on the processability of Aluminium alloys in selective laser melting," in *Lasers in Manufacturing Conference 2015*.

[102] H. Yang, S. Li, Z. Li, and F. Ji, "Experimental and Numerical Study on the Packing Densification of Metal Powder with Gaussian Distribution," *Metals*, vol. 10, no. 11, p. 1401, 2020, doi: 10.3390/met10111401.

[103] A. Y. M. Alfaify, "The Effect of Changing Particle Size Distribution and Layer Thickness on the Density of Parts Manufactured UsingtheLaser Powder Bed Fusion Process," Advanced Manufacturing Research Centre, The Universtiy of Sheffield, 2019.

[104] K. Riener *et al.,* "Influence of particle size distribution and morphology on the properties of the powder feedstock as well as of AlSi10Mg parts produced by laser powder bed fusion (LPBF)," *Additive Manufacturing*, vol. 34, p. 101286, 2020, doi: 10.1016/j.addma.2020.101286.

[105] V. Ramesh Sagar *et al.,* "Investigating the Sensitivity of Particle Size Distribution on Part Geometry in Additive Manufacturing," in *Proceedings of the ASME 2020 International Mechanical Engineering Congress and Exposition*.

[106] S. Sendino, S. Martinez, F. Lartategui, M. Gardon, A. Lamikiz, and J. J. Gonzalez, "Effect of powder particle size distribution on the surface finish of components manufactured by laser powder bed fusion," *The International Journal of Advanced Manufacturing Technology*, vol. 124, 3-4, pp. 789–799, 2023, doi: 10.1007/s00170-022-10423-9.

[107] M. A. Spurek, L. Haferkamp, C. Weiss, A. B. Spierings, J. H. Schleifenbaum, and K. Wegener, "Influence of the particle size distribution of monomodal 316L powder on its flowability and processability in powder bed fusion," *Progress in Additive Manufacturing*, 2021, doi: 10.1007/s40964-021-00240-z.

[108] L. Marchetti and C. Hulme-Smith, "Flowability of steel and tool steel powders: A comparison between testing methods," *Powder Technology*, vol. 384, pp. 402–413, 2021, doi: 10.1016/j.powtec.2021.01.074.

[109] B. Daumann and H. Nirschl, "Bestimmung des Mischgüteverlaufes mit Hilfe der Bildauswertung beim diskontinuierlichen Feststoffmischen," *Symposium Produktgestaltung in der Partikeltechnologie*, 2008.

[110] M. Kraume, Ed., *Transportvorgänge in der Verfahrenstechnik: Grundlagen und apparative Umsetzungen,* 3rd ed. Berlin, Heidelberg: Springer, 2020.

[111] E. L. Paul, V. A. Atiemo-Obeng, and S. M. Kresta, *Handbook of industrial mixing: Science and practice*. Hoboken N.J.: Wiley-Interscience, 2004.

[112] M. Stieß, "Feststoffmischen und Rühren," in *Mechanische Verfahrenstechnik; 2009*, pp. 331–447.

[113] R. Weinekötter and H. Gericke, *Mischen von Feststoffen: Prinzipien, Verfahren, Mischer*. Berlin, Heidelberg: Springer, 1995.

[114] H. Schubert, *Handbuch der mechanischen Verfahrenstechnik: Partikeleigenschaften, Mikroprozesse, Makroprozesse, Schüttgut*. Weinheim: Wiley-VCH, 2002.

[115] V. A. Churu, "Homogenisation of Ti-6Al-4V powder blends during sintering," Facutly of Engineering and the Built Enviroment, University of Capetown, 2022.

[116] C. N. Ekaputra, D. Weiss, J.-E. Mogonye, and D. C. Dunand, "Eutectic, precipitation-strengthened alloy via laser fusion of blends of Al-7Ce-10Mg (wt.%), Zr, and Sc powders," *Acta Materialia*, vol. 246, p. 118676, 2023, doi: 10.1016/j.actamat.2023.118676.

[117] G. Huang, Z. Fan, L. Li, Y. Lu, and J. Lin, "Corrosion Resistance of Selective Laser Melted Ti6Al4V3Cu Alloy Produced Using Pre-Alloyed and Mixed Powder," *Materials*, vol. 15, no. 7, 2022, doi: 10.3390/ma15072487.

[118] G. Ma *et al.,* "Sustaining an excellent strength–ductility combination for Ti–6Al–4V alloy prepared from elemental powder blends," *Journal of Materials Research and Technology*, vol. 23, pp. 4965–4975, 2023, doi: 10.1016/j.jmrt.2023.01.231.

[119] Fransisco Medina, "Reducing Metal Alloy Powder Costs For Use In Powder Bed Fusion Additive Manufacturing: Improving The Economics For Production," Dissertation, Materials Science and Engineering, The University of Texas at El Paso, 2013.

[120] B. S. Parker, "Blending of powders for in-situ alloying of Ti6Al4V laser powder bed fusion," Faculty of Engineering, Stellenbosch University, 2021.

[121] M. Thamae, M. Maringa, and W. B. Du Preez, "Parameters Affecting the Mixing of Powders and the Results of Mixing SiC and Ti6Al4V (ELI) Powders," in *The 22nd Annual International RAPDASA Conference*, 2023.

[122] S. Vock, B. Klöden, A. Kirchner, T. Weißgärber, and B. Kieback, "Powders for powder bed fusion: a review," *Progress in Additive Manufacturing*, vol. 4, no. 4, pp. 383–397, 2019, doi: 10.1007/s40964-019-00078-6.

[123] A. Karambakhsh, A. Afshar, S. Ghahramani, and P. Malekinejad, "Pure Commercial Titanium Color Anodizing and Corrosion Resistance," *Journal of Materials Engineering and Performance*, vol. 20, no. 9, pp. 1690–1696, 2011, doi: 10.1007/s11665-011-9860-0.

[124] E. Gaul, "Coloring titanium and related metals by electrochemical oxidation," *Journal of Chemical Education*, 1993.

[125] M. V. Diamanti, B. Del Curto, and M. Pedeferri, "Interference colors of thin oxide layers on titanium," *Color Research & Application*, vol. 33, no. 3, pp. 221–228, 2008, doi: 10.1002/col.20403.

[126] A. Driewer, "Manual Particle Size Analyser Camsizer X2: hardware," Microtrac Retsch GmbH, 2020.

[127] *Particle size analysis - image analysis methods: Part 2: Dynamic image analysis methods*, ISO 13322-2, International Organisation for Standardisation, Nov. 2006.

[128] N.N., "Bedienungsanleitung Auswerte Software CAMSIZER X2," Microtrac Retsch GmbH, 2020.

[129] *Representation of results of particle size analysis: Part 1: Graphical representation*, DIN ISO 9276-1:2004-09, DIN ISO, Berlin, 2004.

[130] *Standard Test Method for Analysis of Titanium and Titanium Alloys by Direct Current Plasma and Inductively Coupled Plasma Atomic Emission Spectrometry (Performance-Based Test Methodology)*, ASTM E2371-21a, ASTM, 2022.

[131] *Test Methods for Determination of Carbon, Sulfur, Nitrogen, and Oxygen in Steel, Iron, Nickel, and Cobalt Alloys by Various Combustion and Fusion Techniques*, ASTM E 1019, ASTM, West Conshohocken, PA.

[132] *Titanium and titanium alloys: Determination of oxygen - Infrared method after fusion under inert gas*, ISO 22963:2008-01, ISO, Jan. 2008.

[133] *Test Method for Determination of Oxygen and Nitrogen in Titanium and Titanium Alloys by Inert Gas Fusion*, ASTM E1409, ASTM, West Conshohocken, Pennsylvania.

[134] *Test Method for Determination of Hydrogen in Titanium and Titanium Alloys by Inert Gas Fusion Thermal Conductivity: Infrared Detection Method*, ASTM E1447, ASTM, West Conshohocken, Pennsylvania.

[135] *Test Method for Determination of Carbon in Refractory and Reactive Metals and Their Alloys by Combustion Analysis*, ASTM E1941, ASTM, West Conshohocken, Pennsylvania.

[136] *Additive Manufacturing – Feedstock Materials: Methods to characterize metal powders*, DIN EN ISO/ASTM 52907, Berlin, Germany, May. 2020.

[137] *Metallic powders: Determination of flow rate by means of a calibrated funnel (Hall flowmeter)*, DIN EN ISO 4490:2008, Berlin, Germany, Feb. 2009.

[138] *Metallic powders - Determination of apparent density: Part 1: Funnel method*, DIN EN ISO 3923-1:2018-10, ISO, Berlin, Germany, Oct. 2018.

[139] *Metallic powders - Determination of tap density*, DIN EN ISO 3953:2011, Berlin, Germany, 2011.

[140] H. H. Hausner, "Powder Characteristics and their Effect on Powder Processing," *Powder Technology*, vol. 30, pp. 3–8, 1981.

[141] *Additive manufacturing of metals — Feedstock materials: Correlating of rotating drum measurement with powder spreadability in PBF-LB machines*, ISO/ASTM TR 52952:2023-06, Jun. 2023.

[142] S. Caubergh, "Granudrum Measurements: Cohesive Index CI," Granutools, 2022.

[143] N.N., "GranuDrum Operators Guide," Granutools, 2016.

[144] N.N., *Granudrum: The new powder rheometer: Dynamic Angle of Repose and Cohesive Index Measurements* (accessed: Aug. 19 2024).

[145] Z. Zheng *et al.,* "Microstructure and anisotropic mechanical properties of selective laser melted Ti6Al4V alloy under different scanning strategies," *Materials Science and Engineering: A*, vol. 831, p. 142236, 2022, doi: 10.1016/j.msea.2021.142236.

[146] T. Reiber, J. Rüdesheim, M. Weigold, E. Abele, J. Musekamp, and M. Oechsner, "Influence of contour scans on surface roughness and pore formation using Scalmalloy® manufactured by laser powder bed fusion (PBF‐LB)," *Materialwissenschaft und Werkstofftechnik*, vol. 52, no. 4, pp. 468–481, 2021, doi: 10.1002/mawe.202000287.

[147] J. P. Oliveira, A. D. LaLonde, and J. Ma, "Processing parameters in laser powder bed fusion metal additive manufacturing," *Materials & Design*, vol. 193, p. 108762, 2020, doi: 10.1016/j.matdes.2020.108762.

[148] T. Wischeropp, "Advancement of Selective Laser Melting by Laser Beam Shaping," Doctoral Thesis, Institute of Laser and System Technologies, Technical University of Hamburg, 2021.

[149] *Testing of metallic materials: Tensile test pieces*, DIN 50125, Dec. 2016.

[150] *Standard terminology for additive manufacturing: Coordinate systems and test methodologies*, DIN EN ISO/ASTM 52921, Jan. 2017.

[151] *Metallic Materials - Tensile Testing: Part 1: Method of test at room temperature*, DIN EN ISO 6892-1:2019, Jun. 2020.

[152] Obilor, Esezi Isaac: Amadi, Eric Chikweru, "Test for Significance of Pearson's Correlation Coefficient (r)," *International Journal of Innovative Mathematics, Statistics & Energy Policies*, vol. 6, no. 1, pp. 11–23, 2018.

[153] P. Kiani, U. S. Bertoli, A. D. Dupuy, K. Ma, and J. M. Schoenung, "A Statistical Analysis of Powder Flowability in Metal Additive Manufacturing," *Advanced Engineering Materials*, vol. 22, 2020, doi: 10.1002/adem.202000022.

[154] F. Del Re *et al.,* "Statistical approach for assessing the effect of powder reuse on the final quality of AlSi10Mg parts produced by laser powder bed fusion additive manufacturing," *The International Journal of Advanced Manufacturing Technology*, vol. 97, 5-8, pp. 2231–2240, 2018, doi: 10.1007/s00170-018-2090-y.

[155] Daniela Keller, *Analyse von Zusammenhängen: Korrelation.* [Online]. Available: https:// statistik-und-beratung.de/2013/05/analyse-von-zusammenhangen-korrelation/ (accessed: Apr. 6 2024).

[156] K. Dietrich, J. Diller, S. Dubiez-Le Goff, D. Bauer, P. Forêt, and G. Witt, "The influence of oxygen on the chemical composition and mechanical properties of Ti-6Al-4V during laser powder bed fusion (L-PBF)," *Additive Manufacturing*, vol. 32, p. 100980, 2020, doi: 10.1016/j.addma.2019.100980.

[157] *Standard Test Method for Analysis of Titanium and Titanium Alloys by Direct Current Plasma and Inductively Coupled Plasma Atomic Emission Spectrometry (Performance-Based Test Methodology)*, ASTM E 2371a, West Conshohocken, Pennsylvania, 2021.

[158] *Microbeam analysis: Quantitative analysis using energy-dispersive spectrometry (EDS) for elements with an atomic number of 11 (Na) or above*, DIN ISO 22309:2015-11, Nov. 2015.

[159] C. Pauzon, A. Raza, I. Hanif, S. Dubiez-Le Goff, J. Moverare, and E. Hryha, "Effect of layer thickness on spatter properties during laser powder bed fusion of Ti–6Al–4V," *Powder Metallurgy*, vol. 66, no. 4, pp. 333–342, 2023, doi: 10.1080/00325899.2023.2192036.

[160] T. Kim, "Effects of Heat Treatment on the Microstructure and Mechanical Properties of Electron Beam Additively Manufactured Ti6Al4V with Powder Reuse," Thesis, Department of Materials Science and Engineering, University of Washington, 2020.

[161] I. Ludwig, M. Kluge, D. Jutjuhn, M. Grube, P. Imgrund, and C. Emmelmann, "Investigations of air atomized and coarser gas-atomized AlSi12 powders to evaluate cost reduction potentials for additive manufacturing processes," Maastricht, October 2021.

[162] P. Kohlwes, I. Ludwig, A. Kouhestani-Farouji, D. Herzog, and C. Emmelmann, "Influence Analysis of Individual Powder Properties on L-PBF Process Capability," in *Fraunhofer Direct Digital Manufacturing Conference DDMC 2023*.

[163] A. Priyadarshi *et al.,* "New insights into the mechanism of ultrasonic atomization for the production of metal powders in additive manufacturing," *Additive Manufacturing*, vol. 83, p. 104033, 2024, doi: 10.1016/j.addma.2024.104033.

[164] H. P. Tang, M. Qian, N. Liu, X. Z. Zhang, G. Y. Yang, and J. Wang, "Effect of Powder Reuse Times on Additive Manufacturing of Ti-6Al-4V by Selective Electron Beam Melting," *JOM*, vol. 67, no. 3, pp. 555–563, 2015, doi: 10.1007/s11837-015-1300-4.

[165] S. M. Yusuf, E. Choo, and N. Gao, "Comparison between Virgin and Recycled 316L SS and AlSi10Mg Powders Used for Laser Powder Bed Fusion Additive Manufacturing," *Metals*, vol. 10, no. 12, p. 1625, 2020, doi: 10.3390/met10121625.

[166] T. Roy-Minard, "Ti-6Al-4V Material Test Certificate: TEKMAT Ti64-53_20-A, Lot 40968," Tekna Advanced Materials Inc., Québec, Canada, May. 2021.

[167] I. Smolina *et al.,* "Influence of the AlSi7Mg0.6 Aluminium Alloy Powder Reuse on the Quality and Mechanical Properties of LPBF Samples," *Materials*, vol. 15, no. 14, 2022, doi: 10.3390/ma15145019.

[168] K. Kassym and A. Perveen, "Atomization processes of metal powders for 3D printing," *Materials Today: Proceedings*, vol. 26, pp. 1727–1733, 2020, doi: 10.1016/j.matpr.2020.02.364.

[169] *Standard Test Method for Apparent Density of Non-Free-Flowing Metal Powders Using the Carney Funnel*, ASTM B417-13, West Conshohocken, Pennsylvania.

[170] J. L. P. Soh, C. V. Liew, and P. W. S. Heng, "New indices to characterize powder flow based on their avalanching behavior," *Pharmaceutical development and technology*, vol. 11, no. 1, pp. 93–102, 2006, doi: 10.1080/10837450500464123.

[171] Y. Lee, A. K. Gurnon, D. Bodner, and S. Simunovic, "Effect of Particle Spreading Dynamics on Powder Bed Quality in Metal Additive Manufacturing," *Integrating Materials and Manufacturing Innovation*, 2020, doi: 10.1007/s40192-020-00193-1.

[172] S. Slama, *Experimentalphysik kompakt für Naturwissenschaftler: Mechanik, Thermodynamik, Elektrodynamik, Optik & Quantenphysik*. Berlin, Heidelberg: Springer Spektrum, 2018.

[173] M. T. Andani, D. Reza, M. R. Karamooz-Ravari, R. Mirzaeifar, and J. Ni, "A study on the effect of energy input on spatter particles creation during selective laser melting process," *Additive Manufacturing*, vol. 20, pp. 33–43, 2018, doi: 10.1016/j.addma.2017.12.009.

[174] *Additive manufacturing processes - Powder bed fusion of metal with laser beam (PBF-LB/M): Defect catalogue - Defect images during laser beam melting*, VDI 3405 Blatt 2.8, VDI – The Association of German Engineers, Dec. 2022.

[175] Katja Schmitke, "Qualification of SLM - Additive Manufacturing for Aluminium," doctoral thesis, Institute of Laser and System Technologies, Technical University of Hamburg, 2019.

[176] T. Kimura, T. Nakamoto, T. Ozaki, K. Sugita, M. Mizuno, and H. Araki, "Microstructural formation and characterization mechanisms of selective laser melted Al–Si–Mg alloys with increasing magnesium content," *Materials Science and Engineering: A*, vol. 754, pp. 786–798, 2019, doi: 10.1016/j.msea.2019.02.015.

[177] Jim Clark, *Fundamentals of Inorganic Chemistry*. California, US.

[178] Cang Zhao, Niranjan D. Parab, Xuxiao L, Kamel Fezzaa, Wenda Tan, Anthony D. Rollett, and Tao Sun, "Critical instability at moving keyhole tip generates porosity in laser melting," *Science*, vol. 370, pp. 1080–1086, 2020.

[179] N. Tabatabaei, A. Zarei-Hanzaki, A. Moshiri, and H. R. Abedi, "The effect of heat treatment on the room and high temperature mechanical properties of AlSi10Mg alloy fabricated by selective laser melting," *Journal of Materials Research and Technology*, vol. 23, pp. 6039–6053, 2023, doi: 10.1016/j.jmrt.2023.02.086.

[180] C. N. Kuo, P. C. Peng, D. H. Liu, and C. Y. Chao, "Microstructure Evolution and Mechanical Property Response of 3D-Printed Scalmalloy with Different Heat-Treatment Times at 325 °C," *Metals*, vol. 11, no. 4, p. 555, 2021, doi: 10.3390/met11040555.

[181] V. S. Bhattiprolu and G. A. Crawford, "Microstructural Evolution and Mechanical Behavior of Heat Treated Ti-6Al-4V Powders," *Metallography, Microstructure, and Analysis*, vol. 7, no. 6, pp. 761–768, 2018, doi: 10.1007/s13632-018-0488-4.

[182] T. Maconachie *et al.,* "Effect of build orientation on the quasi-static and dynamic response of SLM AlSi10Mg," *Materials Science and Engineering: A*, vol. 788, p. 139445, 2020, doi: 10.1016/j.msea.2020.139445.

[183] P. K. Singh, S. Kumar, P. K. Jain, and U. S. Dixit, "Effect of Build Orientation on Metallurgical and Mechanical Properties of Additively Manufactured Ti-6Al-4V Alloy," *Journal of Materials Engineering and Performance*, 2023, doi: 10.1007/s11665-023-08218-4.

[184] C. M. Cepeda-Jiménez, F. Potenza, E. Magalini, V. Luchin, A. Molinari, and M. T. Pérez-Prado, "Effect of energy density on the microstructure and texture evolution of Ti-6Al-4V manufactured by laser powder bed fusion," *Materials Characterization*, vol. 163, p. 110238, 2020, doi: 10.1016/j.matchar.2020.110238.

[185] X. Sun *et al.,* "Characterization, preparation, and reuse of metallic powders for laser powder bed fusion: a review," *International Journal of Extreme Manufacturing*, vol. 6, no. 1, 2024, doi: 10.1088/2631-7990/acfbc3.

[186] *Systematic approach to the development and design of technical systems and products*, VDI 2221, VDI – The Association of German Engineers, Düsseldorf, Germany, 1993.

[187] I. Ludwig, A. Gerassimenko, and P. Imgrund, "Investigation of Metal Powder Blending for PBF-LB/M Using Particle Tracing with Ti-6Al-4V," *Journal of Manufacturing and Materials Processing*, vol. 8, no. 4, p. 151, 2024, doi: 10.3390/jmmp8040151.

[188] *Design engineering methodics: Engineering design at optimum cost - Valuation of costs*, VDI 2225 part 3, VDI – The Association of German Engineers, Nov. 1998.

[189] K. Langhorn, *Selecting appropriate powder blender.* [Online]. Available: https:// www.powderbulksolids.com/mixers-blenders/selecting-the-appropriate-powder-blender (accessed: May 19 2023).

[190] A. Bhattacharya, *Difference between a double cone blender and a V-Blender.* [Online]. Available: https://www.abilityfab.com/difference-between-double-cone-blender-and-v-blender/ (accessed: May 19 2023).

A Appendix

A.1 List of Figures

A.2 List of Tables

A.3 Systematic Approach to Blending Type Selection

The following sections describe the underlying list of requirements and the selection approach of the blender type for the development of the powder blender.

A.3.1 Requirements for powder blending

The VDI 2221 guideline provides the foundation for the powder blender development process [186]. In Table A-1, the specific requirements for effective powder blending are outlined.

Table A-1: List of powder blending requirements.

No.	Category	Requirement Description	Target
1.1	Container	Volume of the blend container	3 l – 10 l
1.2		Low surface roughness	< 1 µm Ra
2.1	System Architecture	Flexible suspension system for interchangable containers	
2.2		Discontinous blending	
3.1	Kinematics	electric drive with defined rotational speed	20, 40, 60 rpm
4.1	Interfaces	ISO-Standard interfaces	KF 40
4.2		Possibilities for sampling during the process	(>1 places)
4.3		Adapter unit for inert gas filling from stationary pipeline	
5.1	Monitoring	Oxygen content monitoring at filling	< 500 ppm
5.2		Overpressure measurement at operation	< 4 bar
6.1	Safety	Earthing of all components and the entire system	
6.2		Tightness against solid (powder) and gas	< 3 bar
6.3		Inert gas atmosphere in the blend chamber	Ar or N
6.4		Emergency stop switch	
6.5		Preservation of particle characteristics (size, shape, chemistry)	

In a preliminary selection, three mixer types, tumbling, convection and pneumatic, are selected for assessment in order to determine a suitable blending geometry [187]. These mixer types are evaluated for each selected principle on a 5-level scale according to VDI-2225 part 3 in Table A-2 [188].

A.3.2 Assessment of blender types

The assessment leads to the pre-selection of a tumbling blender. The advantages of a tumbling system are the low complexity, which reduces costs, and enables thorough cleaning. In addition, tumbling blenders are completely dischargeable [189]. The flexible design of the test rig allows the use of different blending container shapes such as V-shape or double cone containers. Bhattacharya states after testing both blending containers, the V-shape is more effective than the double cone shape. Therefore, the V-shape container geometry is selected for this study [190].

Table A-2: Blender Type Assessment for tumbling, convective and pneumatic blender types via pre-selected principles.

Principle	Tumbling Blender	Convective Blender	Pneumatic Blender
Suitability	●	◔	◑
Homogenization	◔	●	◔
Lab Scale	●	◑	◔
Low-impact Blending	●	◑	●
Complexity	●	◑	◔
Blending Time	◔	●	◔
Cleanability	●	◕	●
Total	●	◑	◔

Assessment: excellent ●, good ◔, fair ◑, unsatisfactory ◕, fail ○; acc. to VDI standard 2225